University of Sussex

Toward coherent ion-cavity coupling

Markus O. Vogt

Submitted for the degree of Doctor of Philosophy
University of Sussex
September 2016

Declaration

I hereby declare that this thesis has not been and will not be, submitted in whole or in part to another University for the award of any other degree.

Signature:

Markus Otto Vogt

20th April 2017

UNIVERSITY OF SUSSEX

Markus Otto Vogt, Doctor of Philosophy

Toward coherent ion-cavity coupling

Summary

Entanglement is an established resource in quantum information processing, and there is a clear imperative to study many-body systems both in quantum technology applications and for probing fundamental physical laws. Ion trap cavity quantum electrodynamics is a highly promising platform for research. Prerequisites are the controlled coupling of many ions to the cavity field along with the ability to initialize the quantum states and drive coherent transitions between them.

A coaxial ion trap and high finesse cavity system has been shown to couple strings of up to five ions to the cavity mode with nearly optimal coupling strength thanks to precise control over their positions in the standing wave and their mutual Coulomb interaction. The predictive power of the theoretical model demonstrates that the scheme can be extended to more ions or to higher coupling regimes.

In a separate experiment it has been demonstrated that a quantum state can be initialized, before coherently transferring the population to a qubit state through the cavity interaction. The emission of polarized photons in the cavity mode has been measured, taking the system closer to the generation of cluster states for quantum information research and fundamental studies in many-body entanglement.

Building on the aforementioned work, an infrastructure has been put in place for the direct observation of vacuum Rabi oscillations between a single ion and the cavity. In this scheme, the contribution to the dynamics from the dominant incoherent channel is minimized through post-selection of the data. As a quantum system coupled to a reservoir with memory, it will provide experimental constraints on theoretical work in the field of non-Markovian dynamics.

Acknowledgements

The work described in this thesis was carried out in the Ion trap cavity QED and molecular physics (ITCM) group laboratories at the University of Sussex between 2012 and 2016. I did not know what to expect when I began a PhD in experimental atomic physics - even the difficulty of coming to grips with the tools of ion trap CQED is overshadowed by the unnatural clarity and focus required to do actual Science. It has been such a steep learning curve that it was really only while writing this thesis that I realized that I somehow did manage to make a contribution, however modest. I am deeply grateful to have had the opportunity.

So a huge thank you to Matthias Keller, whose knowledge, vision, drive and patience are awing and inspiring. It is humbling to have glimpsed some of the scope of the work done by academics of research, overseeing the great project of scientific endeavour, and often invisible to the world at large.

I wish to acknowledge Professor Wolfgang Lange, rest in peace, for a great legacy of humour and humanity which he left to the AMO community and to anyone who has had the privilege of his company. To quote a colleague who knew him much better than I did, he became your friend by simply walking into the room.

Nic Seymour Smith and Kevin Sheridan were outgoing post-doctoral researchers when I was a newcomer at ITCM and gave me much needed early advice and encouragement. I am very grateful to Gurpreet Kaur Gulati for bringing her professionalism and dedication at just the moment when our project really needed it. It has been a pleasure to meet you and those qualities will now serve you very well at NASA.

Over all these years in the lab, however, Hiroki Takahashi has been the one upon whose shoulders the burden of my quantum optics training has in large part rested. Thank you for showing me that there is a right way to do it, and thanks for your patience as I have puzzled over the bewildering secrets of the Quantum. As well as knowing nearly everything, Hiroki always reminds you that physics can, indeed, be fun.

Alan Butler makes an enormous contribution to the work done at ITCM. Alan gets us out of countless pickles with not just immense engineering skill, but gratefully received

kindness and compassion. I hope that you have the wonderful retirement you deserve, just never forget the difference you have made to so many early researchers.

The pressures of working in this field have been mitigated by the great people that make up ITCM. I owe a debt of gratitude to Stephen Begley as my lab partner for three years. My deepest thanks to Ezra Kassa and Jack Morphew, Class of 2016, for crucial support and many fond memories - all the very best for the future guys! Thanks to Arijit Sharma, Callan Jobson, William Groom and Sahar Hejazi for help, suggestions and discussions in the lab. Welcome also to the new vanguard, Vicentiu Iancu, Costas Christoforou and especially Tom Walker - it has been a pleasure to work with you and I have every confidence that you will get important results with the apparatus.

Thank you to Christina and Michael, my parents, who are exceptional in the love and support which they have always given me. I really hope that I have made them both sufficiently aware of the huge role they have played in my happiness.

Finally, there are many reasons why without Amy Gardner I could not have written this thesis. Before and after she opened the door for me at ITCM, Amy has been my soul mate and best friend. In the lab you have made me a better scientist and beyond physics you have made me a better person. Thank you so much!

Contents

Chapter 1

Introduction

Quantum information processing (QIP) is expected to greatly enhance humankind's ability to perform certain important algorithms [1] and carry out simulations of systems which cannot be computed classically [2]. In the last ten years, cavity quantum electrodynamics (CQED) has presented a wide range of techniques whereby quantum emitters are localized in high-finesse optical cavities [3; 4; 5; 6; 7]. In order for an experimental system to carry out useful QIP, it is necessary that it be scalable [8]. CQED is a highly promising platform for scalability due to the inherent coupling of photons to quantum emitters. While the systems are relatively easily coupled, they are nonetheless ideally suited to applications in quantum information technology [9] and the study of fundamental processes in physics such as entanglement and decoherence [10]. The natural scalability in these systems arises from the inherent coupling of the internal states of the emitters to degrees of freedom associated with the cavity field, leading to the possibility of linking emitter nodes with optical fibers in a network. Proof-of-principle demonstrations of quantum networking have recently been demonstrated [11; 12; 13]. Mode-matching the cavity output to fiber optics is straightforward, and this mature technology can link stationary nodes of a quantum network through the transfer of quantum information encoded in photonic degrees of freedom [12]. Ion traps are excellent candidates to occupy these nodes as fault-tolerant quantum computation has been demonstrated [14].

Qubit entanglement is the resource at the heart of QIP, and large scale entanglement of many ions is the ultimate aim of our system. The Innsbruck group has achieved entanglement of up to 14 ions [15] using the Coulomb interaction between ions in a string trapped in a common potential. However, experimental complexity increases as the vibrational modes present increase with the number of ions in the string, limiting the scalability of this approach. By contrast, we have a scheme for many-ion entanglement which utilizes

the common coupling of a string of ions to a cavity field.

There are significant challenges which arise when dielectric mirror coatings are brought into proximity with the trapping field, hitherto preventing attainment of the strong coupling regime in ion trap CQED. Strong coupling is achieved if the rate of emitter-cavity coupling is greater than the dissipative processes, and small volume cavities are a requirement for high rates of coupling. Nevertheless, ion trap CQED has achieved significant milestones such as the generation of single photons [4], the entanglement of an ion with a photon [16] and the heralded entanglement of two ions [17].

While the challenge of strong coupling has not yet been met, there are probabilistic schemes for entanglement of many trapped ion qubits which do not require it [18]. Furthermore, ion trap CQED has the advantage that quantum emitters can be deterministically and precisely localized in the cavity standing wave [19] for periods of time extending to many hours [20].

Our QIP system comprises a linear ion trap with an integrated high-finesse optical cavity. The cavity field and trap axes are co-linear, allowing the simultaneous deterministic positioning of many calcium ions, each close to an antinode of the cavity field, i.e. with close to optimal coupling strength. This is achieved through precise control of both the inter-ion distances, as well as the axial coordinate of the cavity field. An example of a probabilistic entanglement scheme available to us of the type proposed by Duan and Kimble [18] (and already implemented by the Innsbruck group [17]), is as follows. Our qubit is encoded in the Zeeman sub-levels of the long-lived $D_{3/2}$ manifold in $^{40}Ca^{+}$. After preparation of the ion in the ground $S_{1/2}$ state, a control laser mediates a cavity-assisted Raman transition which coherently couples the ground state to one of two $D_{3/2}$ qubit states with equal probability, with the emission of a photon in the cavity mode whose polarization is entangled with the final qubit state of the ion. Simultaneously addressing two similarly prepared ions results in the emission of two photons. The scheme takes advantage of the erasure in the cavity of which-way information associating a photon with a particular ion. Therefore, simultaneous detection of two orthogonally polarized photons heralds the entanglement of the two ion qubits. With individual ion addressing, several entangled pairs will be created in a string, and these pairs then fused into a highly entangled array of qubits, known as a cluster state, through parity checks on different pair partners.

QIP is often associated with a *circuit* model of quantum computation, in which qubit initialization is followed by successive entangling gate operations. However it is challen-

ging to implement a logical gate on an arbitrary state, while it is relatively easy to create a specific state. In the *cluster state*, or *measurement-based*, model of quantum computation, many qubits are prepared in a single entangled state, which forms a substrate for computation. The computation is achieved by successive measurements of the state of each qubit with measurement results classically fed forward to determine the bases for further measurements [21]. The ultimate aim of our ion trap CQED setup is the generation of large matter-qubit cluster states for the implementation of measurement-based quantum computation. Although measurement-based quantum algorithms have been demonstrated by other groups, experimental realizations of cluster states have so far been realized only with qubits encoded in photonic degrees of freedom and the number of qubits has remained limited to six [22]. Our system is a unique platform with which to explore cluster state quantum computation [23] with larger numbers of matter qubits, as well as to study many-qubit entanglement at a fundamental level [24].

In order to implement this, the ion trap-cavity system and vacuum chamber were designed by Matthias Keller and built by Nicolas Seymour-Smith, Peter Blythe and Dan Crick. Nicolas Seymour-Smith and Dan Crick built the optics, detection and laser systems, as well as a stable atomic frequency reference and a scanning cavity stability transfer system. The frequency reference was further improved by Ezra Kassa during the time that the work described in this thesis was being carried out. These systems are described in detail in chapter 3 of this thesis. After locating the trapped ions in the cavity mode, a proof-of-principle demonstration of ion-cavity coupling had been performed by Nicolas Seymour-Smith, in which he drove cavity-assisted Raman transitions in a large ion crystal whilst manually holding the cavity length on resonance. Blocking the light from the control laser interrupted the cavity emission, confirming the ion-cavity coupling [25]. After this, Stephen Begley and I inherited the system. It was soon decided that after Nic's proof-of-principle demonstration, the system could be further improved in terms of both the rf confinement of the trap, and the cavity finesse. The vacuum system was opened, the rf circuit rewired and mirrors replaced, paving the way for the two experiments described in this thesis which bring the setup closer to the realization of many-ion cluster states.

The first experiment explores the extent to which we can simultaneously position many ions close to the anti-nodes of the cavity field where optimal coupling is achieved. The efficiency of the probabilistic entanglement scheme relies critically upon the degree of coupling of all the ions to be entangled. In general, previous work in atomic CQED has largely focused on coupling either single atoms or large ensembles. In the case of the

latter, individual couplings are not controlled and it is the averaged contribution that is of interest [26; 27]. In 1954 Dicke first explored the realm of multi-atom coupling to a single cavity with the model of superradiance [28], but experimental work has begun only recently [17; 29; 30]. In general, the physics manifest in the interactions of many atoms through a common cavity mode is far richer than for single emitters [31; 32], and applications include quantum logic gates [33; 34], nonclassical light sources [35; 36] and schemes for entanglement generation [37; 38]. As stated above, the Innsbruck group have entangled two ions in a cavity-mediated interaction, with a remarkable fidelity of 92%, however their setup is currently limited to two-ion entanglement as the trap and cavity axes are nearly orthogonal [17]. In the multi-ion cavity coupling experiment described in chapter 4 of this thesis, we control the individual coupling strengths of up to five ions, thanks to the co-axial ion trap-cavity construction. Their average coupling strength was shown to be greater than 98% of the maximum attainable in the ideal case of the ions' positions coinciding exactly with anti-nodes of the cavity field. The good agreement of the results with a model developed by Hiroki Takahashi paves the way for confident predictions of the behaviour of the system when many-ion entanglement is attempted. With further contributions from Gurpreet Kaur Gulati, the result led to the following publication with an Editors' Suggestion:

> S. Begley, M. Vogt, G. K. Gulati, H. Takahashi and M. Keller, "Optimized Multi-Ion Cavity Coupling," *Physical Review Letters*, vol. 116, no. 22, p. 223001, 2016.

In a separate experiment, focus was turned to realizing the coherent cavity-assisted Raman transition from a prepared state to a target state, as a precursor for the transition which will eventually lead to two-ion entanglement. A single ion is initialized in a specific Zeeman sub-state, and the coherent cavity-assisted Raman transition to the qubit state, required by our entangling scheme, is performed and characterized. This is described in chapter 5 and the work was done by myself with contributions from Hiroki Takahashi. Here the ion state is initialized through optical pumping and the coherent transition to the target state confirmed by a measurement of the polarization purity of the cavity emission. In future work, the scene is therefore set for ion-ion entanglement generation in which a bichromatic control beam will similarly address two ions in the cavity.

Additionally, a final piece of work was done which followed naturally from that just described. Previously, while work was being carried out on multi-ion cavity coupling, the system had been theoretically evaluated by Kimmo Luoma (Theoretical Quantum Optics group at Dresden University) for the observation of vacuum Rabi oscillations,

and it was decided to implement the proposal as an extension of the work done on the coherent ion-cavity interaction described above. Whilst driving the cavity-assisted Raman transition, the coherent evolution of the system results in an oscillation in probability of a photon occupying the cavity mode predicted by the Jayne-Cummings model. This coherent evolution within the $D_{3/2}$ manifold is vulnerable to the dominant decay process in the system, namely the high rate of scatter to the ground state from the excited $P_{1/2}$ level. The setup was modified to include time-resolved detection of the cavity emission and which-way control of the laser pulses to include a state detection sequence in order to post-select the data and eliminate the effect of the fast incoherent process. Although an oscillation has not been detected above the noise of the system, key sources of dephasing, decoherence and signal to noise degradation have been identified.

Chapter 2

Theory

The aim of this chapter is to introduce some of the theoretical framework which underpins the experiments in this thesis. It applies broadly to the techniques and measurements which are implemented in ion trap cavity QED, and is supplemented in subsequent chapters by deeper theoretical considerations when they become relevant.

The physics behind the confinement generated in linear rf quadrupole ion traps is presented first, leading to the equations of motion for the trapped ion.

Then follows a discussion of the basic interaction between light and matter and the mechanics by which laser light couples the quantized atomic energy levels. The optical Bloch equations are derived for a two level atom, and then solved to get expressions for the steady state atomic populations in terms of the laser intensity, detuning and decay rate of the excited state. This sets the scene for a description of laser Doppler cooling. This is a fundamental and indispensable technique in ion-trapping, so the process is outlined and an expression derived for the fundamental temperature limit attainable with this type of laser cooling. Both of the experiments described in chapters 4 and 5 rely on attainment of temperatures close to this limit.

The main results from cavity QED are presented which govern the way in which an ion, when driven by the free-space mode of a laser, emits directional radiation into the cavity mode. This cavity-assisted Raman transition is a coherent process which couples two long-lived states in the ion, and produces a photon at the cavity output with a high probability of detection. It is this mechanism which produces cavity emission which is detected as a means of determining the degree of ion-cavity coupling making possible the experiments in chapter 4. It is also the transition which couples the initialized state with the final qubit state in the experiments in chapter 5. Here, a magnetic field defines the quantization axis in such a way that the polarization of the emitted photon is correlated

with the final internal state of the ion. This is a precursor to ion-ion entanglement, and some entanglement schemes available to our setup are outlined. This theory chapter ends with the description of an extension to the entanglement scheme which will fuse entangled pairs into cluster states.

2.1 RF ion trap theory

The electric field is divergenceless in vacuum:

$$\vec{\nabla} \cdot \vec{E} = 0. \tag{2.1}$$

This fact leads directly to a theorem by Earnshaw which states that there is no local minimum in the electric potential in free space, so that the use of a static electric field to confine a charged particle, such as an ion, is forbidden. Most ion traps used in physics research fall broadly into two categories [39]: Penning traps, in which ions (or electrons) are confined through the overlaying of static electric and magnetic fields; and rf Paul traps, which generate a time averaged psuedopotential minimum through an electric field which switches direction at radio frequency. The motion of an ion in a Penning trap is epicyclic and that of an ion in an rf trap is harmonic with an element of driven motion at the rf frequency. The rf trap confines the ion with unique motional control and precise localization.

RF traps in turn fall into different geometric categories including linear traps, ring traps, endcap traps and surface traps, each of which offer advantages and disadvantages which may be weighted in the context of the experimental purpose for which the trap is required. The linear ion trap featured in this thesis has been designed to trap strings of ions co-axially with the mode of a high finesse optical cavity, with the purpose of tuning the equilibrium positions of the ions to coincide with antinodes of the cavity field, optimizing their CQED coupling. To this end, a 2 dimensional quadrupole trap geometry is chosen as it offers an extended linear trapping region with near-constant confinement across strings of many ions. A schematic of our trap is presented in Fig. 2.1 showing the blade-shaped rf electrodes, the dc endcap electrodes, and coordinate system. Following Ghosh [39] in determining the equations of motion for a trapped ion, the derivation below assumes a single ion in the trap, and rf electrodes with ideal hyperbolic geometry. To model the true potentials of a real trap, finite element modeling software may be used.

An rf voltage

$$U(t) = \frac{1}{2} \pm U_{\mathrm{rf}} \cos(\Omega_{\mathrm{rf}} t) \tag{2.2}$$

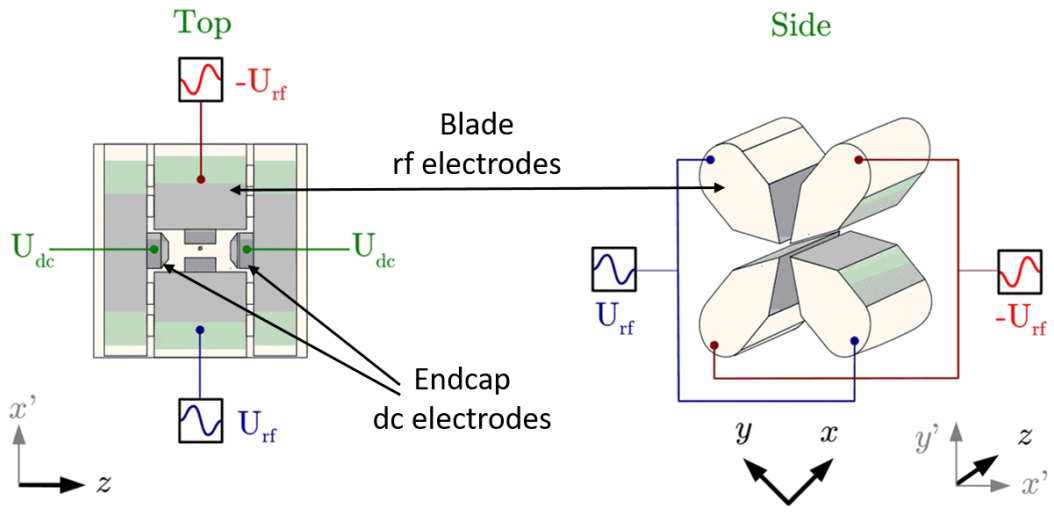

Figure 2.1: Schematic of blade-electrode trap. Voltage of similar polarity $\pm U_{\mathrm{rf}}$ is applied to opposing blades to provide radial confinement. U_{dc} is applied to the endcaps. x, y and z refer to the principle axes of the trap, with x' and y' along the natural vertical and horizontal directions. Without qualification, the *trap axis* refers to the line equidistant to all four blade edges, and pointing in the z direction. Figure taken from [25].

is applied to the rf blade electrodes with opposite blades sharing the same polarity. Here, U_{rf} is the voltage amplitude and Ω_{rf} is the frequency. This generates an oscillating quadrupole field in the radial direction. A dc voltage U_{dc} is applied to each endcap electrode, providing confinement along the trap axis.

We examine the confinement in the radial direction. A positively charged ion near the trap centre will feel a force due to the potential

$$\phi(x,y,t) = -\frac{1}{2}U_{\mathrm{rf}}\cos(\Omega_{\mathrm{rf}}t)\left[\frac{x^2-y^2}{r_0^2}\right] - \frac{1}{2}\eta U_{\mathrm{dc}}\left[\frac{x^2+y^2}{z_0^2}\right]. \tag{2.3}$$

Here, $2z_0$ is the endcap to endcap separation, r_0 is the ion to rf electrode separation, and η is a geometric factor [40]. The second term on the right-hand side carries a negative sign, reflecting the anti-confining contribution in the radial direction due to the positively charged endcap electrodes [41].

The fast-switching direction in which the trap is confining and anti-confining realizes a ponderomotive potential with the mechanical analogy of a massive particle resting at the centre of a fast-rotating saddle.

A particle of mass m and charge Q obeys Newton's second law in the x direction, with

$$\ddot{x} + \frac{Q}{m}\frac{\partial\phi(x,y,t)}{\partial x} = 0 \tag{2.4}$$

and letting $\tau = \frac{\Omega_{\rm rf} t}{2}$ we have

$$\frac{d^2x}{d\tau^2} = \frac{4Q}{m\Omega_{rf}^2}\frac{\partial\phi(x,y,t)}{\partial x} = 0. \tag{2.5}$$

It is useful when parametrizing the trap confinement to make the substitutions:

$$q = \frac{2QU_{rf}}{m\Omega_{\rm rf}^2 r_0^2} \tag{2.6}$$

and

$$a = -\frac{4Q\eta U_{dc}}{m\Omega_{\rm rf}^2 z_0^2}. \tag{2.7}$$

This casts the problem of the motion in the form of a pair of Matthieu equations in x and y:

$$\frac{d^2x}{d\tau^2} - (a - 2q\cos(2\tau))\,x = 0 \tag{2.8}$$

and after the same steps

$$\frac{d^2y}{d\tau^2} - (a + 2q\cos(2\tau))\,y = 0. \tag{2.9}$$

To arrive at an expression for the ion's motion in the trap, we make the physically justifiable approximations that the ion's excursion from the trap centre is small, and that the a and q parameters are small (see section 3.4.5 for the measured values). We now have

$$u_i(t) = U_i\,(1 - q\cos(\Omega_{rf}t))\cos(\omega_r t) \tag{2.10}$$

in which u_i are the two radial coordinates, U_i are the amplitudes of the displacements of the ion from the equilibrium position and ω_r is known as the radial secular frequency. It is slow compared to the driven micromotion at the trap drive frequency $\Omega_{\rm rf}$ with

$$\omega_r = \frac{\sqrt{q^2/2 \pm a}}{2}\Omega_{rf}. \tag{2.11}$$

The radial motion of the ion in the trap is shown in Fig. 2.2. The micromotion superposed on the secular motion grows in amplitude with distance from the trap centre. In practice, this motion is unwanted, and the care taken to minimize it is described in section 3.4.3. The secular motion is damped through Doppler cooling, described in section 2.2.2.

The endcap electrodes are held at dc voltages $U_{\rm dc}$ so that the potential in the axial direction is

$$\phi(z) = \eta U_{\rm dc}\frac{z^2}{z_0^2}, \tag{2.12}$$

and the motion is harmonic.

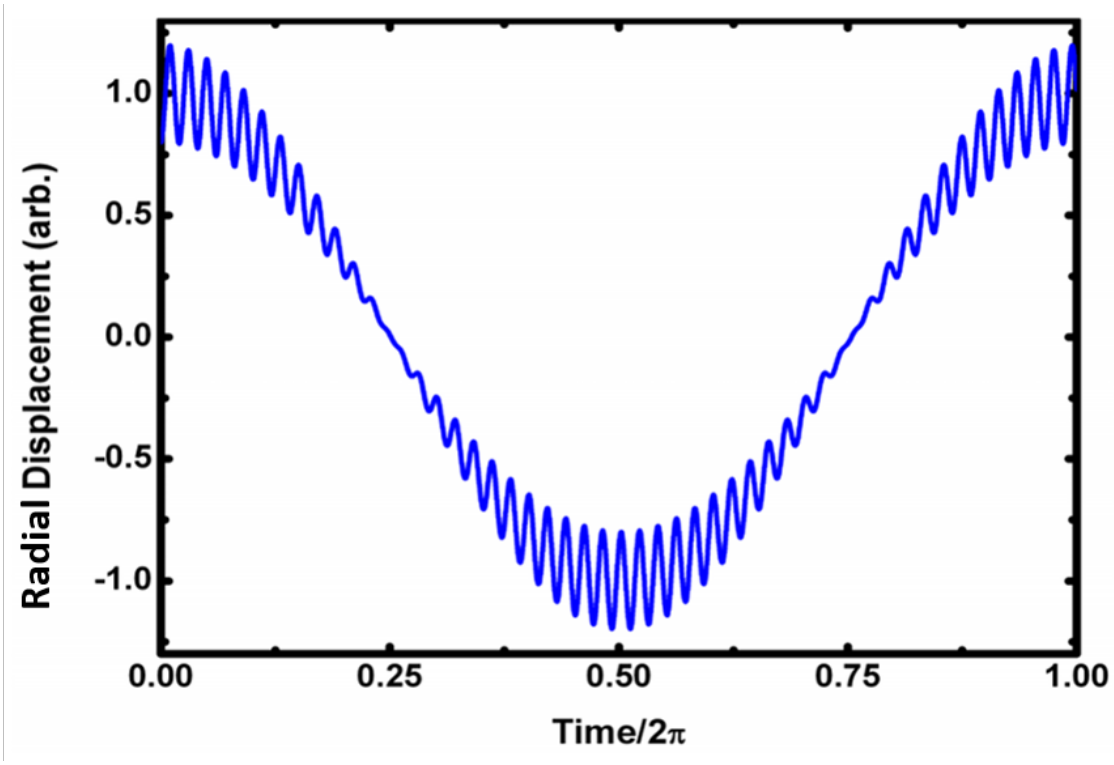

Figure 2.2: Modelling the ion's motion. The amplitude of the secular motion is 1, q has a value of 0.2, and $\Omega_{rf} = 50\omega_r$. Figure taken from [42].

2.2 Atom-light interactions

Narrow-linewidth lasers enable the coupling of discrete energy states within the atomic structure. Energy levels in quantum-mechanical atoms are stationary states, and we require a time-varying perturbation for one state to evolve to another. A two-level system is sketched in Fig. 2.3. If the atom is in the ground state $|1\rangle$, and exposed to laser light of a frequency close to resonance with a transition in the atom to another (excited) state $|2\rangle$, then the atom may undergo the transition from $|1\rangle$ to $|2\rangle$. The light field in the vicinity of the atom oscillates at a frequency which serves to couple the two states for the correct amount of time to leave the atom in $|2\rangle$. This process is known as stimulated absorption of a photon by the atom. The time-reversed process, in which an atom is in state $|2\rangle$ and a light field couples it to $|1\rangle$ leaving it in the ground state, is known as stimulated emission. If left in the excited state with no resonant light switched on to couple it to other states, the atom will nevertheless decay spontaneously to a lower energy state after a characteristic time known as the lifetime of the excited state. This is because the zero-point vacuum energy contains all the frequencies to couple the transitions. This is known as spontaneous decay, in which a photon is emitted into the vacuum. Spontaneous absorption does not

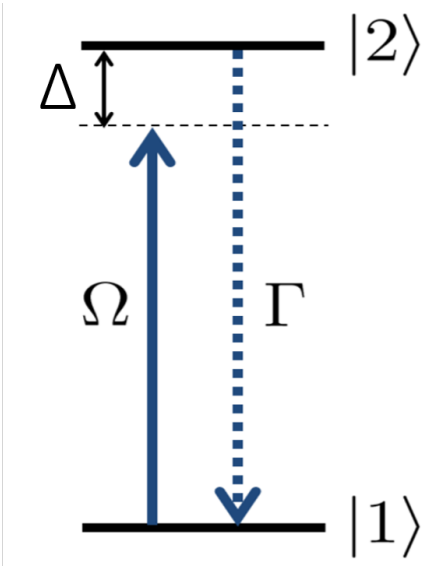

Figure 2.3: Two level atom. The stationary states are coupled by a laser of intensity corresponding to a Rabi frequency of Ω, detuned from resonance by Δ. Γ is the spontaneous decay rate from $|2\rangle$ to $|1\rangle$. Figure taken from [42].

occur due to energy conservation as the vacuum energy density is too low. In this section we will review the perturbation mechanics which describe the stimulated processes. The derivation required for the rigorous inclusion of the the decay process is beyond the scope of this thesis and is introduced phenomenologically.

We will see that an atom in the presence of a driving laser field may undergo coherent oscillations between two coupled states, as long as the spontaneous decay rate from the upper level is less than the rate of the oscillations. These are known as Rabi oscillations. In $^{40}Ca^{+}$, however, the excited state decays quickly, so that when driven with a resonant laser, a steady state is reached with populations in both levels. We will derive a set of equations, called the optical Bloch equations, whose solutions give the populations of the energy levels as a function of the laser intensity, detuning and atomic decay rate.

After introducing the dynamics of a two-level atom with a single laser it will be shown that the lineshape of the absorption spectrum of the atom is in general a power-broadened Lorentzian. The next section demonstrates how this enables the technique of laser Doppler cooling, and how the cooling parameters may be optimized for cooling to the lowest temperature possible for the chosen cooling transition. Attainment of temperatures close to this Doppler limit is crucial for the experiments detailed in chapters 4 and 5. It will then be shown that practical Doppler cooling of $^{40}Ca^{+}$ requires the coupling of more than two energy levels, and after exploring a cooling scheme in which three levels are coupled by two lasers it will be clear that improved cooling is possible by coupling five levels by

three lasers. The dymanics of this cooling scheme are well approximated by those of a two-level system and is the one employed in the experiments in this thesis. It is described at the end of the section.

2.2.1 Two-level system coupled by a laser

In deriving the optical Bloch equations we will closely follow [43]. The derivation is semi-classical, in that the energy levels of the atom are quantized, while it is sufficient to consider a classical light field. We consider an atom with two states $|1\rangle$ and $|2\rangle$, whose energies are $E_1 = \hbar\omega_1$ and $E_2 = \hbar\omega_2$ with an energy difference $\Delta E = \hbar(\omega_2 - \omega_1) = \hbar\omega_0$. A near-resonant laser of frequency ω detuned $\Delta\omega = \omega_0 - \omega$ couples the two levels due to its interaction with an atomic dipole moment which arises when the levels are coupled by the time-varying field.

Coupled equations of a two-level system

The wave function for the two level system is written

$$|\Psi\rangle = |1\rangle + |2\rangle \tag{2.13}$$

$$\Psi = \psi_1(\mathbf{r})\,\mathrm{e}^{-i\omega_1 t}C_1(t) + \psi_2(\mathbf{r})\,\mathrm{e}^{-i\omega_2 t}C_2(t), \tag{2.14}$$

where the time-dependent and space-dependent parts of each level are shown explicitly as well as the amplitudes $C_{1,2}$. The time-dependence of the amplitudes anticipates the coupling of the two levels by a time-dependent perturbation. The time-dependent Schrödinger equation is

$$\hat{H}\Psi(\mathbf{r},t) = i\hbar\frac{\partial\Psi}{\partial t}. \tag{2.15}$$

In the presence of a classical laser field, the Hamiltonian may be written as the sum of two terms

$$\hat{H} = \hat{H}_A + \hat{V}(t), \tag{2.16}$$

where $\hat{H}_A$ is the bare atomic Hamiltonian

$$\hat{H}_A = \hbar\omega_1 |1\rangle\langle 1| + \hbar\omega_2 |2\rangle\langle 2| \tag{2.17}$$

and $\hat{V}(t)$ represents the time-varying energy due to the atom-light interaction, responsible for coupling the states $|1\rangle$ and $|2\rangle$.

Upon substitution of the time-dependent wave function in Eq. (2.14) in the Schrödinger equation, multiplying from the left by $\psi_1^*(\mathbf{r})e^{i\omega_1 t}$ and integrating gives:

$$C_1\int\psi_1^*\hat{V}\psi_1 d\mathbf{r} + C_2\mathrm{e}^{-i\omega_0 t}\int\psi_1^*\hat{V}\psi_2 d\mathbf{r} = i\hbar\frac{dC_1}{dt}, \tag{2.18}$$

along with a second expression similarly obtained by left-multiplication with $\psi_2^*(\mathbf{r})e^{i\omega_2 t}$. The quantities $\int \psi_1^* \hat{V} \psi_1 d\mathbf{r}$ and $\int \psi_1^* \hat{V} \psi_2 d\mathbf{r}$ are known as matrix elements, and will be denoted V_{11} and V_{12} respectively. We have

$$C_1 V_{11} + C_2 \mathrm{e}^{-i\omega_0 t} V_{12} = i\hbar \frac{dC_1}{dt} \tag{2.19}$$

$$C_1 \mathrm{e}^{i\omega_0 t} V_{21} + C_2 V_{22} = i\hbar \frac{dC_2}{dt}. \tag{2.20}$$

We have two coupled equations for the quantities C_1 and C_2, the probability amplitudes as a function of time for the ground and excited states of the atom when the atom is subjected to a time-varying perturbation $\hat{V}(t)$.

Coupling operator

The atom is driven with a coherent laser field $\mathbf{E}(z,t)$, polarized along the unit vector $\hat{\mathbf{e}}$ and propagating along the z-direction with amplitude E_0, at a frequency ω close to the atomic transition frequency ω_0:

$$\mathbf{E}(z,t) = \hat{\mathbf{e}} E_0 \cos(\omega t - kz). \tag{2.21}$$

Optical wavelengths are on the order of 10^4 larger than the radius of an atom as characterized by the Bohr radius, so we may make the *dipole approximation* in which the spatial variation of the field across the atom is neglected, $\mathbf{E}(z,t) \rightarrow \mathbf{E}(t) = \hat{\mathbf{e}} E_0 \cos(\omega t)$. The atom is modeled as a dipole

$$\mathbf{d} = -e\mathbf{r} = -e \sum_j^N \mathbf{r}_j, \tag{2.22}$$

where e is the electronic charge and the sum is over the coordinate $\mathbf{r}$ of each of N electrons. After rewriting Eq. (2.22) as an operator equation

$$\hat{\mathbf{d}} = -e\hat{\mathbf{r}} = -e \sum_j^N \hat{\mathbf{r}}_j, \tag{2.23}$$

the interaction part of the Hamiltonian $\hat{V}(t)$ may now be written as the scalar product of the atomic dipole with the electric field:

$$\hat{V} = -\hat{\mathbf{d}} \cdot \mathbf{E}. \tag{2.24}$$

$\hat{V}$ has odd parity with respect to $\mathbf{r}$ so that the matrix elements V_{11} and V_{22} are equal to zero. The dipole matrix element μ_{12} is defined

$$\mu_{12} = e \int \psi_1^* \left(\sum_j^N \hat{\mathbf{r}}_j \cdot \hat{\mathbf{e}} \right) \psi_2 \, d\mathbf{r}, \tag{2.25}$$

so that the non-zero matrix elements of Eqs. (2.19) and (2.20) are

$$V_{12} = \mu_{12} E_0 \cos(\omega t) \tag{2.26}$$

$$V_{21} = \mu_{21} E_0 \cos(\omega t). \tag{2.27}$$

Defining the *on-resonance* Rabi frequency Ω_0, which describes the strength of the coupling between the atomic dipole and the electric field:

$$\Omega_0 = \frac{\mu_{12} E_0}{\hbar} \tag{2.28}$$

we may write

$$V_{12} = \hbar \Omega_0 \cos(\omega t). \tag{2.29}$$

We may now write the coupled Eqs. (2.19) and (2.20) as

$$\Omega_0 \cos(\omega t) \mathrm{e}^{-i\omega_0 t} C_2 = i \frac{dC_1}{dt} \tag{2.30}$$

$$\Omega_0^* \cos(\omega t) \mathrm{e}^{i\omega_0 t} C_1 = i \frac{dC_2}{dt}. \tag{2.31}$$

Rewriting the expression $\cos(\omega t)$ in exponential form, Eq. (2.30) becomes

$$\frac{\Omega_0}{2} \left[\mathrm{e}^{-i(\omega_0+\omega)t} + \mathrm{e}^{-i(\omega_0-\omega)t} \right] C_2 = i \frac{dC_1}{dt}. \tag{2.32}$$

We have assumed that the frequency of the light field ω is close to resonance with the atomic transition ω_0, which is on the order of 10^{15} Hz for the optical spectrum. Therefore the first term on the left-hand side of Eq. (2.32), which contains the expression $\mathrm{e}^{-i(\omega_0+\omega)t}$, oscillates very fast compared to the rate at which the coefficients C_1 and C_2 evolve. Over the timescale of the transition, its effect is negligible compared to the term containing the expression $\mathrm{e}^{-i(\omega_0-\omega)t}$. The fast-oscillating term is dropped in what is known as the rotating wave approximation (RWA). After applying the approximation to Eqs. (2.30) and (2.31) we have

$$\frac{\Omega_0}{2} \mathrm{e}^{i\Delta\omega t} C_2 = i \frac{dC_1}{dt} \tag{2.33}$$

$$\frac{\Omega_0^*}{2} \mathrm{e}^{-i\Delta\omega t} C_1 = i \frac{dC_2}{dt}. \tag{2.34}$$

These equations may be solved with the intial conditions at $t = 0$, $C_1(0) = 1$ and $C_2(0) = 0$ giving an expression for the time-dependence of the excited state population $|C_2(t)|^2 = 1 - |C_1(t)|^2$:

$$|C_2(t)|^2 = \frac{|\Omega_0|^2}{\Omega^2} \sin^2 \left(\frac{\Omega}{2} t \right). \tag{2.35}$$

Here,

$$\Omega = \sqrt{(\Delta\omega)^2 + \Omega_0^2} \tag{2.36}$$

is the generalized Rabi frequency, which includes the detuning of the laser. This oscillatory behaviour of the state population is known as Rabi oscillation and is a coherent transfer of population between the ground state and some maximum probability of being in the excited state. This maximum excited state probability reaches unity for zero detuning and allows the deterministic excitation of a ground state ion to the excited state. It is achieved with a resonant pulse of light of a duration equal to half a period of the Rabi oscillation, and is known as a π pulse.

We have solved Schrödinger's equation for a two-level system and a time-varying Hamiltonian which has served to couple the two states and make transitions between them possible. A theoretical framework for the stimulated transition between the two levels, while emitting or absorbing a photon from the light field mode, has been developed. However, the effects of spontaneous emission have not been included in this account. Spontaneous emission is an incoherent process which populates a distribution of light modes and leaves the atom in a distribution of momentum states. This departure from a situation in which a single wave function describes the dynamics requires the introduction of the formalism of the density operator. The optical Bloch equations are expressions for the time evolution of the density operator matrix elements. Phenomenologically including a decay term will give a steady-state solution for these equations which predicts the fluorescence of an ion as a function of the detuning of the laser, underpinning the description of laser Doppler cooling.

The Optical Bloch equations

The density operator $\hat{\rho}$ is defined

$$\hat{\rho} = \sum_i P_i \left|\psi_i\right\rangle \left\langle\psi_i\right|, \tag{2.37}$$

where P_i is the probability of finding the system in the state $|\psi_i\rangle$. For a two-level system it is a 2 x 2 matrix

$$\hat{\rho} = \begin{pmatrix} \rho_{11} & \rho_{12} \\ \rho_{21} & \rho_{22} \end{pmatrix} = \begin{pmatrix} |C_1|^2 & C_1 C_2^* \\ C_2 C_1^* & |C_2|^2 \end{pmatrix}. \tag{2.38}$$

The diagonal elements ρ_{11} and ρ_{22} are the populations of $|\psi_1\rangle$ and $|\psi_2\rangle$ respectively, with $\rho_{11} + \rho_{22} = 1$, and the off-diagonal elements are known as coherences, with $\rho_{21} + \rho_{12}^*$.

Element-wise differentiation of Eq. (2.38) gives

$$\frac{\mathrm{d}\rho_{11}}{\mathrm{d}t} = C_1\frac{\mathrm{d}C_1^*}{\mathrm{d}t} + \frac{\mathrm{d}C_1}{\mathrm{d}t}C_1^* \tag{2.39}$$

$$\frac{\mathrm{d}\rho_{22}}{\mathrm{d}t} = C_2\frac{\mathrm{d}C_2^*}{\mathrm{d}t} + \frac{\mathrm{d}C_2}{\mathrm{d}t}C_2^* \tag{2.40}$$

$$\frac{\mathrm{d}\rho_{12}}{\mathrm{d}t} = C_1\frac{\mathrm{d}C_2^*}{\mathrm{d}t} + \frac{\mathrm{d}C_1}{\mathrm{d}t}C_2^* \tag{2.41}$$

$$\frac{\mathrm{d}\rho_{21}}{\mathrm{d}t} = C_2\frac{\mathrm{d}C_1^*}{\mathrm{d}t} + \frac{\mathrm{d}C_2}{\mathrm{d}t}C_1^*. \tag{2.42}$$

Eqs. (2.33) and (2.34) are substituted for $\frac{\mathrm{d}C_1}{\mathrm{d}t}$ and $\frac{\mathrm{d}C_2}{\mathrm{d}t}$ to give

$$\frac{\mathrm{d}\rho_{22}}{\mathrm{d}t} = i\frac{\Omega_0}{2}\mathrm{e}^{i\Delta\omega t}\rho_{21} - i\frac{\Omega_0^*}{2}\mathrm{e}^{-i\Delta\omega t}\rho_{12} = -\frac{\mathrm{d}\rho_{11}}{\mathrm{d}t} \tag{2.43}$$

$$\frac{\mathrm{d}\rho_{12}}{\mathrm{d}t} = i\frac{\Omega_0}{2}\mathrm{e}^{i\Delta\omega t}(\rho_{11} - \rho_{22}) = \frac{\mathrm{d}\rho_{21}^*}{\mathrm{d}t} \tag{2.44}$$

Equations (2.44) are the optical Bloch equations in the absence of spontaneous emission, and may be solved with the initial conditions $\rho_{11} = 1$, $\rho_{22} = 0$ and $\rho_{21} = 0$ to recover Eq. (2.35) describing Rabi oscillations.

Any excited state eventually decays via spontaneous emission at a rate Γ. To include this effect in the dynamics, a decay term $-i(\Gamma/2)C_2$ is included in Eq. (2.34). The optical Bloch equations then become

$$\frac{\mathrm{d}\rho_{22}}{\mathrm{d}t} = i\frac{\Omega_0}{2}\mathrm{e}^{i\Delta\omega t}\rho_{21} - i\frac{\Omega_0^*}{2}\mathrm{e}^{-i\Delta\omega t}\rho_{12} - \Gamma\rho_{22} = -\frac{\mathrm{d}\rho_{11}}{\mathrm{d}t} \tag{2.45}$$

$$\frac{\mathrm{d}\rho_{12}}{\mathrm{d}t} = i\frac{\Omega_0}{2}\mathrm{e}^{i\Delta\omega t}(\rho_{11} - \rho_{22}) - \frac{\Gamma}{2}\rho_{12} = \frac{\mathrm{d}\rho_{21}^*}{\mathrm{d}t}. \tag{2.46}$$

If we make the substitution $\tilde{\rho}_{21} = \rho_{21}e^{i\Delta\omega t}$ and $\tilde{\rho}_{12} = \rho_{12}e^{-i\Delta\omega t}$ the optical Bloch equations simplify to

$$\frac{\mathrm{d}\rho_{22}}{\mathrm{d}t} = i\frac{\Omega_0}{2}\tilde{\rho}_{21} - i\frac{\Omega_0^*}{2}\tilde{\rho}_{12} - \Gamma\rho_{22} = -\frac{\mathrm{d}\rho_{11}}{\mathrm{d}t} \tag{2.47}$$

$$\frac{\mathrm{d}\tilde{\rho}_{12}}{\mathrm{d}t} = i\frac{\Omega_0}{2}(\rho_{11} - \rho_{22}) - \frac{\Gamma}{2}\rho_{12} - i\Delta\omega\tilde{\rho}_{12} = \frac{\mathrm{d}\tilde{\rho}_{21}^*}{\mathrm{d}t}. \tag{2.48}$$

Now we may look for an expression for the steady state excited population of the driven two-level system in terms of the parameters Ω_0, Γ and $\Delta\omega$. Using $\tilde{\rho}_{12} = \tilde{\rho}_{21}^*$ and the conservation of population $\rho_{11}+\rho_{22} = 1$, and imposing the steady state condition $d\rho/dt = 0$ we get the solution for the excited population

$$\rho_{22} = \frac{\frac{1}{4}|\Omega_0|^2}{\Delta\omega^2 + \frac{1}{4}\Gamma^2 + \frac{1}{2}|\Omega_0|^2}. \tag{2.49}$$

It is useful to define the saturation parameter $s_0 = 2\Omega^2/\Gamma^2$ giving an expression

$$\rho_{22} = \frac{s_0/2}{1 + s_0 + 4\left(\frac{\Delta\omega}{\Gamma}\right)^2}. \tag{2.50}$$

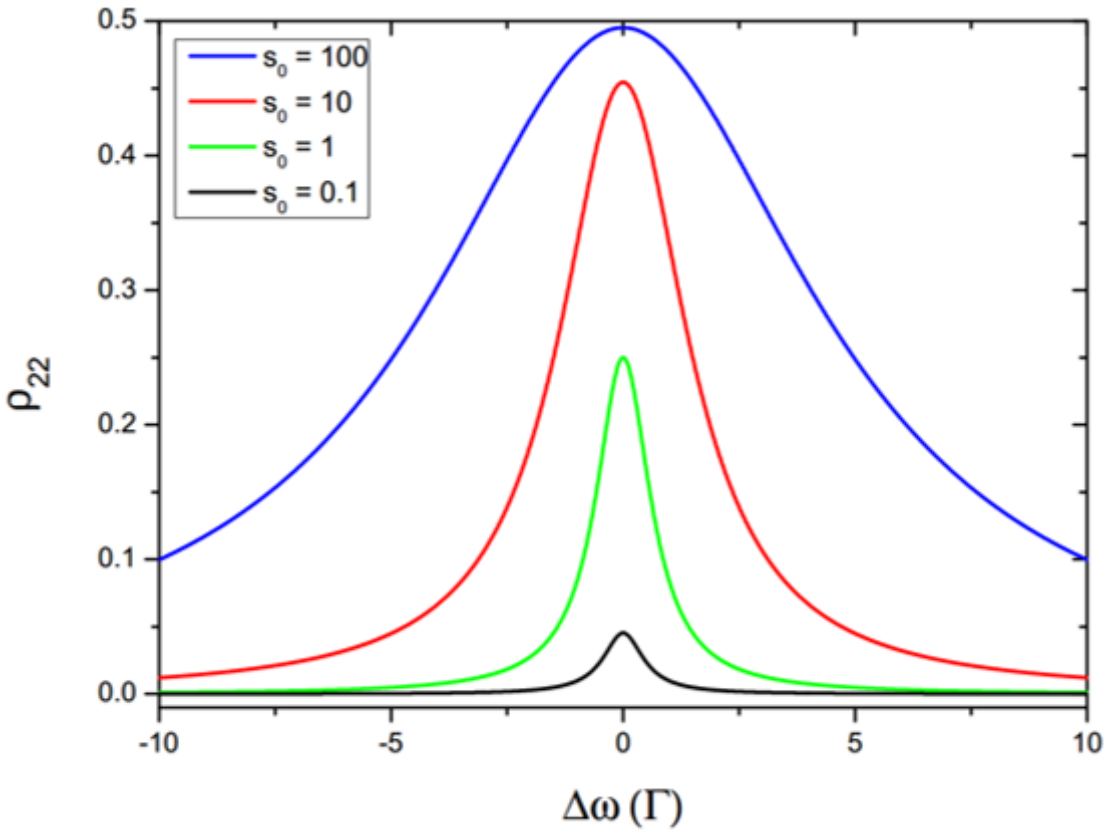

Figure 2.4: Population in the excited state ρ_{22} as a function of detuning. Behaviour is shown for various values of the saturation parameter s_0. Detuning is in units of Γ. Image taken from [44].

This Lorentzian expression leads directly to a prediction of the outcome of a measurement of the fluorescent scatter from a stationary particle, in which the fluorescence rate is the product of the upper state population ρ_{22} and the decay rate Γ. Figure 2.4 shows the lineshapes as a function of detuning from resonance for a number of different intensities. Higher laser intensities increase the rate of stimulated emission causing the population in the excited state to asymptotically approach 0.5. Away from resonance, the excited state population still goes up with laser intensity leading to an effect known as power broadening of the transition.

The next section describes the way in which laser Doppler cooling takes advantage of the fluorescence profile as a way to reduce the motional energy of the ion along the direction of the propagation of the laser beam.

2.2.2 Laser Doppler cooling

An atom in the presence of a high intensity laser beam close to resonance experiences two forces: a conservative force proportional to the gradient of the light intensity, known as the dipole force; and a dissipative force proportional to the intensity known classically as radiation pressure. The results derived in the preceding subsection will now be used to provide a theoretical framework for the technique by which the ion is localized in the trap, laser Doppler cooling. Finally it will be shown that there is a minimum theoretical temperature attainable through this method of cooling called the Doppler cooling limit, T_{D}.

In the presence of a beam of laser light of wavevector $\vec{k}$, an atom will gain momentum $\hbar\vec{k}$ each time a photon is absorbed. Upon spontaneous decay, the photon is re-emitted in a random direction, with the time-averaged force due to these emission events equaling zero, so that there is a net force in the direction of propagation of the light. The rate at which this process happens is proportional to the decay rate of the excited state of the atom. By detuning the laser to the red side of resonance with a fast atomic transition, this process may be used to cool the atom's motion thanks to the Doppler effect. When the motion has a component in the direction opposite to the direction of propagation of the light, the apparent frequency in the frame of the atom is Doppler shifted toward resonance, and the rate of scatter increases. The reverse is true for motion in the same direction as the photons in the light field. It will be shown that the force due to the increase in scatter is proportional to the atom's velocity and hence it amounts to a viscous damping force.

The force F_0 felt by a stationary atom when scattering laser light is equal to the product of the momentum transfer per photon and the rate of scattering:

$$\vec{F_0} = \hbar\vec{k}\Gamma\frac{s_0/2}{1+s_0+4\left(\frac{\Delta\omega}{\Gamma}\right)^2}. \tag{2.51}$$

From here we drop the vector overbars. Let the atom have a component of velocity v_k in the direction anti-parallel to the k vector of the laser. The shift δ in apparent frequency of the detuned laser due to v_k is $v_k k$ so that the apparent detuning $\Delta\omega \to \Delta\omega+\delta = \Delta\omega+v_k k$. Now the force on the atom is

$$F = \hbar k\Gamma\frac{s_0/2}{1+s_0+4\left(\frac{(\Delta\omega+v_k k)}{\Gamma}\right)^2}. \tag{2.52}$$

The velocity dependent force is Taylor expanded about $v_k = 0$ to give

$$F \approx F_0 + F_{\mathrm{Dopp}} \tag{2.53}$$

where F_{Dopp} is the contribution due to the motion of the ion. This second term in the expansion is

$$F_{\mathrm{Dopp}} = -\frac{4\hbar k^2 \Delta\omega v_k}{\Gamma} \cdot \frac{s_0}{\left(1 + s_0 + 4\left(\frac{\Delta\omega}{\Gamma}\right)^2\right)^2} = \beta v_k. \tag{2.54}$$

F_0 is the constant force felt by the stationary atom, and βv_k is a damping force which is a function of the instantaneous velocity of the atom along the direction of the laser. The effect of this force is to dampen the motion of the ion, reducing its kinetic energy. The rate of change of kinetic energy of an ion of mass m is

$$\frac{dE_{\mathrm{cool}}}{dt} = \frac{d}{dt}\left(\frac{1}{2}mv_k^2\right) = mv_k\frac{dv_k}{dt} = v_k F_{Dopp} = -\beta v_k^2. \tag{2.55}$$

Now we consider sources of heating of the ion due to the interaction with the laser. While the time-averaged momentum transfer due to the randomly directed emission events is zero, they contribute to a net heating of the ion due to stochastic fluctuations in the rate of this process. Also contributing to heating the ion is a stochastic fluctuation in the force F_0 due to the Poissonian distribution of photon arrival times in the laser beam. It can be shown using the statistics of diffusion and random walks [45] that the rate of change in energy due to these heating processes is

$$\frac{dE_{\mathrm{heat}}}{dt} = 2\frac{(\hbar k)^2 \Gamma}{m}. \tag{2.56}$$

We choose a detuning of $\Delta\omega = -\Gamma/2$ to maximize the slope of the Lorentzian function at which the cooling takes place. This maximizes the cooling rate. To minimize the heating rate we minimize the intensity in the cooling beam so that $s_0 \to 0$. Setting Eqs. (2.55) and (2.56) equal for the case where equilibrium is reached, and defining a temperature by $mv_k^2/2 = k_{\mathrm{B}}T/2$ where k_{B} is Boltzmann's constant we arrive at the key result:

$$T_{\mathrm{D}} = \frac{\hbar\Gamma}{2k_{\mathrm{B}}}. \tag{2.57}$$

This is the Doppler cooling limit T_{D}, reached when the cooling rate is maximized and the heating due to scattering events is minimized. For the 397 nm transition in $^{40}Ca^{+}$ T_{D} is 532 μK. Chapter 4 describes the experimental attainment of temperatures close to this limit.

2.2.3 Three- and five-level systems

The expressions in section 2.2.1 have been derived for a two-level atom in a laser field and the description of laser Doppler Cooling above only considers two levels. In reality, however, cooling $^{40}Ca^{+}$ entails coupling at least three levels with lasers addressing two

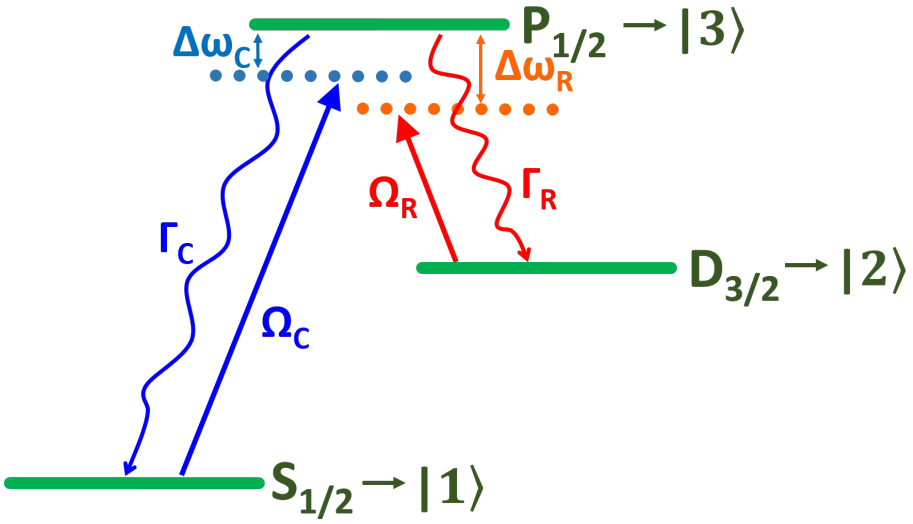

Figure 2.5: Laser Doppler cooling in a three-level lambda-type system. The cooling laser Ω_C couples states $S_{1/2}$ and $P_{1/2}$, while a repump laser Ω_R couples states $D_{3/2}$ and $P_{1/2}$. The detunings are $\Delta\omega_C$ and $\Delta\omega_R$, and the decay rates from the $P_{1/2}$ level are Γ_C and Γ_R. The states $S_{1/2}$, $D_{3/2}$ and $P_{1/2}$ are relabeled $|1\rangle$, $|2\rangle$ and $|3\rangle$ to simplify the notation in the optical Bloch equations for the three-level system.

transitions. While exploring the dynamics explicitly for the three level case, it will be shown that optimal cooling close to the Doppler limit requires a cooling scheme which employs five levels.

Three-level system coupled by two lasers

We begin by examining the cooling dynamics for the closed three level system illustrated in Fig.2.5. Doppler cooling is achieved by scattering on the 397 nm $S_{1/2}$ to $P_{1/2}$ transition but there is 8% probability of decay to the $D_{3/2}$, necessitating a repumper laser at 866 nm on the $D_{3/2}$ to $P_{1/2}$ transition to repopulate the $P_{1/2}$ level. While this is a feasible scheme for laser cooling, such a three-level system is not appropriate for cooling to close to the Doppler limit because the line shape of the absorption spectrum is no longer Lorentzian, as it is for a two-level system, and in addition the spectrum is broadened by the repumper. We explore the dynamics of the three level system for two reasons: to introduce and justify the use of a five-level system coupled by three lasers for a more sophisticated optimal cooling scheme; and to provide a theoretical basis for the dark resonance spectroscopy described in section 3.2.2. Kevin Sheridan (ITCM) explored the dynamics of 3-level and 5-level systems as part of his PhD thesis [42] in order to investigate the relative merit of

the two cooling schemes, and his results are reproduced in this section and the next. The optical Bloch equations for the three-level system are presented and absorption spectra for different 397 nm laser powers calculated.

The cooling laser with Rabi frequency Ω_C is detuned $\Delta\omega_C$ from resonance with the cooling transition $S_{1/2}$ to $P_{1/2}$, and the repumper with Rabi frequency Ω_R has detuning $\Delta\omega_R$ from resonance with the $D_{3/2}$ to $P_{1/2}$ transition. The Hamiltonian for the system contains two interaction parts

$$\hat{H} = \hat{H}_A + \hat{V}_{SP}(t) + \hat{V}_{DP}(t), \tag{2.58}$$

given by

$$\hat{V}_{DP}(t) = \hat{\mu}_{DP} \cdot \vec{E}_R(t), \tag{2.59}$$

$$\hat{V}_{SP}(t) = \hat{\mu}_{SP} \cdot \vec{E}_C(t). \tag{2.60}$$

To simplify the notation the states are relabeled as indicated in Fig.2.5:

$$\begin{aligned} S_{1/2} &\rightarrow |1\rangle \\ D_{3/2} &\rightarrow |2\rangle \\ P_{1/2} &\rightarrow |3\rangle. \end{aligned} \tag{2.61}$$

The five optical Bloch equations which describe the dynamics are

$$\frac{d\rho_{11}}{dt} = i\frac{\Omega_C}{2}\left(\tilde{\rho}_{13} - \tilde{\rho}_{31}\right) + \Gamma_C\rho_{33}, \tag{2.62}$$

$$\frac{d\rho_{22}}{dt} = i\frac{\Omega_R}{2}\left(\tilde{\rho}_{23} - \tilde{\rho}_{32}\right) + \Gamma_R\rho_{33}, \tag{2.63}$$

$$\frac{d\tilde{\rho}_{12}}{dt} = i\left(\Delta\omega_D - \Delta\omega_C\right)\tilde{\rho}_{12} + i\frac{\Omega_R}{2}\tilde{\rho}_{13} - i\frac{\Omega_C}{2}\tilde{\rho}_{32}, \tag{2.64}$$

$$\frac{d\tilde{\rho}_{13}}{dt} = i\frac{\Omega_C}{2}\left(\rho_{11} - \rho_{33}\right) + i\frac{\Omega_R}{2}\tilde{\rho}_{12} - i\Delta\omega_C\tilde{\rho}_{13} - \frac{\Gamma_C + \Gamma_R}{2}\tilde{\rho}_{13}, \tag{2.65}$$

$$\frac{d\tilde{\rho}_{23}}{dt} = i\frac{\Omega_R}{2}\left(\rho_{22} - \rho_{33}\right) + i\frac{\Omega_C}{2}\tilde{\rho}_{21} - i\Delta\omega_R\tilde{\rho}_{23} - \frac{\Gamma_C + \Gamma_R}{2}\tilde{\rho}_{23}. \tag{2.66}$$

The steady state solution for the excited P level is

$$\rho_{33} = \frac{4\left(\Delta\omega_C - \Delta\omega_R\right)^2\Omega_C^2\Omega_R^2\left(\Gamma_D + \Gamma_R\right)}{Z} \tag{2.67}$$

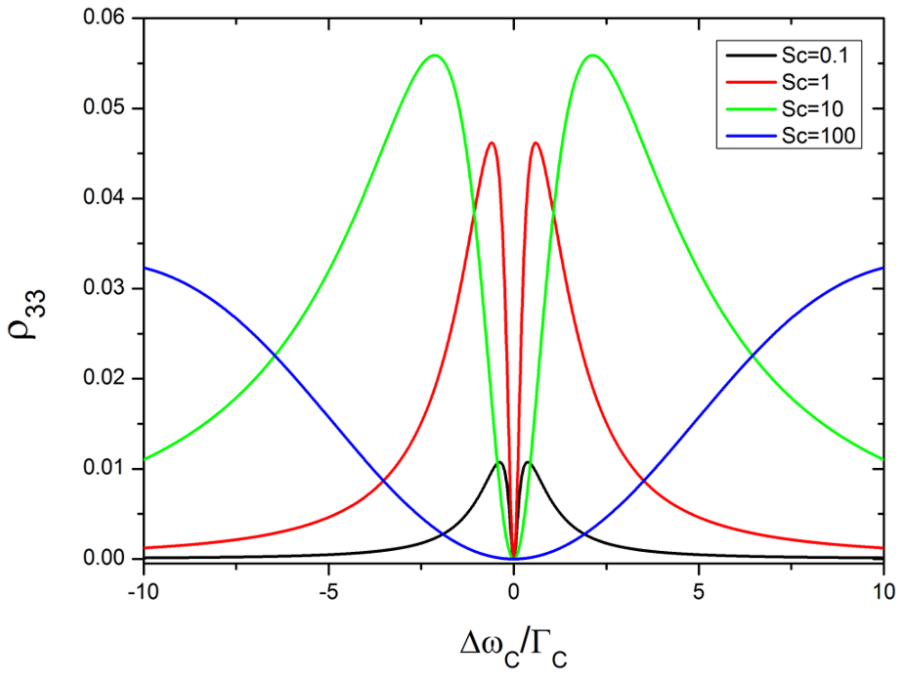

Figure 2.6: Excited state probability ρ_{33} as function of detuning of cooling laser $\Delta\omega_C$. The detuning of the repump laser is set to zero, and curves are shown for various values of the cooling laser saturation parameter. The repumper saturation parameter is set equal to 1. Figure taken from [42].

with the denominator

$$\begin{aligned} Z = & 8\left(\Delta\omega_C - \Delta\omega_R\right)^2 \Omega_C^2 \Omega_R^2 \left(\Gamma_D + \Gamma_R\right) \\ & + 4\left(\Delta\omega_C - \Delta\omega_R\right)^2 \left(\Gamma_D + \Gamma_R\right)^2 \left(\Omega_C^2 \Gamma_R + \Omega_R^2 \Gamma_C\right) \\ & + 16\left(\Delta\omega_C - \Delta\omega_R\right)^2 \left(\Delta\omega_C^2 \Omega_R^2 \Gamma_C + \Delta\omega_R^2 \Omega_C^2 \Gamma_R\right) \\ & - 8\Delta\omega_C \left(\Delta\omega_C - \Delta\omega_R\right) \Omega_R^4 \Gamma_C + 8\Delta\omega_R \left(\Delta\omega_C - \Delta\omega_R\right) \Omega_C^4 \Gamma_R \\ & + \left(\Omega_C^2 + \Omega_R^2\right)^2 \left(\Omega_C^2 \Gamma_R + \Omega_R^2 \Gamma_C\right). \end{aligned} \tag{2.68}$$

The excited state population as a function of the cooling laser detuning is plotted in Fig. 2.6 for various cooling laser intensities. The detuning and saturation parameter of the repump laser are held at zero and 1 respectively. A dark resonance forms a dip when the detunings of the two lasers are the same. This is due to coherent population trapping, in which the time evolution of the system stops when it is in a superposition of just states in the $S_{1/2}$ and $D_{3/2}$ levels. The result is an undesirable distortion of the cooling transition lineshape, with an increase in temperature at the Doppler cooling limit. We therefore employ a cooling scheme which mitigates this effect, described in the next section.

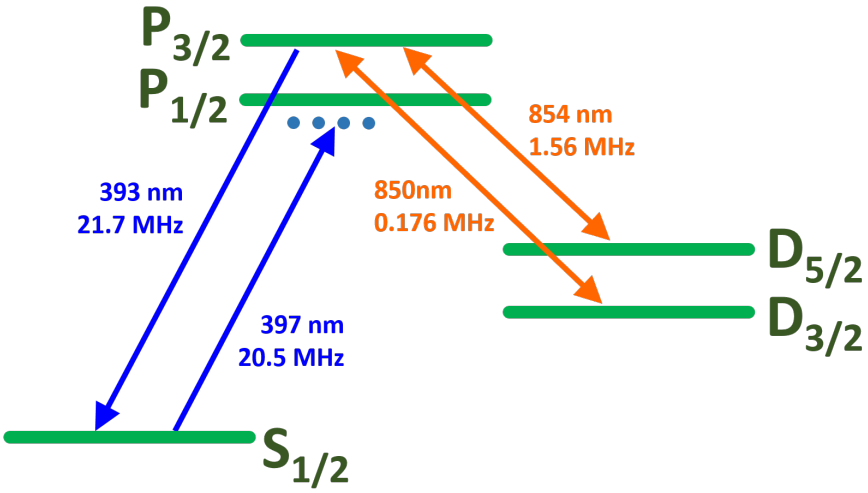

Figure 2.7: Optimal Doppler cooling with five-level system. When the ion decays to a dark state it is repumped to the $P_{3/2}$ level, decoupling the repumper lasers from the cooling transition.

Five-level system coupled by three lasers

The cooling scheme used to achieve ion temperatures close to the Doppler cooling limit is shown in Fig.2.7. With two repumpers at 850 nm and 854 nm, additional levels in $^{40}Ca^{+}$ are accessed. Population in $D_{3/2}$ is repumped by the 850 nm beam to $P_{3/2}$ and from there the ion decays to $S_{1/2}$, $D_{3/2}$ or $D_{5/2}$. The $D_{5/2}$ level is evacuated to $P_{3/2}$ by the 854 nm beam. In this way the repumping is decoupled from the $P_{1/2}$ level, to mitigate the problems associated with the coupled three-level system. The dynamics of the five-level system were modeled by Kevin Sheridan in [42], and he shows through a measurement of the saturation intensity and natural linewidth of the cooling transition that the dynamics are well approximated by those of a two-level system.

2.3 Elementary CQED theory

So far we have considered the resonant interactions of atoms in free space with photons from external laser sources. Atom-photon interactions are enhanced when the atom is placed inside an optical cavity whose length is tuned to be resonant with an atomic transition. This section introduces some of the properties of optical cavities, before highlighting some key results from CQED which govern the dynamics of our ion-cavity system. Of particular interest is the use of the ion-cavity CQED system to drive cavity-assisted Raman transitions. Detection of the cavity emission produced during this process underpins all

of the experimental results in chapters 4 and 5, and is critical in our schemes for eventual ion-ion entanglement and cluster state generation.

Optical cavities

A concise introduction to optical cavities in the context of CQED can be found in *Quantum Optics* by Fox [46], with explanations of the background to the equations in this section. Further details on optical cavities can be found in classical optics texts.

A Fabry-Perot cavity of length L supports a longitudinal light mode consisting of a standing wave of frequency ω_{C} and wavelength λ_{C} when the cavity length is equal to an integer number n half wavelengths. This is the condition for resonance,

$$L = n\frac{\lambda_{\mathrm{C}}}{2} = n\frac{\pi c}{\omega}. \tag{2.69}$$

The modes recur for changes of cavity length equivalent to a frequency interval known as the free spectral range (FSR):

$$FSR = \frac{c}{2L}. \tag{2.70}$$

When changing the cavity detuning from one side of resonance to the other, the intensity of the standing wave mode is a Lorentzian function of the detuning. The full width at half maximum of this function is the cavity line width, δ. Real cavity mirrors introduce losses in the system due to transmission and scattering. The electric field inside a cavity decays due to the mirror losses at a rate κ, so the intensity decays at a rate 2κ. The rate of this decay is inversely proportional to the round-trip time for the light propagating in the cavity. The line width and decay rate are related by

$$\kappa = \frac{2\pi\delta}{2}, \tag{2.71}$$

and the cavity finesse $\mathcal{F}$ is defined

$$\mathcal{F} = \frac{FSR}{\delta}. \tag{2.72}$$

Application of CQED - the cavity-assisted Raman transition

This section gives a description of the cavity-assisted Raman transition, in which a laser addresses an ion coupled to the cavity mode. This drives an electronic transition between two long-lived states in the ion, and a photon is emitted into the cavity. If one of the cavity mirrors is less reflective than the other, a detection system mode-matched to the output of the former has a high probability of detecting the emitted photon. This process is central to the multi-ion coupling experiments in chapter 4, because the rate of photon emission is

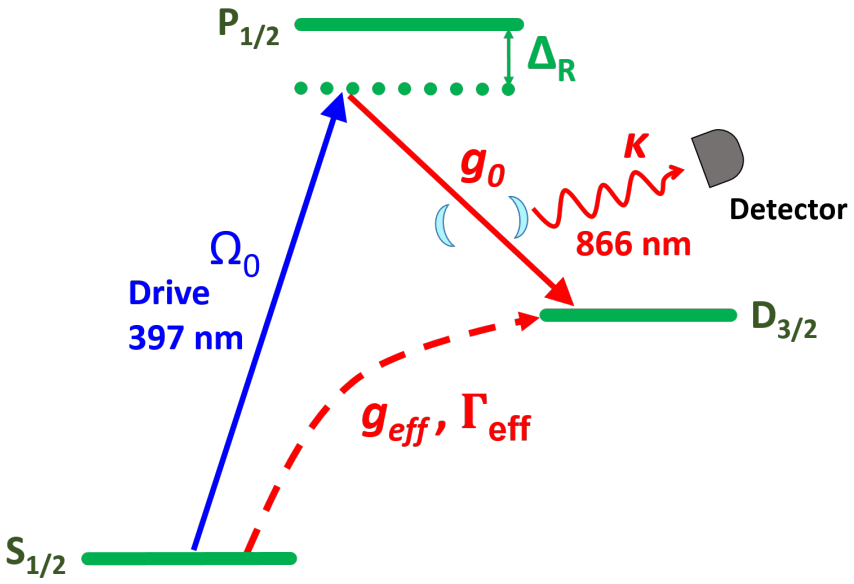

Figure 2.8: Cavity-assisted Raman transition. With a Raman detuning Δ_{R}, the drive laser with Rabi frequency Ω_0 and the cavity with coupling strength g_0 couple the $S_{1/2}$ and $D_{3/2}$ states with an effective coupling rate g_{eff} and effective linewidth Γ_{eff}. The decay rate of the cavity is κ.

a function of the degree of coupling of the ions to the cavity. In the experiments in chapter 5, the process results in the emission of single polarized photons as two discrete atomic quantum states are coherently coupled. The description of the cavity-assisted Raman transition here is not exhaustive, but a more rigorous analysis of the dynamics can be found in [47]. The equations in this section are taken from that source, as well as [20].

Even in the absence of an external light source to excite it, a cavity nonetheless contains vacuum energy with an electric field amplitude in the TEM_{00} Gaussian mode

$$\mathcal{E}_0 = \sqrt{\frac{\hbar\omega_{\mathrm{C}}}{2\epsilon_0 V}} \tag{2.73}$$

where ϵ_0 is the permittivity of free space and V is the mode volume of the cavity. When an atom is confined in the mode of a cavity with a detuning close to the frequency of a transition between two atomic energy levels, the standing wave couples the energy levels. The rate of this coupling is g_0 and is proportional to the product of the cavity field amplitude $\mathcal{E}_0$ and the atomic dipole matrix element μ_{12}:

$$g_0 = \frac{2\mu_{12}\mathcal{E}_0}{\hbar}. \tag{2.74}$$

Of particular importance to the CQED experiments in this thesis is the ability to drive cavity-assisted Raman transitions. This is a Raman process in which a free-space drive

laser with Rabi frequency Ω_0 addresses the ion and couples one branch of the transition, while the vacuum field of the cavity provides the other. Consider the lambda-type structure in $^{40}Ca^{+}$ consisting of the $S_{1/2}$ ground state, the $P_{1/2}$ excited state and the $D_{3/2}$ long-lived state, shown in Fig.2.8. The ion is placed inside a cavity which is detuned Δ_R from resonance with the 866 nm transition between the $D_{3/2}$ level and the $P_{1/2}$. A drive laser Ω_0 is switched on, detuned Δ_R from resonance with the $S_{1/2}$ to $P_{1/2}$ transition. The Raman condition is that the detuning of the cavity and laser from the $P_{1/2}$ state are equal. There is now a coupling between the $S_{1/2}$ and the $D_{3/2}$ states and the ion may undergo a coherent transition between the two, with some probability of incoherent spontaneous decay from the $P_{1/2}$ level. The effective coupling rate between the $S_{1/2}$ and the $D_{3/2}$ levels, g_{eff} is

$$g_{\text{eff}} = \frac{\Omega_0 g_0}{2\Delta_R} \tag{2.75}$$

and the effective line width of the transition Γ_{eff} is

$$\Gamma_{\text{eff}} = \Gamma \left(\frac{\Omega_0}{2\Delta_R} \right)^2, \tag{2.76}$$

where Γ is the decay rate from the $P_{1/2}$ level. Energy is conserved through the emission of a 866 nm photon into the cavity mode. By mode-matching a detection system to the (higher transmissivity) output mirror of the cavity, the emission is detected.

Our proposed schemes for heralded entanglement generation, discussed in the next section, require that the photons produced in this way are indistinguishable in time. Any scattering events from the $P_{1/2}$ will delay the production of a heralding photon, compromising the fidelity of the entanglement. To minimize the incoherent scatter, the Raman detuning may be increased to reduce the effective decay rate. To compensate for the drop in the effective coupling rate, the laser power may be turned up. This is an example of how the CQED parameters may be engineered. Another example is presented in section 5.1 of chapter 5, where distinct cavity-assisted Raman transitions are resolved by narrowing the line widths through a large detuning.

2.4 Ion-ion entanglement and cluster state generation

The ultimate aim of our CQED setup is to produce entangled pairs of ions in a string, before fusing the pairs into cluster states to act as a substrate for experiments in measurement-based quantum computation. This section presents some possible entanglement schemes, beginning with a simple example to illustrate the principle, before describing a more sophisticated scheme with higher inherent fidelity and which fulfills the requirements set by

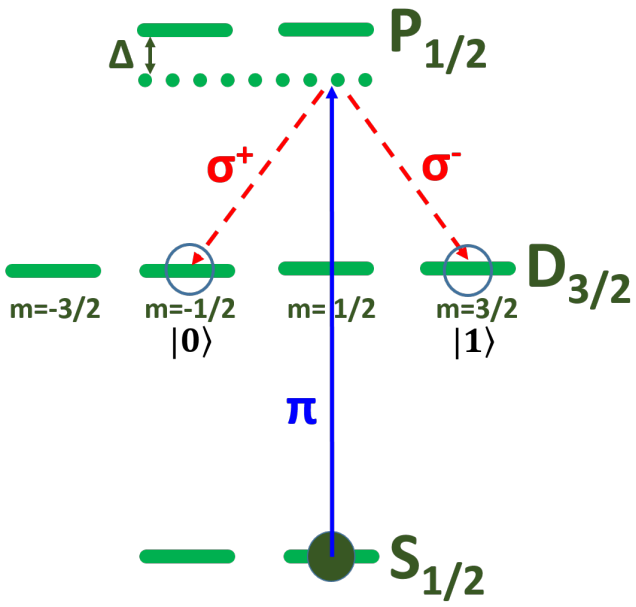

Figure 2.9: Example of a cavity-assisted Raman transition for heralded entanglement of two ions. A π-polarized drive laser couples the initialized $\left|S_{1/2}, m = 1/2\right\rangle$ state to two possible final states $\left|D_{3/2}, m = -1/2\right\rangle = |0\rangle$ and $\left|D_{3/2}, m = 3/2\right\rangle = |1\rangle$ via the σ^+ and σ^- transition paths shown. With two ions simultaneously driven, measurement of two orthogonally polarized photons in the cavity emission heralds entanglement. The drive laser and cavity length share a Raman detuning Δ from resonance.

the subsequent generation of cluster states. This is followed by a proposal for fusion of entangled ion pairs into 1-D and 2-D cluster states.

2.4.1 Probabilistic (heralded) ion-ion entanglement

The ion-ion entanglement schemes available in our system are probabilistic. Each time an attempt is made at entanglement, success is heralded by a certain measurement outcome, otherwise the attempt is discarded and the run repeated. The schemes are similar to that proposed by Duan and Kimble [18] and two-ion entanglement has been successfully demonstrated by the Innsbruck group [17]. In our schemes, cavity-assisted Raman transitions are driven in two ions simultaneously coupled to the common cavity mode, resulting in the emission of two photons. The initial state may be in the $S_{1/2}$ or $D_{3/2}$ manifolds and the final states are in the $D_{3/2}$ manifold, so the photons emitted into the cavity have a wavelength of 866 nm. The final states of the ions are entangled with the polarization states of the photons. The cavity erases which-way information connecting a photon to an ion, so ion-ion entanglement is heralded by the successful measurement of orthogonally

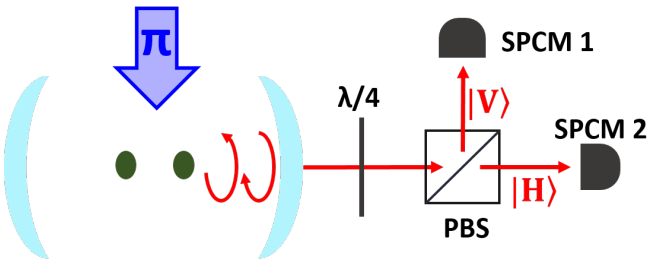

Figure 2.10: Setup for heralded entanglement of two ions. A π-polarized drive laser mediates the cavity-assisted Raman transition causing the emission of two photons of circular polarization into the cavity mode. A quarter wave plate ($\lambda/4$) linearizes the polarization and a polarizing beam splitter (PBS) splits the polarization components for detection in single photon counters (SPCM).

polarized photons in the cavity emission. The measurement result is probabilistic, and the scheme is therefore an example of probabilistic ion-ion entanglement.

A possible scheme is as follows. Figure 2.9 shows a cavity-assisted Raman transition in which the ion has been initialized in the state $\left|\mathrm{S}_{1/2}, m = 1/2\right\rangle$. A drive laser, polarized to excite only π transitions, is switched on. The population is transferred to a superposition of the $\left|\mathrm{D}_{3/2}, m = -1/2\right\rangle$ and $\left|\mathrm{D}_{3/2}, m = 3/2\right\rangle$ states, labeled $|0\rangle$ and $|1\rangle$ respectively, with the emission of a photon into the cavity. A small magnetic field defines a quantization axis parallel to that of the cavity, so that only σ^+ and σ^- transitions are possible in the cavity-assisted branches, with the accompanied emission into the cavity of right-circularly polarized $|\mathrm{R}\rangle$ and left-circularly polarized $|\mathrm{L}\rangle$ photons respectively. Measurement of a right-circularly polarized photon in the cavity emission indicates that the ion is in the $|0\rangle$ state and a left-circularly polarized photon indicates that the ion is in $|1\rangle$. In practice a quarter wave plate is inserted at the output of the cavity to transform circular into the horizontal and vertical linear polarization basis: $|\mathrm{R}\rangle \rightarrow |\mathrm{H}\rangle$ and $|\mathrm{L}\rangle \rightarrow |\mathrm{V}\rangle$. The measurement is carried out by insertion of a polarizing beam splitter (PBS) after the quarter wave plate and placing single photon detectors at each of its outputs. The transient entanglement of the ion with the photon may be written

$$|\Psi\rangle = \frac{1}{\sqrt{2}} \left(|0\,\mathrm{H}\rangle + |1\,\mathrm{V}\rangle \right. \tag{2.77}$$

assuming equal transition probabilities in each branch.

With two ions in the cavity, simultaneously addressed by the drive laser, two photons are emitted in the same spatial mode, and their polarization components are split at the PBS. The setup is schematically indicated in Fig. 2.10. Coincident counts at both

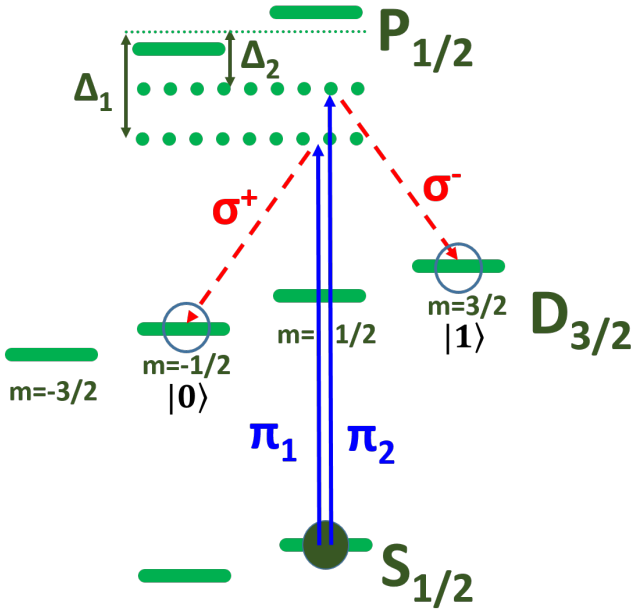

Figure 2.11: Entanglement scheme with Zeeman splitting. To accommodate significant magnetic field splitting of the $D_{3/2}$ manifold required later by the cluster state generation scheme, a bichromatic drive laser is used. It contains two frequency components π_1 and π_2 with detunings Δ_1 and Δ_2 from the unshifted $P_{1/2}$ level.

detectors heralds the measurement of orthogonally polarized photons. The total state $|\Psi_{\mathrm{TOT}}\rangle = |\Psi\rangle \otimes |\Psi\rangle$ is projected by the measurement to the entangled state [17]

$$|\Psi_{\mathrm{Ent}}\rangle = \frac{1}{\sqrt{2}} \left(|0\,1\rangle + |1\,0\rangle \right). \tag{2.78}$$

This will occur with a probability of 1/2 for all the instances where two photons are generated in the output of the PBS. The other possibilities are that both photons arrive in one or the other detector, heralding the states $|0\,0\rangle$ or $|1\,1\rangle$, in which case the run is discarded and the attempt at entanglement repeated.

It will be shown in the next section that our proposed scheme for fusion of entangled ion pairs into a cluster state requires the presence of a sufficiently large magnetic field to split the $D_{3/2}$ manifold. This is due to a requirement of the scheme that individual cavity-assisted Raman transitions should be well resolved. The two-ion entanglement scheme presented above relies on the magnetic field splitting to be less than the linewidth of the Raman transitions, in order to eliminate the possibility of energetically favouring one transition branch over the other. It is technically challenging to quickly change the strength of the magnetic field once the entangled ion pairs have been formed, as it would be necessary to adiabatically eliminate frequency components which might drive magnetic

dipole transitions between the Zeeman levels. Therefore the above scheme may be modified to admit the presence of significant magnetic shifting of the energy levels through the application of a bichromatic drive laser. The scheme is shown in Fig. 2.11. With the correct detunings Δ_1 and Δ_2 from the unshifted $P_{1/2}$ level, frequency components π_1 and π_2 have equal probability of driving the transitions σ^+ and σ^- when the Zeeman levels have shifted. Again, with two ions driven in this way, simultaneous measurement of orthogonally polarized photons at the detectors will herald entanglement of the ions.

A final extension of the scheme will be presented in which the ions are initialized in the $D_{3/2}$ manifold. This is advantageous to the fidelity of the entanglement because of the following reasoning. Any attempt at entanglement of the type using cavity-assisted Raman transitions is vulnerable to scatter from the excited $P_{1/2}$ level. In the schemes presented above, in which the ions are initialized in the $S_{1/2}$ level, several scattering events back to the $S_{1/2}$ level may occur for one or both of the ions during a shot at entanglement, delaying the successful production of the cavity photon, and a finite time interval will be measured between the cavity photon detection events. The scattering events produce measurable fluorescence, detectable by a suitable imaging system, and this information may be correlated with the arrival times of the photons emitted from the cavity. Therefore this delay gives information associating individual ions with the emitted photons. If a scattering event does occur, there is only 8% probability of scatter from the $P_{1/2}$ level to $D_{3/2}$. Therefore if the ion was initialized in the $D_{3/2}$, there is a much smaller probability of re-initialization in that level. Instead, the state is lost to the $S_{1/2}$ level and the run must be repeated before a photon can be emitted into the cavity. Therefore, the success rate (as measured by the frequency of events in which two photons are detected in the cavity emission) is lower when initializing the ions in the $D_{3/2}$ level, but the fidelity will be higher[1].

The scheme for ion-ion entanglement with ion initialization in the $\left|D_{3/2}, m = 1/2\right\rangle$ level is shown in Fig. 2.12. Initially the ions are optically pumped to the $\left|D_{3/2}, m = -3/2\right\rangle$ Zeeman level (chapter 5 contains a description of successful optical pumping to this level.) A bichromatic two-photon STIRAP pulse containing Rabi frequencies Ω_L^+ and Ω_L^- [48] then transfers the populations to the $\left|D_{3/2}, m = 1/2\right\rangle$ level. Finally a further bichromatic drive laser, this time close to resonance with the 866 nm transition, mediates an entangling cavity-assisted Raman transition of the type already described above.

[1] As a step toward eventual ion-ion entanglement, a Hong-Ou-Mandel-type interferometry experiment will be carried out to optimize the simultaneity of the cavity photon emission

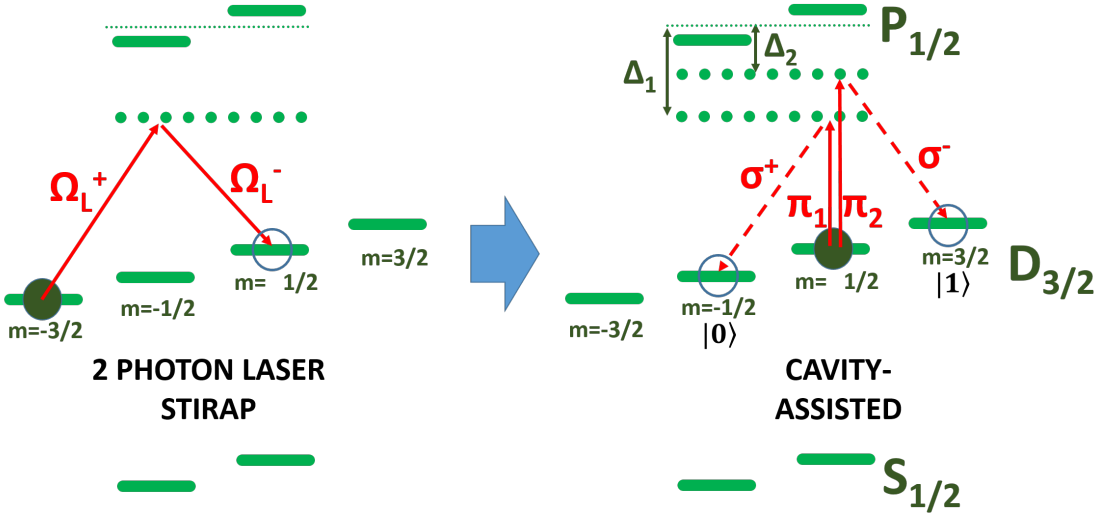

Figure 2.12: Entanglement scheme with $D_{3/2}$ initialization. The ions are optically pumped into $\left|D_{3/2}, m = -3/2\right\rangle$, before a two-photon STIRAP pulse with laser Rabi frequencies Ω_L^+ and Ω_L^- initializes the $\left|D_{3/2}, m = 1/2\right\rangle$ state (left). Then a bichromatic cavity-assisted Raman transition produces the superposition state as in the examples above.

2.4.2 Cluster state generation

An electro-optic deflector may be used entangle pairs of ions sequentially in a string following the above protocols. These pairs are to be entangled pair-wise to form a many-ion cluster state. In order to create entanglement between two pairs, an ion from each pair may be individually addressed with the electro-optic deflector and entanglement generated between these pair-partners through a parity check which is now described. A laser resonant with the cavity and close to the 866 nm transition with linear polarisation perpendicular to the magnetic field simultaneously drives σ^+ and σ^- cavity-assisted Raman transitions. The magnetic field splitting is sufficient to ensure that only transitions which return the ions to their original states are possible. This is illustrated in Fig. 2.13. Each ion emits a photon into the cavity which is associated with either $|0\rangle$ or $|1\rangle$, so that probabilistic entanglement between the pair-partner ions is heralded by coincident detection of orthogonal polarization states in the cavity emission. Two entangled pairs are thus formed into a four-ion entangled state. The process can be repeated for adjacent pairs to exponentially grow linear clusters. Additionally there is the possibility of producing two-dimensional cluster states, in which entangled pairs are fused through parity checks on alternate ions. This is shown schematically in Fig. 2.14.

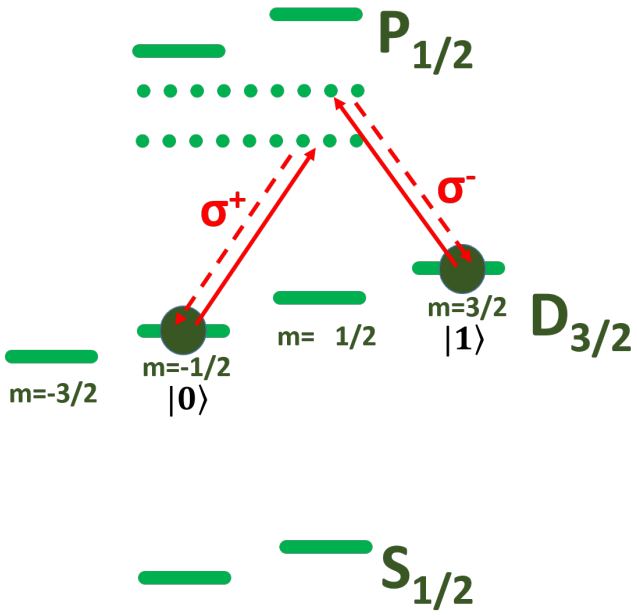

Figure 2.13: Entangled pair fusion through parity check. To fuse two entangled pairs, a partner from each pair is addressed with a laser polarized to drive only σ^+ and σ^- cavity-assisted Raman transitions. Measurement of orthogonally polarized photons in the cavity emission heralds entanglement of the partners and hence the pairs.

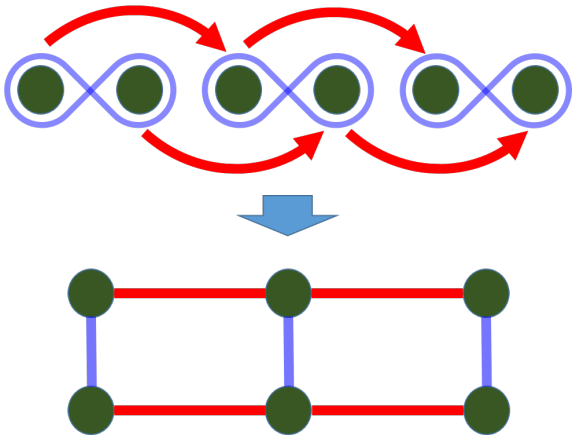

Figure 2.14: Two-dimensional cluster state. After creating entanglement between pairs of ions (blue), parity checks on alternate ions (red) fuses the pairs into a two-dimensional multi-ion entangled state.

Chapter 3

Experimental setup

The core of the apparatus is an ion trap with an integrated high finesse optical cavity, with the purpose of carrying out CQED experiments with highly localized ions as emitters. The geometry allows for strings of ions to be trapped along the axis of the TEM_{00} mode of the cavity field, enabling simultaneous equal coupling of many ions to the cavity. The structure in which the trap and cavity are mounted is housed in a vacuum chamber with electrical feedthroughs. The ion trap-cavity system and vacuum chamber were designed by Matthias Keller and built by Nicolas Seymour-Smith, Peter Blythe and Dan Crick. Lasers for cooling the ions, stabilizing the cavity length and performing experimental operations surround the chamber. An imaging system allows visualization of the ions via a CCD camera and fluorescence collection via a photomultiplier tube (PMT). A separate detection system, mode-matched to one of the cavity mirrors monitors cavity emission. In general, the lasers are locked to commercial wavemeters, but any of the infra red lasers may be frequency-locked to a stable atomic reference laser via a scanning stability-transfer cavity. Nicolas Seymour-Smith and Dan Crick built the optics, detection and laser systems, as well as the stable atomic frequency reference and scanning cavity stability transfer systems. The frequency reference was further improved by Ezra Kassa during the time that the work described in this thesis was being carried out

This chapter begins by describing the trap and associated systems including the neutral calcium oven and imaging and vacuum systems. After that there is a description of the integration of the cavity mirrors as well as details of the systems which stabilize the cavity length and detect cavity emission. Next, the laser systems necessary for trapping and cooling the ions are described. The description includes the stable atomic reference laser and the scanning cavity lock.

At the end there is a description of the routine measurements that enable the ex-

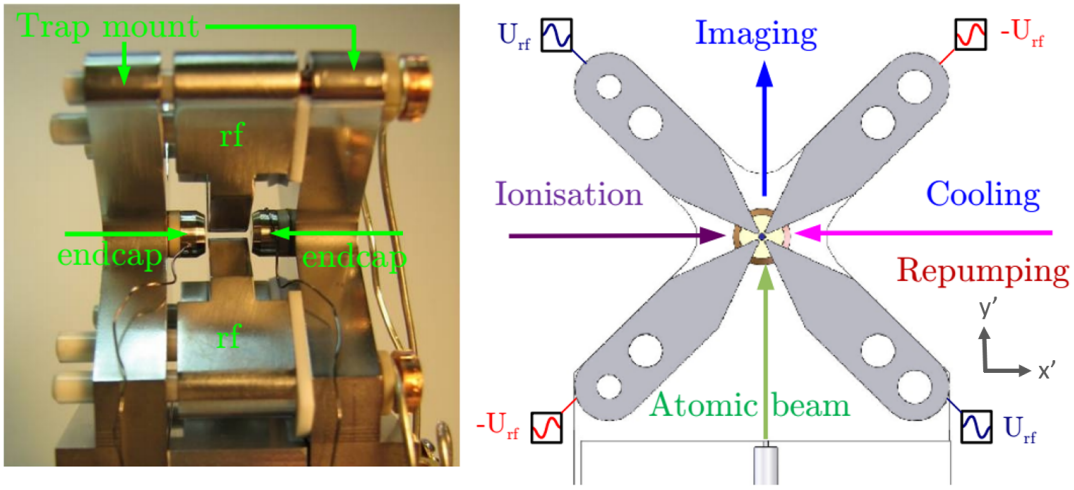

Figure 3.1: Ion trap photograph and schematic. Radial blade electrodes (with rf voltage U_{rf} indicated) and axial dc electrodes are shown with electrical connections, along with the spatial orientation of the lasers required for ion trapping, the neutral atomic beam and the imaging system. The natural horizontal and vertical axes, x' and y', are shown, and the trap axis points along z. Photograph and drawing by Nic Seymour Smith and taken from [25].

periments in later chapters, including precision spectroscopy of both the dipole-allowed cooling transition and the cavity-assisted Raman transitions, micromotion compensation, magnetic field compensation and trap secular frequency measurements.

3.1 Ion trap and associated systems

The trap is a linear rf ion trap consisting of four blade-shaped rf electrodes and two dc endcap electrodes, providing radial and axial confinement respectively. The trapped species is singly ionized calcium, $^{40}Ca^{+}$, produced by photo-ionization of neutral atoms effusing in a collimated beam from a resistively heated oven below the centre of the trap. Electrical connections are via feedthroughs incorporated in a feedthrough flange upon which the vacuum chamber is mounted. An imaging system collects fluorescence emitted during laser Doppler cooling.

3.1.1 Ion trap

The ion trap is produced monolithically with blade-shaped rf electrodes cut by the electrical discharge machining (EDM) technique from the same block of stainless steel as the

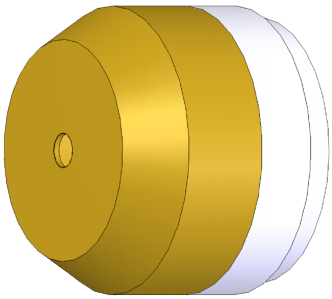

Figure 3.2: DC endcap electrode. The hollow steel electrodes are glued to plastic mounts and have holes drilled to allow cavity mode field to pass through. SolidWorks design by Matthias Keller.

trap mount structure. The blades taper to narrow edges on a square of sides 0.66 mm. The distance from the trap centre to the electrode edge is $r_0 = 0.465$ mm and the distance between the endcap electrodes $2z_0 = 5$ mm. The blade-shaped design of the rf electrodes allows for a smaller value of r_0 which yields a steeper trapping potential compared with rod-shaped designs used by the Aarhus group [26] and previously at Innsbruck [49].

Figure 3.1 shows a photograph and schematic of the trap structure without the assembly for mounting the cavity mirrors. Each rf electrode is mounted on a pair of ceramic dowels which pass through holes drilled in the trap mount and electrode. The holes are drilled before the mount and electrodes are separated by electric discharge machining. This method of construction eliminates the need for fine positioning of the rf electrodes with respect to the trap mount. Ceramic spacers ensure the blades are well centered while insulated from the trap mount and further ceramic sleeves insulate copper screws which connect the electrodes to the rf circuit.

Fig. 3.2 shows the steel dc electrodes glued to PEEK (polyether ether ketone) mounts which fit inside holes in the trap mount. PEEK is a robust polymer with a high melting point to prevent deformation when baking the vacuum system. These endcap electrodes are hollow in order to surround and shield the cavity mirrors, and have 1 mm diameter holes drilled in their faces to allow the cavity mode to pass. Spot-welded tantalum wire connects each dc endcap to the high voltage dc circuit.

There is an aluminium plate beneath the trap centre, below which the calcium oven is mounted. A 1 mm hole is drilled in this plate to collimate the divergent beam of neutral calcium emerging from the oven. The plate also serves as a structure on which to mount an excitation plate for carrying out the secular frequency measurements described in section 3.4.5.

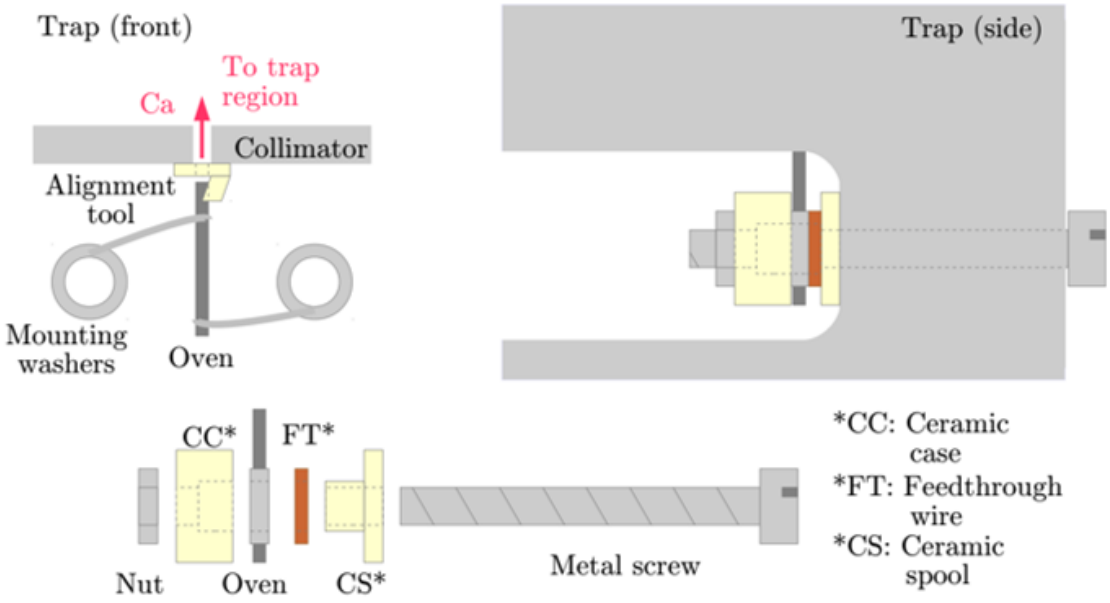

Figure 3.3: Oven mounting. A metal screw passes through the trap mount structure to the oven mounting cavity. An insulating ceramic case and spool allow a nut to clamp the oven mounting washers into electrical contact with the feedthrough wire without shorting the oven circuit. Mechanical tension in the current-carrying oven mounting wire holds it firmly against a ceramic alignment tool to ensure the effusion of calcium to the trap centre. Drawing by Nic Seymour Smith taken from [25].

The source of the neutral calcium beam ions is a stock of grated calcium metal in a tantalum tube, crimped at one end and mounted in a cavity below the collimation plate. This oven is 1 mm in diameter and about 10 mm long and is heated through spot welded contacts with tantalum wire which is resistively heated by a current source. Due to the high rate at which calcium reacts with air and water vapour, insertion of the oven in the ion trap structure is the last procedure before closing and evacuating the vacuum system. The oven electrical circuit is designed to take currents in excess of 2 A, with oven temperatures measured by Kevin Sheridan at between 500 K and 725 K for between 1.3 A and 1.9 A for similar designs [42].

The other end of the tantalum wire is spot welded to M4 mounting washers which make electrical contact with a copper wire carrying current from the oven circuit feedthroughs. The copper feedthrough wire slips over a screw which is fixed to the trap mount, and is insulated from the screw by a ceramic spool. A ceramic case insulates the oven mounting washers from a securing nut which presses together the oven mounting washer and the feedthrough wire, as shown in Fig. 3.3. Mechanical tension holds the top of the oven

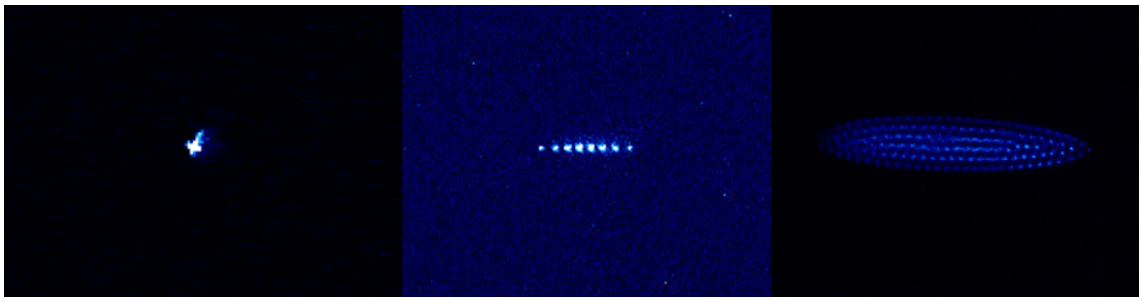

Figure 3.4: Imaging trapped ions. From left to right: a single ion, a string of eight ions and a Coulomb crystal are imaged. The axial inter ion distance is on the order of 10 μm.

against a ceramic lip which acts as an alignment tool to deliver a flux of atoms through the collimation hole to the trap centre. Photoionization of the neutral calcium is described in section 3.3.1.

3.1.2 Fluorescence imaging system

Imaging is through fluorescence photodetection by a CCD camera and an ultraviolet-sensitive photomultiplier tube (PMT). In general the system measures the 397 nm photons scattered by the ions during the cooling process, therefore there is a bandpass filter to eliminate background form other photosources. Examples of images of ions recorded by the CCD camera are presented in Fig. 3.4. The exceptions to detection at 397 nm are when the trap is illuminated by white light to image the electrodes, for example when setting up or overhauling the imaging system, or when spectroscopy is done on the 393 nm $S_{1/2}$ to $P_{3/2}$ transition outlined in section 5.2.2 of chapter 5 on coherent ion-cavity interactions. The fluorescence photodetection is completely distinct from the 866 nm detection system mode-matched to the cavity output for monitoring cavity emission.

The fluorescence photodetection system is mounted on an optical breadboard above the trap vacuum chamber. Light from the centre of the trap is magnified by a x10 objective lens mounted on a 3D micrometer positioning stage and directed horizontally after a periscope mirror. An image is formed and an iris closed around it to reduce background scatter. After passing through the bandpass filter, the light is re-focused by a lens pair. A vertical mirror fixed to a rotating light-tight turntable allows light to either pass and strike the PMT, or reflect onto a CCD camera.

The PMT outputs a TTL pulse when it detects a photon and a computer DAQ counts these pulses to provide a count rate proportional to the rate at which cooling light is scattered by the ions, permitting spectroscopy to be carried out on the ion.

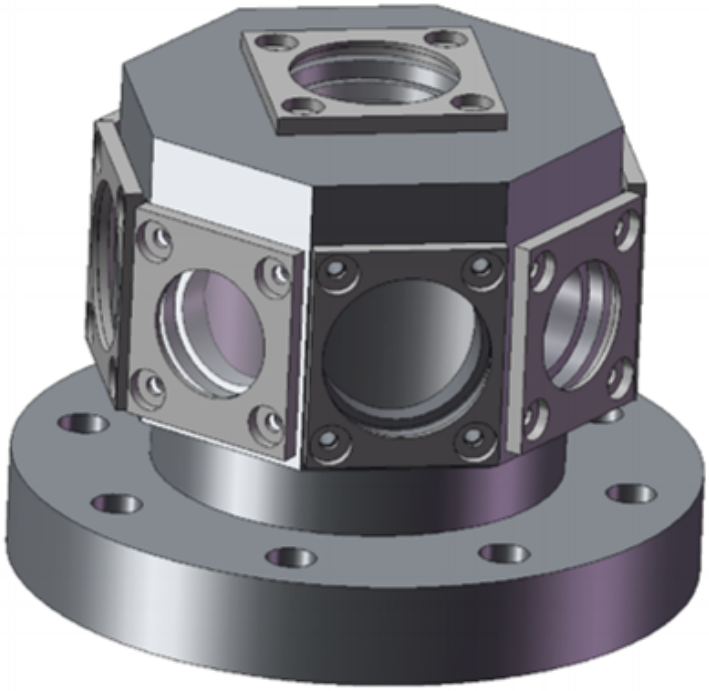

Figure 3.5: Vacuum chamber. Eight UV and IR anti reflection-coated windows allow laser beams to pass in and out of the trap centre. SolidWorks design by Matthias Keller.

3.1.3 Vacuum system

The trap is housed in a vacuum chamber bolted to a feedthrough flange with 12 electrical feedthroughs, nine of which are in use. The chamber is octagonal with eight UV and IR anti reflection-coated windows, shown in Fig. 3.5. The geometry gives good optical access while minimizing the angles of incidence of the beams. The feedthrough flange is connected to a T-piece with a valve to the exterior and an ion pump. When closed up, the system is initially evacuated with a turbo-molecular pump attached to the valve. Baking is achieved by wrapping the vacuum system in resistively heated belts, with the chamber covered by a purpose-built insulated heated shroud, and thermocouples are attached to monitor the temperature of the system at several locations. The system is then baked to up to 200°C except for temperature sensitive points such as the indium window seals and PZT material, whose temperatures are kept within specification. Additionally it is ensured that there is not a temperature gradient at the chamber windows. When baking the system an initial rise in pressure is followed by an exponential drop. When close to base pressure the system is allowed to cool and the ion pump switched on. The turbo-molecular pump is valved off and an ultra high vacuum (UHV) pressure of 10^{-10} mbar is attained.

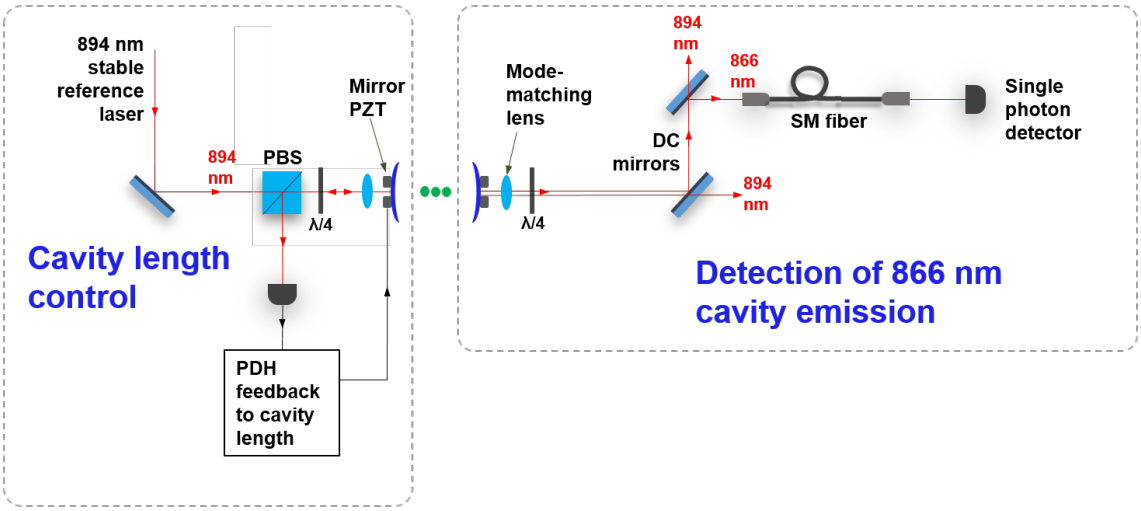

Figure 3.6: Length-locking and cavity emission detection. A stable reference laser at 894 nm generates a Pound-Drever-Hall (PDH) error signal which is fed back to one cavity mirror PZT to stabilize the length. On the other side of the cavity, the mirror with 100 ppm tranmissivity is mode-matched to a fiber which couples the cavity emission signal to the single photon counting module. Two dichroic (DC) mirrors filter the locking light from the cavity signal.

In accordance with UHV protocol, all of the trap components, vacuum plumbing and trap assembly tools are cleaned with acetone in an ultrasonic bath, and surgical gloves are worn while working on the exposed system.

3.2 Experimental cavity

A Fabry-Perot resonator is integrated into the design of the ion trap structure. Its purpose is to form an optical cavity resonant with the 866 nm $P_{1/2}$ to $D_{3/2}$ transition in $^{40}Ca^{+}$ by which the ions are coupled to the cavity mode. The cavity has a length L of 5.25 mm and a linewidth of 470 kHz at 866 nm. From these parameters we calculate that the free spectral range (FSR) is 29 GHz and, from measurements of the cavity linewidth the finesse is 60,000. The mirror radius of curvature R is 12 mm and they have transmissivities at 866 nm of 5 ppm and 100 ppm. The ratio of transmissivities give a strong directionality to the photon emission from the cavity. The waist w_0 of the cavity is 36 μm calculated from the mirror radius of curvature and the cavity length via [50]

$$w_0 = \sqrt{\frac{\lambda}{2\pi}(L(2R-L))^{1/2}}, \tag{3.1}$$

where λ is the optical wavelength at 866 nm. The mirrors are formed by coatings which are

highly reflective at 866 nm, on fused silica substrates. Each mirror substrate is mounted on a ring piezo-electric transducer (PZT) with a travel of approximately 2 μm and by exercising the full range of travel of both mirrors approximately 6 free spectral ranges are accessible. A broad range is desirable to facilitate length-stabilizing the cavity to be simultaneously resonant with the TEM_{00} mode of the 866 nm transition while close to resonance with a mode of the 894 nm reference laser. This is explained in detail in section 3.2.2. The calculated coupling strength between the ion and the cavity field is $g_0 = 0.9$ MHz calculated from an expression equivalent to Eq. (2.74)

$$g_0 = \sqrt{\frac{3c\Gamma\lambda^2}{2\pi^2 L w_0}}, \tag{3.2}$$

where c is the speed of light and $\Gamma = \Gamma_{P_{1/2}\to D_{3/2}}$ is the decay rate for the 866 nm transition.

The requirements of the CQED experiments for which the system is designed are that the cavity mode is well overlapped with the trap centre, that the cavity length is stably locked to fulfill the condition for Raman resonance and that there is a means for detecting the emisison. The first of these requirements is addressed in section 3.2.4, and the section below details the apparatus for locking the cavity length and the detection system. Figure 3.6 shows schematically how these systems occupy the experimental space on either side of the cavity.

3.2.1 Integration of the optical cavity

The high-finesse optical cavity is formed of two mirrors of radius of curvature 12 mm, held a distance 5.25 mm apart. The mirrors consist of highly reflective coatings applied to the ends of cylindrical fused silica substrates of 3 mm diameter and 10 mm length which have later been ground to a taper forming 1 mm diameter mirrors. The substrates are shown in Fig. 3.7 before integration in the trap. Each substrate is loaded into a collet, which has a reduced diameter collar for halting the travel of the substrate by the taper, shown in Fig. 3.8. A thread inside the collet admits a hollow PEEK screw to secure the substrate in place. UHV compatible glue is used to attach a ring PZT to the base of the collet, and this assembly is glued to the collet mount. In this way, once the collet mount is attached by screws through the mounting points to the side of the trap mount, the position of each mirror may be translated along the trap-cavity axis up to the distance of the travel of the PZT. This is approximately 2 μm, giving a total frequency span of approximately six free spectral ranges. See Fig. 3.9 for the full trap mount with mirror collets mounted, and Fig. 3.10 for a cutaway of the trap structure showing the integrated mirror substrates.

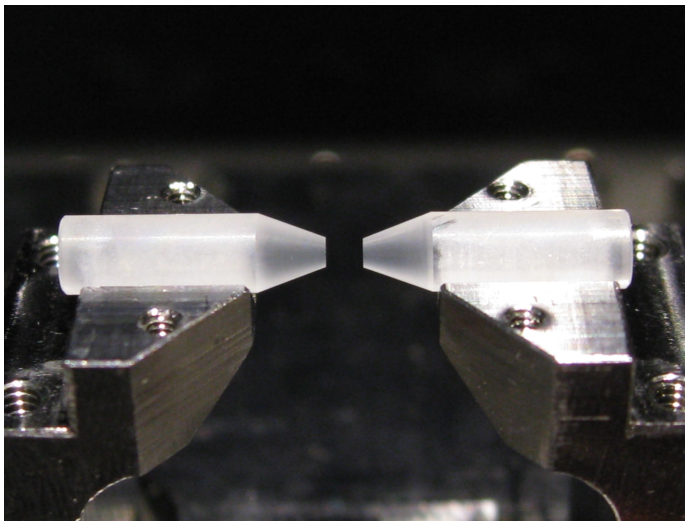

Figure 3.7: Cavity mirror substrates. A cavity is formed by the coated surfaces of the substrates.

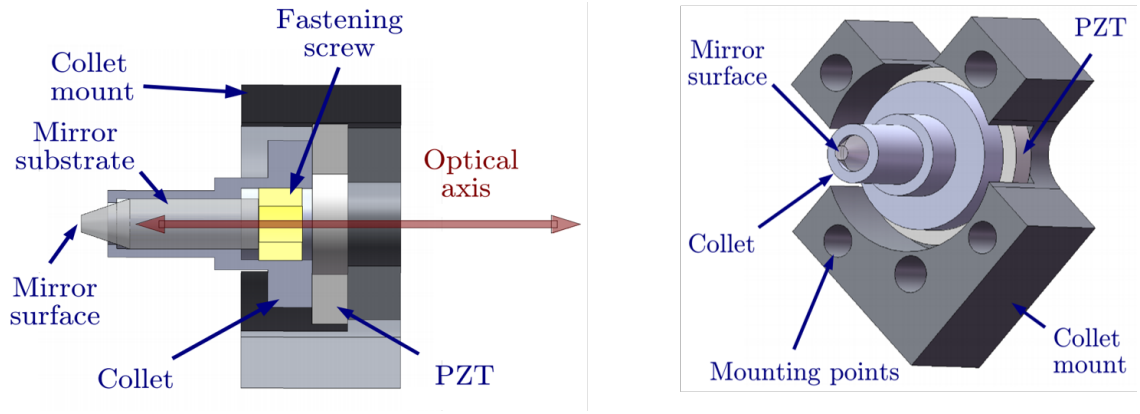

Figure 3.8: Mirrors in collet mounts. The mirrors are held in the collets by a hollow PEEK fastening screw, and the collets are glued to ring PZTs which are glued to the collet mounts. SolidWorks design by Matthias Keller and image taken from [25].

3.2.2 Cavity length stabilization

An important parameter in experiments in CQED is the linewidth of the cavity, for example in the experiments detailed in chapter 5 in which the cavity linewidth is a limiting factor. It is therefore necessary to stabilize the length of the cavity as precisely as possible. The lab contains a stable reference laser at 894 nm, described in section 3.3.2, and a fiber guides frequency-stabilized light directly to the experimental cavity. The frequency-stable beam is reflected off the 5 ppm transmissivity cavity mirror and a Pound-Drever-Hall (PDH) setup feeds back to one of the cavity PZTs to hold the cavity length constant to within a fraction of the cavity linewidth of the reference laser. The 894 nm laser is

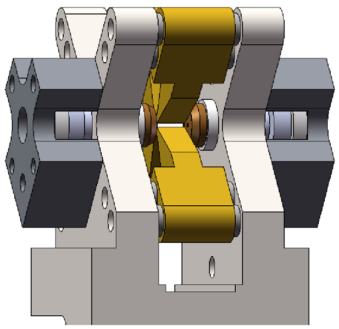

Figure 3.9: Mirror mounting. The collets are fixed in place by locating the collet mounts with respect to the trap mount structure. The precise locating procedure is detailed in section 3.2.4. SolidWorks design by Matthias Keller.

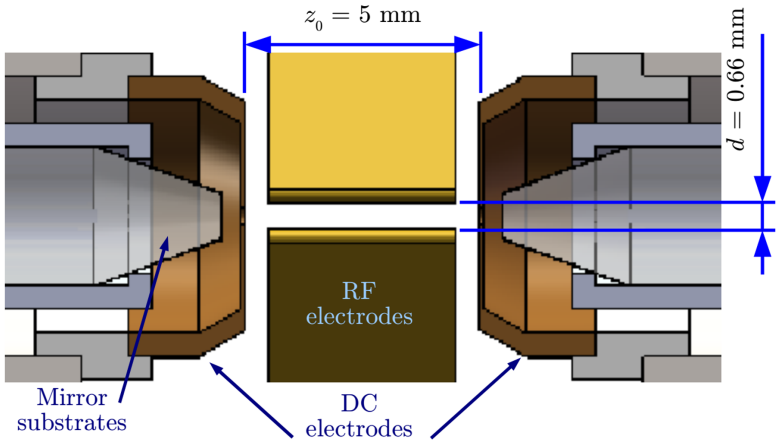

Figure 3.10: Trap electrodes and cavity mirrors. The trapping region is shielded from the dielectric cavity mirrors by the endcap structure. SolidWorks design by Matthias Keller and image taken from [25].

stabilized to a transition in caesium, therefore a frequency offset has to be introduced in order for the cavity to be resonant with the $P_{1/2}$ to $D_{3/2}$ transition. Furthermore this offset must be variable in order to smoothly change the length of the PDH-locked cavity. The scheme relies on generating two sets of sidebands on the stable 894 nm frequency. The first set is an amplified variable frequency rf signal to reduce power in the carrier frequency (locked to the caesium transition) and put power into two amplified sidebands at a variable distance from the carrier. Either of these sidebands may provide the variable locking frequency for the cavity, thanks to the second set of sidebands of fixed frequency which are used to generate the error signal for the PDH lock. Details of the scheme are now presented.

The 894 nm fiber out-coupler is rotated to emit horizontally polarized light which

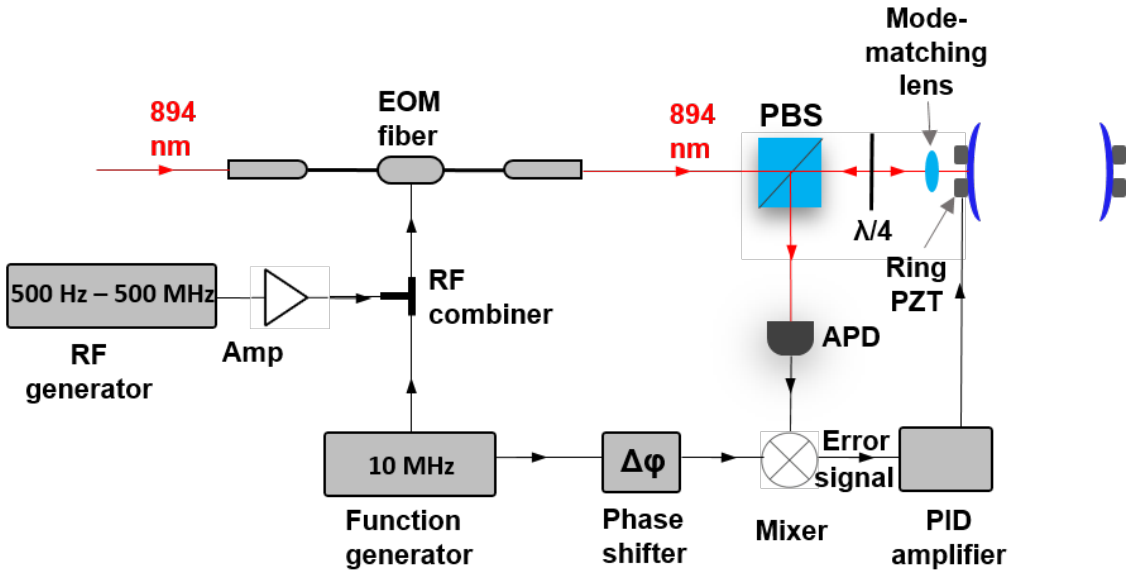

Figure 3.11: Stabilizing the cavity length. The cavity length is Pound-Drever-Hall locked to a tunable amplified sideband of a mode of the 894nm stable reference laser.

passes through a polarizing beam splitter cube (PBS), a quarter wave plate and a mode-matching lens before reflecting off the cavity. The reflected signal passes through the quarter wave plate a second time to become vertically polarized. It then reflects at the PBS and is monitored by a fast avalanche photodiode (APD). The fiber which guides the reference light at 894 nm to the experimental cavity incorporates an electro-optic modulator (EOM) so that electronically generated rf modulation signals may be added to the carrier frequency of the light. The amplified signal from an rf generator produces sidebands in an accessible frequency range of 500 Hz to 500 MHz on the 894 nm carrier, which are maximized in power with respect to the carrier. Secondary sidebands produced by a modulation signal from a function generator at 10 MHz are added to the signal at an rf power combiner. When the 10 MHz modulation signal is mixed with the reflected light signal from the APD an error signal is generated due to the 10 MHz component in the light. This is an example of the Pound-Drever-Hall locking technique. The output from the mixer is fed back to the ring PZT on the 5 ppm cavity mirror via a proportional-integral (PI) amplifier. In this way the cavity can be locked to the 894 nm stable reference carrier, or any of the sidebands produced by the rf generator. Therefore the cavity length can be locked to within approximately ±500 MHz of any resolvable sideband of any TEM cavity mode of the 894 nm laser, transferring the stability of that laser to the cavity with a choice of ranges of offset from the caesium atomic transition frequency. Figure 3.11 shows the 894 nm light path and electronics for stabilizing the cavity length.

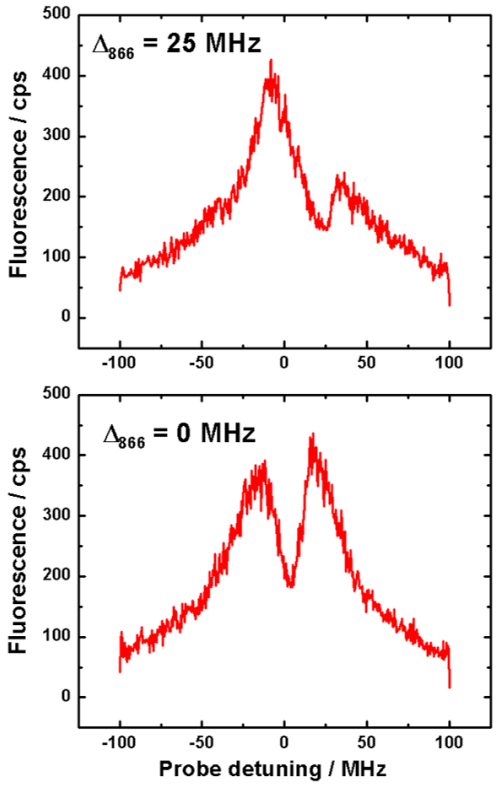

Figure 3.12: Dark resonance spectroscopy. The technique for performing spectroscopy on the dipole-allowed cooling transition was modified to repump the ion with 866 nm light during the probe portion of the sequence. The dip occurs when the repumper has the same detuning from the $P_{1/2}$ level as the cooling laser. Shown are traces taken with the 866 nm laser frequency locked with a detuning Δ_{866} relative to resonance of 25 MHz (top) and on resonance (bottom). The scan range of the 397 nm probe beam is centered on resonance.

Overlapping a mode of the 894 mn with the 866 nm TEM_{00} mode

The amplifier bandwidth limits the range over which the tunable sidebands can be generated, so a free spectral range must be found where a suitable mode of the 894 nm laser is resonant in the cavity within 500 MHz of the 866 nm TEM_{00} mode. Initially it must be established where the 866 nm transition line lies in the experimental cavity free spectral range, beginning with a measurement of the linecentre of the 866 nm transition. To achieve this, dark resonance spectroscopy, treated theoretically in section 2.2.3, was carried out using the allowed dipole transition spectroscopy technique outlined in section 3.4.2. The scheme was modified so that during the probing phase of the sequence, the ion was repumped with 866 nm light. With the 397 nm cooling frequency held constant,

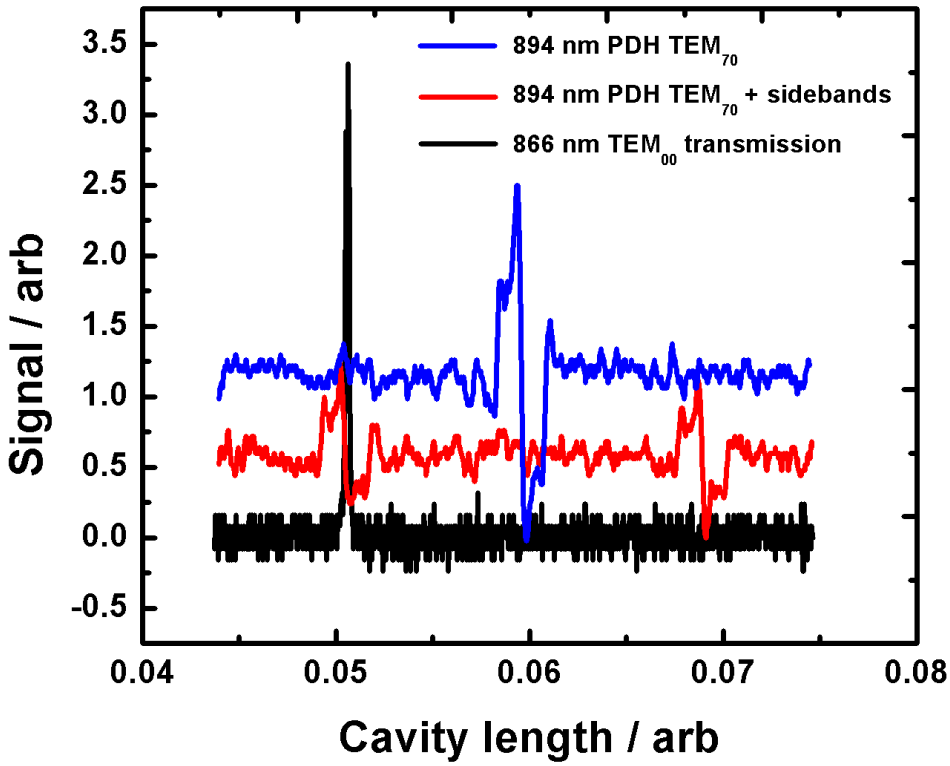

Figure 3.13: Finding an overlap of the 894 mn and 866 nm resonances. While scanning the cavity length the Pound-Drever-Hall error signal generated by the TEM_{70} mode is observed without amplified tunable sidebands (blue) and with ≈100 MHz sidebands (red). The transmitted signal from the TEM_{00} mode of the 866 nm laser shows that in this free spectral range, the stable reference laser can be used to lock the cavity on resonance with the $P_{1/2}$ to $D_{3/2}$ transition.

the detuning of the repumper was changed until a dip characteristic of the population trapping was observed. The dip can be seen in Fig. 3.12 for two different values of the detuning of the 866 nm repumper.

Having established the frequency of the 866 nm transition, the 894 nm light was blocked and the 866 nm laser wavemeter-locked on resonance. 866 nm light was coupled into the cavity from the detection side. For convenience, this was done by coupling the light into the output end of the detection fiber (see Fig. 3.6), after mode-matching the fiber to the cavity, but before coupling it to the single photon counting module (SPCM) which detects cavity emission. See the following section on detecting cavity emission. A flip-mirror was placed in front of the Pound-Drever-Hall APD in order to visualize the 866 nm modes transmitted through the cavity from the detection side on a CCD camera. The cavity

length was scanned with a triangle wave and after locating the 866 nm TEM_{00} mode on the CCD, the resonance was monitored with the APD on an oscilloscope. The black trace in Fig.3.13 shows a peak in cavity transmission when the 866 nm TEM_{00} mode is resonant in the cavity. The 894 nm light was then unblocked so that the cavity length coordinates of the PDH error signals generated from the amplified sidebands of 894 nm light could be compared to that of the 866 nm TEM_{00} mode. The red trace in Fig.3.13 shows the sidebands of the 894 nm stable reference light. In this trace the carrier is vanishingly small because the amplification of the modulation signal generating the sidebands has been optimized for putting power into the first order sidebands. The PDH error signal was used to mark the 894 nm modes as it has a better signal to noise ratio than the bare reflection dip. The oscilloscope trace shows that if the cavity length were locked to the left-hand sideband error signal, the cavity will be resonant with the 866 nm TEM_{00} mode. The error signal due to the 894 nm carrier is shown in blue for reference. The cavity length was scanned over 1 GHz centered on the 866 nm TEM_{00} mode while the coupling of the 894 nm beam into the cavity was changed in order to put power into various parts of the mode spectrum. This was repeated for all the FSRs accessible by the PZT scan range while evaluating all the overlaps for suitability as a locking signal. After evaluating all the traces such as those shown in Fig. 3.13, in which there was an accessible overlap between the 866 nm TEM_{00} and a first order sideband of a mode of the 894 nm reference laser, the 894 nm TEM_{70} mode was chosen. The motivation for choosing this mode was the relatively strong PDH error signal it generated while having a small spatial overlap with the 866 nm TEM_{00} mode. The strong error signal benefits the stability of the PDH lock, while the small spatial overlap between the TEM_{70} and TEM_{00} modes serves to suppress the background signal from the locking light. In addition, the frequency overlap between the modes was in a free spectral range which would allow considerable translation of the locked cavity within the voltage ranges of the PZTs. The accessible translation range is an important factor when translating the cavity mode with respect to the ions in order to position them at antinodes of the cavity field. This is done when characterizing the coupling of many ions to the cavity, detailed in chapter 4.

3.2.3 Detection of cavity emission

As a result of undergoing a cavity-stimulated Raman transition, the ion emits a photon into the cavity mode. The ratio of transmissivities of the mirrors ensures that the photon leaves through a chosen mirror with a high probability. The output from this mirror

is mode-matched to a single-mode fiber which transmits the light directly to an APD single photon counting module (SPCM). Section 3.2.2 details the method used to lock the length of the cavity, and inherent in this scheme is that some 894 nm light used to lock the cavity is transmitted through the cavity, creating an unwanted background. Therefore two dichroic (DC) mirrors are installed in the detection beam path, which transmit 894 nm light while reflecting light at 866 nm. The background due to the locking light is suppressed further by the the use of the TEM_{70} mode of the 894 nm laser, which has only a small spatial mode overlap with the the 866 nm TEM_{00} mode. A further bandpass filter is placed between the fiber output and the SPCM. The SPCM has a dark count of 25 cps and with approximately 8 μW of power at the EOM fiber output, the filtering and mode overlap ensures that less than 75 cps of light from the 894 nm stable locking laser is added to the cavity emission signal from the ions.

The SPCM has an active surface diameter of 70 μm. The mode which is out-coupled from the detection fiber is sufficiently convergent to ensure that the waist of the mode of the cavity signal is less than 70 μm at 60 mm from the fiber, and the SPCM is positioned here.

Before finally coupling the fiber output to the SPCM, 866 nm light was injected into the fiber at the SPCM end, and coupled into the cavity from the detection side. By scanning the cavity length and observing the 866 nm modes on the PDH APD, the detection fiber was mode-matched to the cavity.

3.2.4 Alignment of the trap and cavity axes

The novel purpose of the integrated trap-cavity design is to overlap the line of rf minimum occupied by strings of ions with the centre of the cavity mode, in order to simultaneously couple several ions to the cavity. Overlapping the trap centre with the cavity mode requires a four-stage process, beginning with optimally positioning the cavity mirrors with respect to the geometric trap centre when the mirrors are affixed to the trap mount structure. In the next stage, the cavity mode position is mapped with respect to the trap by locking the cavity to the 866 nm repumper laser and using the light which leaks into the cavity to repump a large ion crystal. The imaging system allows the mode to be mapped in the horizontal plane through fluorescence intensity in the crystal. In the third alignment stage, variable capacitors in each rf electrode circuit are used to change the amplitude of the rf voltage electrode-wise. This allows the rf trap centre to be shifted in the radial plane, to that a single test ion can be moved to the centre of the mode as determined in

the second alignment stage. The second and third alignment stages have only improved the ion-cavity overlap in the horizontal direction. During the final alignment stage, the cavity length and cooling laser are locked in Raman resonance and the ion is continuously cooled. This drives cavity-assisted Raman transitions in the ion with emission into the cavity mode which increases with the degree of radial overlap. Hence the alignment of the ion with the centre of the cavity mode is optimized in orthogonal radial directions by changing the capacitors on electrodes 2 and 3 while maximizing the cavity emission.

Stage 1 alignment - mirrors with respect to geometric trap centre

In the first alignment stage, the position of each mirror is determined by the position of its collet with respect to the trap mount structure. This is radially adjustable due to a clearance between the blank inner diameter of the collet mounting point holes and the mounting screws (see Fig. 3.8). The scheme for optimizing the position of the mirrors relies on the condition that the TEM_{00} cavity mode will be completely overlapped with the trap centre line when the region of each mirror surface through which the trap centre line crosses is perpendicular to the line of the trap centre, i.e. a collimated laser beam propagating along the trap axis will be perfectly retroreflected by a mirror only when the mirror is correctly aligned. The condition is deterministically satisfied through the following method, in which a beam of light is overlapped with the trap centre and the cavity mirrors fixed in place when they maximally retroreflect the beam. The trap mount is fixed firmly to the optical bench with rf and dc electrodes attached. Microscopes are mounted on 3D micrometer translation stages in order to image the edges of the trap electrodes from the side and from above. The coordinates of each edge is measured to the nearest five micrometers, and the position of the line of the rf trap centre calculated. A beam of collimated 866 nm laser light is transmitted through a 50/50 beam splitter and retroreflected with an adjustable plane mirror. In this way a photodiode is aligned to monitor the intensity of the beam which is reflected when it revisits the beam splitter. The plane mirror is removed and the beam coupled into a fiber. At the output of the fiber the beam is re-collimated and aligned to pass through the holes in both dc endcap electrodes. Laser scatter from the tip of a tungsten needle horizontally mounted on a third translation stage is used to probe the alignment of the beam, which is steered until it is overlapped with the rf trap centre as calculated from the positions of the rf electrodes. The collet mount furthest from the source of the laser light is held against the trap mount and translated until the mirror retroreflects the beam, heralded by a signal at the photodiode.

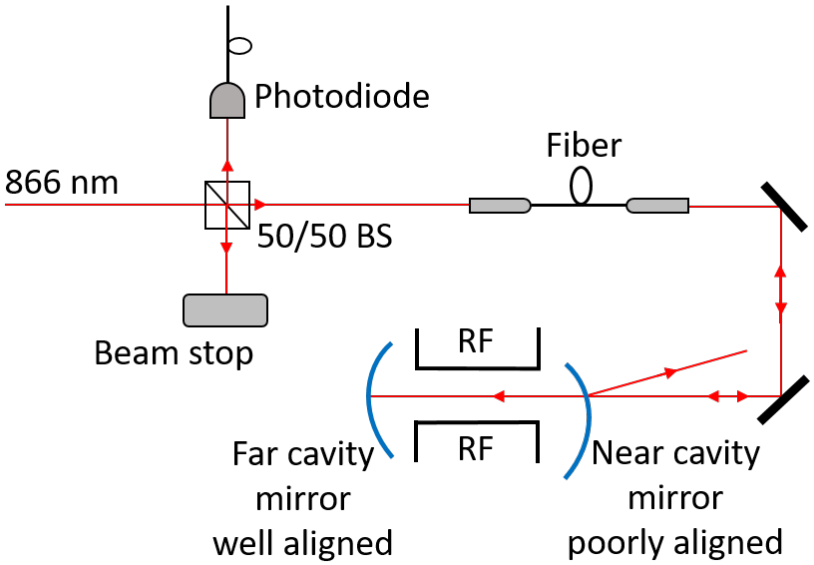

Figure 3.14: Scheme for stage 1 alignment of trap and cavity axes. The 866 nm beam has been overlapped with the trap centre (the line equidistant from all of the blade rf electrode edges). A signal at the photodiode indicates retroreflection by a cavity mirror, and optimal positioning of the mirror is achieved when the photodiode signal is maximized. Shown is when the first mirror (furthest from the beam source) is correctly positioned, but the second mirror is not.

The collet mounting screws are tightened when the signal in the photodiode is maximized. Once fixed in place, the procedure is repeated for the near mirror. Fig. 3.14 shows the geometry of the alignment procedure.

Stage 2 alignment - horizontally imaging cavity mode with cavity-repumped ion crystal

Later, with the trap operational, coarse localization of the centre of the cavity with respect to the trap centre comprises stage two of the alignment process. This is done by locking the cavity to an 866 nm laser which is frequency stabilized to be resonant with the atomic transition, and using it to repump a large crystal of ions. The crystal was moved in the horizontal plane using micromotion compensation dc voltages, so that the cavity mode structure could be identified using ion fluorescence imaged with the CCD camera, shown in Fig. 3.15. The TEM_{20} was chosen for the repumping because saturation of the dark resonance when locking the cavity with the TEM_{00} mode left no resolvable mode structure close to the centre. The pixel coordinates of the cavity axis were recorded.

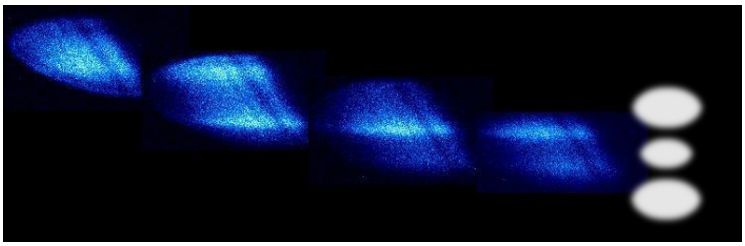

Figure 3.15: Imaging the 866 TEM_{20} cavity mode through repumping. Four stills recorded on the CCD as a large ion crystal is moved in the horizontal plane. The dark resonance of the coupled three-level system was saturated even with the minimum 866 nm beam intensity required to lock the cavity, so that the central dark regions mark the regions of high intensity of the cavity mode, shown schematically to the right of the stills.

Stage 3 alignment - visually locating horizontal rf minimum at mode centre with variable capacitors

In the third alignment stage, a single ion or small ion crystal marks the trap centre, while the variable capacitors in the rf circuit are manipulated to move the trap centre to close to the pixel coordinates previously measured for the centre of the cavity mode in stage 2. During this step it is necessary to regularly adjust the trap drive frequency to maintain rf resonance.

Stage 4 alignment - optimizing overlap radially using cavity emission

In the final stage of the alignment, the radial profile of the mode was mapped by monitoring cavity emission of a single ion while continuously driving the Raman resonance. Changing the capacitors on electrodes 2 and 3 change the position of the ion along the trap x and y directions. Because micromotion affects the level of cavity emission, the micromotion was compensated before each datapoint was taken. Fig. 3.16 shows the cavity emission as a function of the micrometer settings on the capacitors.

3.3 Laser systems

Several lasers are required to trap and cool the ions. Two lasers are used to photoionize the neutral calcium in a two-stage process. Laser Doppler cooling $^{40}Ca^{+}$ requires a minimum of two frequencies of laser light, but a more sophisticated scheme used in these experiments requires three. All the lasers are of the external cavity diode type (ECDL). The cooling laser at 397 nm is frequency-doubled from a 793 nm laser by second harmonic generation. Acousto-optic modulators are used where necessary to rapidly switch intensity and fre-

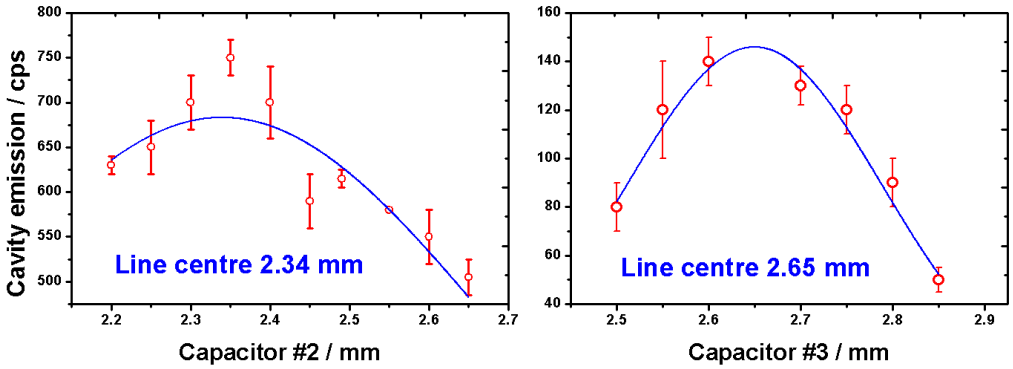

Figure 3.16: Final radial overlap of rf trap centre with the cavity mode. Continuous Raman cavity emission is recorded as variable capacitors in series with electrodes 2 (left) and 3 (right) are adjusted.

quency of the laser beams. Wavemeters with a stability of 10 MHz are used to monitor the laser frequencies, with digital feedback to each laser. However, some laser applications require greater stability, and the lab contains a stable reference laser at 894 nm which is locked to a cavity, which in turn is locked to an electronic transition in caesium, giving the laser stability on both short and long time scales. To transfer the stability of the reference laser to other lasers, a scanning cavity stability transfer lock is employed. The stable laser (master) and lasers to be stabilized (slaves) are coupled into a cavity whose length is constantly scanned. The time instants at which the lasers become resonant in the cavity are monitored and held constant through feedback to the slave lasers.

These lasers and associated systems are now presented in detail.

3.3.1 $^{40}Ca^{+}$ structure and lasers for ion trapping

Photo-ionization lasers

Production of neutral calcium at the trap center is described in section 3.1.1. The center of the trap is crossed by two overlapped laser beams at 423 nm and 375 nm wavelengths. Their purpose is to liberate an electron from the calcium atom in a two-stage photo-ionization process. The first stage, mediated by the 423 nm beam, is resonant and excites an electron in the outer shell from the S_0 ground state to the excited P_1 level. This resonant addressing is isotope-selective ensuring that only $^{40}Ca^{+}$ is trapped. The non-resonant beam at 375 nm then excites the electron out of the atom, completing the ionization

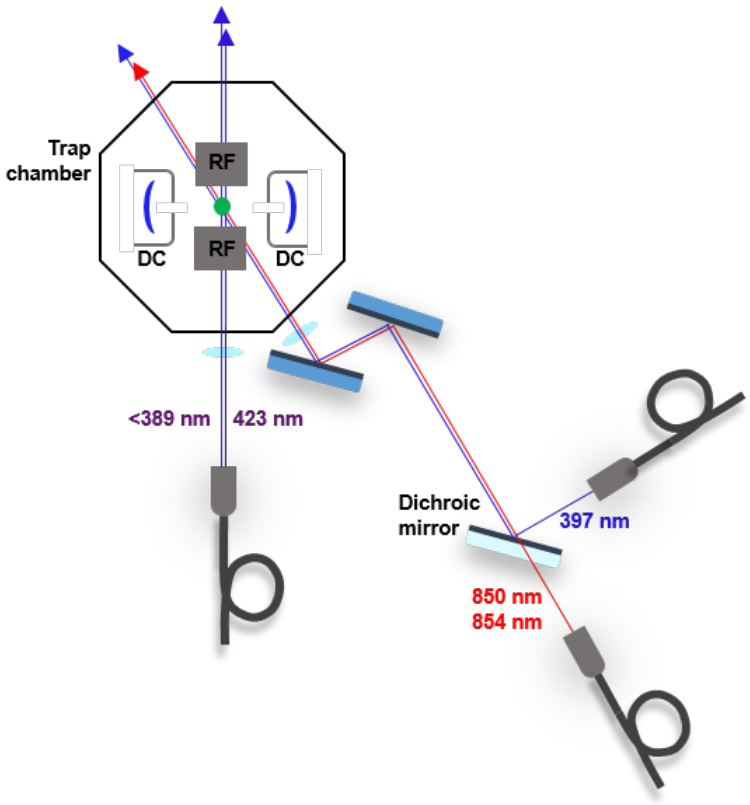

Figure 3.17: Trapping laser beam paths shown with respect to the trap dc and rf electrodes. Neutral calcium is ionized by overlapped beams at wavelengths 423 nm and ¡389 nm. Doppler cooling is carried out by overlapped cooling and repumper beams, beam-walked together to minimize scatter from the electrodes.

process. Figure 3.17 shows schematically how the photo-ionization,cooling and repump lasers are aligned into the trap. The photo-ionization lasers are previously overlapped into the same single mode fiber, from which the collimated beams are directed through a 100 mm plano-convex lens positioned with the trap centre at its focus. Effort has been made to strike the lens in the centre to minimize the difference in refraction angles which the bi-chromatic beam experiences. The waists of the beam are sufficiently close for efficient ionization to take place with the available power.

Cooling and repumper lasers

The lowest-lying energy states of $^{40}Ca^{+}$ are shown in Fig. 3.18 with transition wavelengths and decay rates. The decay rates are the inverse of the lifetimes in the absence of other transitions. The ion experiences the trapping pseudopotential derived in section 2.1, and occupies high motional energy states in the radial and axial harmonic potentials. In order to further localize the ion it must be laser Doppler cooled. This is treated theoretically

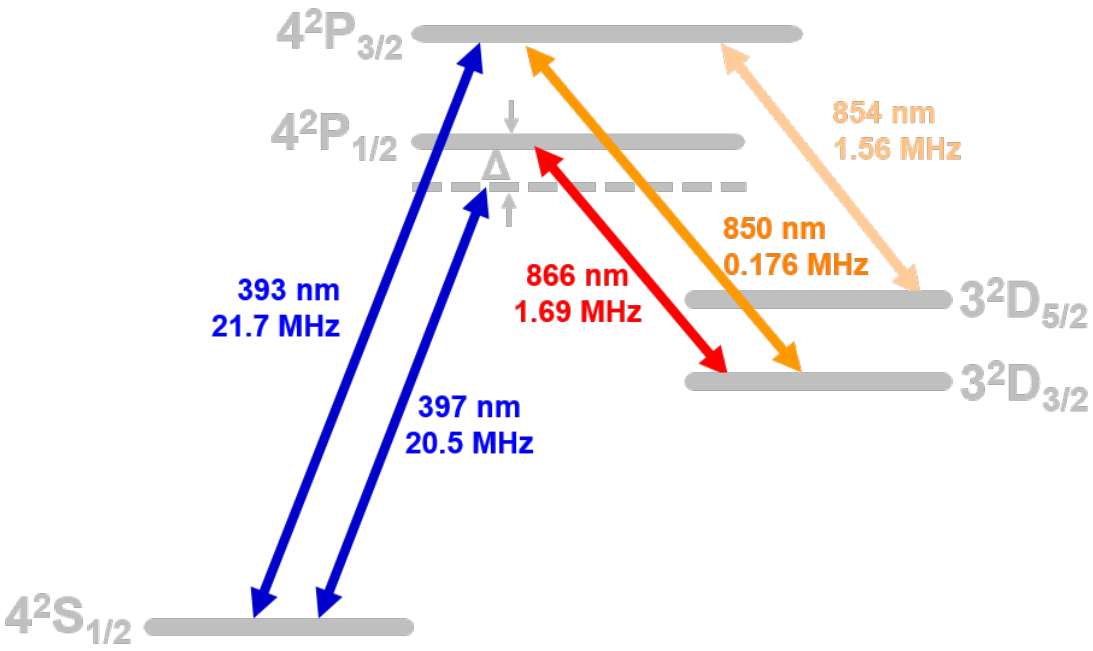

Figure 3.18: Lowest 5 energy levels in $^{40}Ca^{+}$. The wavelengths and decay rates of the transitions between the levels are shown, as well as the detuning from resonance Δ of the 397 nm cooling laser.

in section 2.2.2. Cooling is achieved through scattering photons on the fast $S_{1/2}$ to $P_{1/2}$ transition, and there is an 8% decay channel to the dark $D_{3/2}$ level, requiring the application of a repumper laser to repopulate the excited state. An 866 nm laser can be used for this (and sometimes is - see, for example, the dark resonance spectroscopy presented in section 3.2.2) although in our system repumping is generally done with a pair of lasers at 850 nm and 854 nm. The 850 nm beam evacuates the $D_{3/2}$ level to the $P_{3/2}$ level and the 854 nm beam clears out population which in the $D_{5/2}$ level after decaying there from the $P_{3/2}$ level. The purpose of this indirect repumping scheme is to avoid the coherent population trapping resulting from cooling on a closed three-level system, derived in section 2.2.3, and to avoid broadening the $P_{1/2}$ level with the 866 nm repump laser. The $D_{3/2}$ and $D_{5/2}$ levels are meta-stable with a lifetime of one second. In this thesis, *optimal cooling* refers to cooling while repumping with the 850 and 854 nm lasers, in contrast to repumping with 866 nm light.

The 850 nm and 854 nm repumper beams are overlapped in the same fiber, and this bichromatic beam is further overlapped with 397 nm cooling light at a dichroic mirror shown in Fig. 3.17. The three overlapped beams are reflected twice from adjustable mirrors to allow the minimization of scatter through control of the beam alignment. The

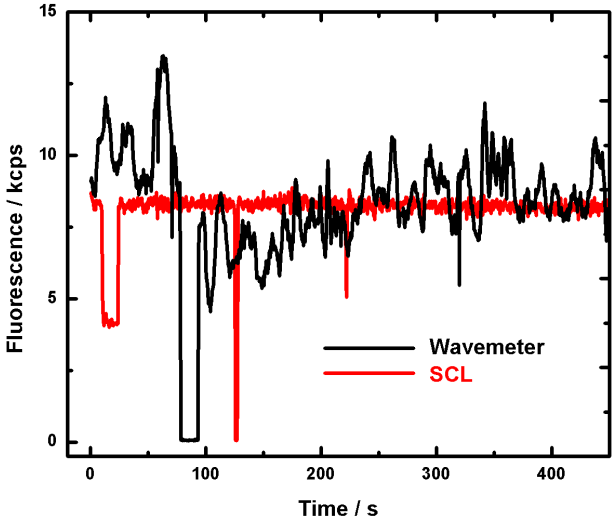

Figure 3.19: Fluorecsence stability comparison. Fluorescence recorded with PMT for 397 nm cooling laser locked to the wavemeter and the scanning cavity lock. The sudden drops in signal are due to collisions between the ions and residual gas molecules in the vacuum system - see end of subsection "Cooling and repumper lasers".

tri-chromatic beam is focussed at the trap centre by a 100 mm plano-convex lens. When using the 397 nm cooling laser to drive cavity-assisted Raman transitions, the cooling laser and cavity length must both be locked to the same reference in order to stably meet the condition for Raman resonance stated in section 2.3. The experimental cavity length is Pound-Drever-Hall locked directly to the stable Cs reference laser, and although the 397 nm cooling beam is UV, it is frequency-doubled from an IR diode, so the cooling laser can be locked to the reference laser via the scanning cavity lock described in 3.3.3. It is also necessary to lock the cooling laser to the stable reference laser in order to cool the ion close to the Doppler limit for reasons outlined in section 2.2.2, as the wavemeter is only stable to 60 MHz while the natural line width of the cooling transition is 22.4 MHz. When using the ion fluorescence to characterize some part of the ion trap-cavity system it is advantageous to have the cooling laser well frequency-stabilized. Figure 3.19 shows the difference in stability of the PMT-recorded fluorescence while cooling with the pre-doubled 794 nm laser diode locked to the wavemeter and to the scanning cavity lock. The sharp drops in signal herald a collision between the ion and a molecule from the residual gas background of the vacuum system. When this happens, the detuning of the Doppler cooling laser relative to the ion is suddenly shifted by an amount sufficient to cause temporary delocalization of the ion and a drop in fluorescence.

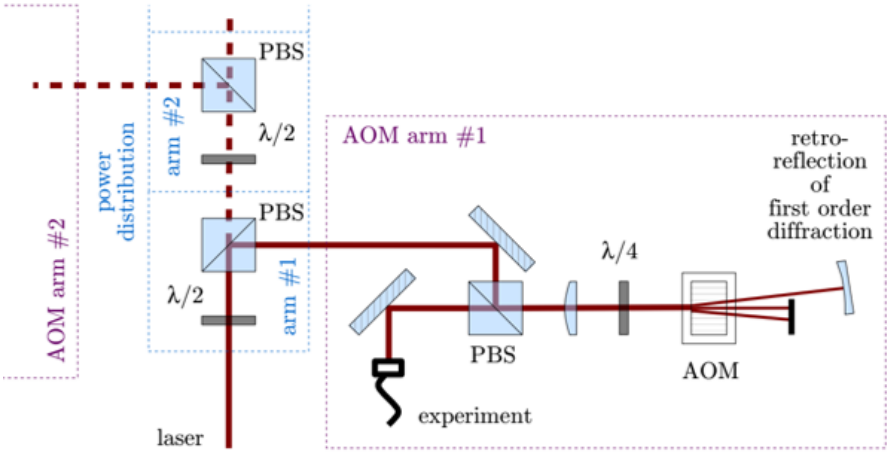

Figure 3.20: A double pass AOM setup. Light is picked off from the main laser path with a half wave plate in front of a polarizing beam splitter (PBS). After entering the setup through a second PBS the first order diffraction beam is retroreflected back through the AOM and after passing twice through the quarter wave plate, exits the setup via the PBS toward the experiment. Drawing by Nic Seymour Smith taken from [25].

Acousto-optical modulators as switches and frequency shifters

All of the laser beams in these experiments are passed once or twice through an acousto-optic modulator (AOM). These are devices which rapidly switch on or off the laser beam, and allow small changes in frequency to be applied to the beam. The AOM contains a crystal which is acoustically driven by an rf actuator. If a laser beam passes through the crystal in a direction perpendicular to the travelling acoustic pressure wave, it is Bragg diffracted. The first order diffracted optical beam is shifted up by the frequency of the acoustic wave. The amount of power in the diffracted beams is a function of the amplitude of the acoustic wave. If the power to the actuator is cut, the first order beam vanishes. If it has been coupled into a fiber, the transmission in the fiber is attenuated by approximately 40 dB for the angle produced by a 200 MHz acoustic frequency. In this way, the AOM behaves as an optical switch to a beam of laser light with a rise time of less than 100 ns and delay of around 500 ns. The rise time is a function of the beam waist inside the AOM. By changing the rf driving frequency, the optical frequency of the light can be given an offset by the same amount. If fiber-coupled, the coupling changes with frequency as the Bragg angle changes, and this is compensated by retro-reflecting the first order beam back through the AOM and once again selecting the first order in the second-pass beams. To a first approximation, this cancels the change in angle due to the change in frequency. Figure 3.20 shows the geometry of a double pass AOM setup, as well as the scheme for

distributing the power from one laser source.

Generally a diode laser in the lab will be shared between several experiments. Therefore a series of PBSs are placed in the path of the output from the laser, with a half wave plate in front of each to precisely and easily define how much power is sent to each experiment. The double-pass AOM configurations are located after the experimental beams are picked off. The inclusion of a PBS and quarter wave plate in the double pass beam path rotates the linear polarization of the beam to the orthogonal basis so that the beam leaves the double-pass setup at the PBS and can be steered toward the experiment. The AOMs have a bandwidth of ± 50 MHz either side of the default 200 MHz oscillation frequency.

The AOMs are driven by a voltage-controlled oscillator (VCO) containing an rf oscillator and an amplifier. Each is controlled by a dc voltage, making possible the direct manipulation of the frequency and power in a laser beam by a pair of computer-controlled DAQ output voltages. In practice, the dc voltages produced in this way are slow compared with atomic timescales. In order to maximize experimental repetition rates, the fast switching of laser beams as part of an experimental pulse sequence is possible if an rf switch is included between the VCO and the AOM, with the switch position governed by a pulse generator. This enables the fast switching of rf power to the AOM, either alternating between two VCO sources (with independent powers and frequencies) or to quickly switch a laser between on and off states. Section 3.4.2 details an application for rf switching of the cooling beam when performing spectroscopy on the 397 nm cooling transition.

3.3.2 Atomic frequency reference at 894 nm

The laboratory lasers may be locked to commercial wavemeters with resolutions of 60 MHz or 10 MHz depending on model, which are calibrated with commercial reference lasers. The feedback is generated by digitally calculated proportional and integral gain, applied through the voltage output of the DAQ of the PC which is hosting the wavemeter software. The experiments in this thesis set some stability requirements beyond these locking line widths. The experimental cavity is locked by the Pound-Drever-Hall technique to a laser which must be below the 470 kHz linewidth of the cavity, as must be the linewidth of the laser which drives the cavity-assisted Raman transitions. Additionally, both experiments require the ion to be cooled close to the Doppler limit which requires the cooling transition to be as close to the natural linewidth as possible, placing stringent requirements on the stability of the 397 nm cooling laser.

To achieve the required stability, an atomic frequency-stable reference laser is used

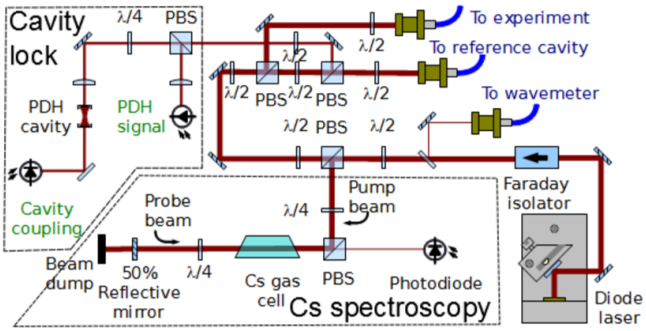

Figure 3.21: Optical path of the 894 nm laser. The beam is split between the cavity and the caesium spectroscopy cell, with branches to the experimental cavity, the reference cavity of the scanning cavity lock setup and the wavemeter. Drawing by Nic Seymour Smith taken from [25].

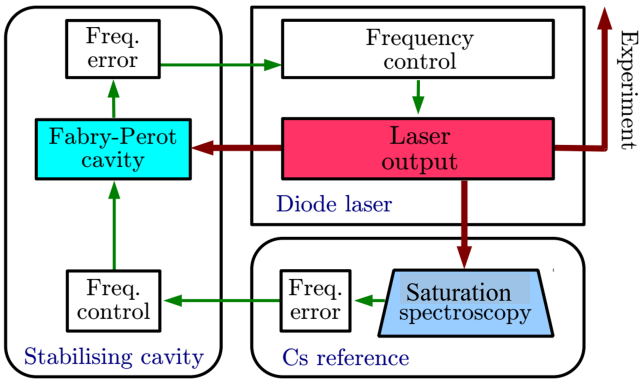

Figure 3.22: Feedback logic in the Cs reference. The laser is locked to the Fabry-Perot cavity, which is locked to the atomic spectroscopy signal. Drawing by Nic Seymour Smith taken from [25].

which was built by Peter Blythe and Nic Seymour-Smith [25] during his doctoral research, and later improved by Ezra Kassa, in which a laser is stabilized on short and long timescales by locking it to a Fabry-Perot cavity which is in turn locked to an atomic transition in caesium. It consists of an external cavity diode laser (ECDL) laser near 894 nm which is coupled to a stabilizing Fabry-Perot cavity, from which a PDH error signal is generated. The error signal is fed back to the laser via independent PI circuits to both the laser current and the external cavity grating angle. Some of the beam is picked off before it reaches the cavity, and passed through a saturation spectroscopy setup centered around a caesium gas cell. A PDH error signal is derived from a dip in one of the 894 nm D1 transitions. Once the laser is locked to the cavity, the second PDH derived from the spectroscopy is fed back to a PZT on one of the cavity mirrors, holding the cavity length

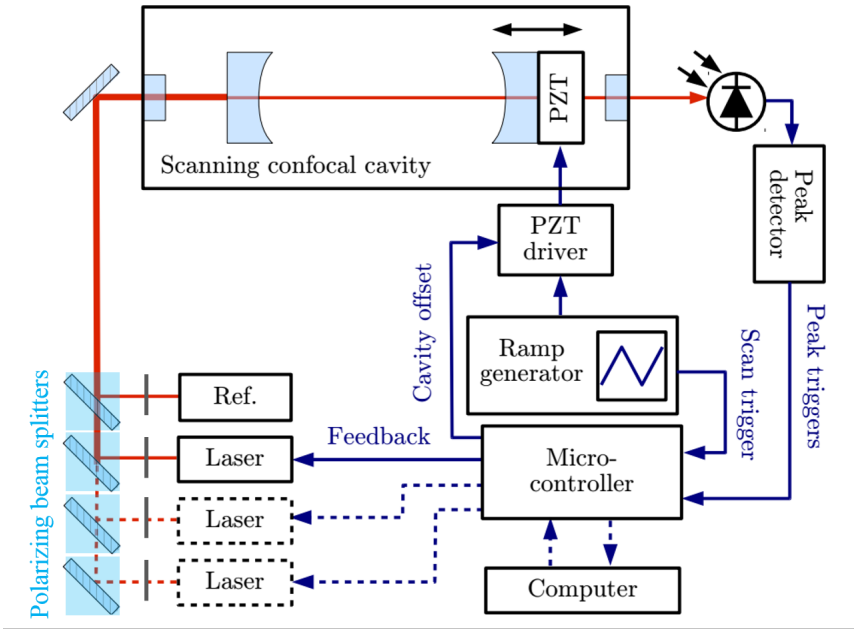

Figure 3.23: Optical paths of the 894 nm master and IR slave lasers. The beams are overlapped and coupled into the cavity as the length is scanned. A peak detector resolves the transmission peaks and passes the signals to a microcontroller which calculates arrival times for each peak with respect to the master and then generates feedback to keep these times constant. Drawing by Nic Seymour Smith taken from [25].

resonant with the optical atomic transition. The optical path of the laser is shown in Fig. 3.21 and a diagram of the feedback loops is shown in Fig. 3.22.

The measured quality of the locks are 40 kHz each, well within the stability requirements of both the experimental cavity length lock and the cooling and Raman lasers. This stability is transferred to other lasers via the scanning cavity lock, detailed in the next section.

3.3.3 Scanning cavity stability transfer lock

The purpose of the scanning cavity lock (SCL) is to transfer the stability of the caesium reference laser at 894 nm ('master' laser) to other lasers in the lab ('slave' lasers). This is achieved by coupling the master and slave lasers into a cavity from one side and monitoring the transmission through the cavity with a fast photodiode. When laser light of a given wavelength impinges on a highly reflective cavity, the light is largely reflected unless the condition for resonance is met. This condition is that the cavity length is equal to an integer number of half wavelengths of the light, allowing the build-up of a standing wave field in the cavity and transmission of the light through the cavity. With the master

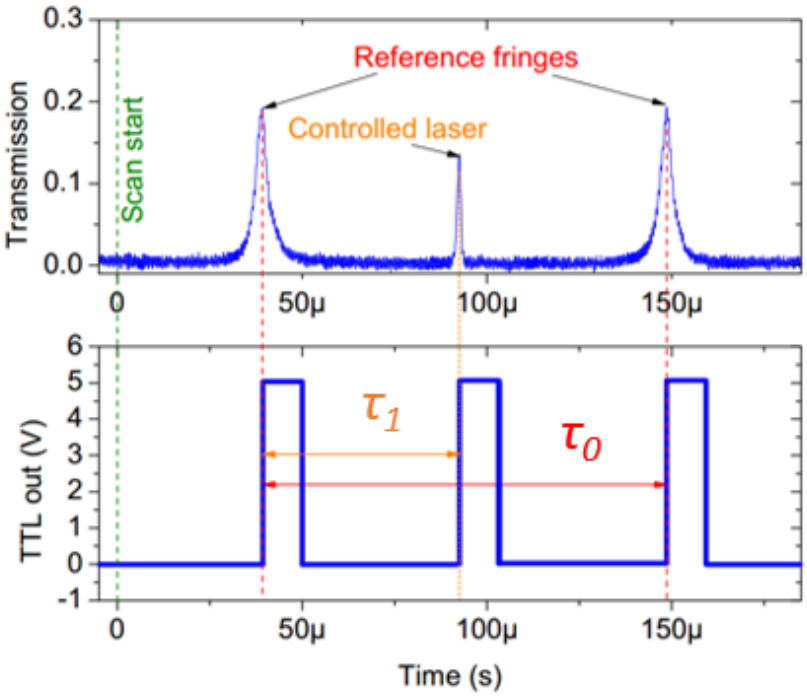

Figure 3.24: Cavity transmission (top) and response of the peak detector (bottom) for one slave laser. The time τ_0 and the ratio τ_1/τ_0 are held constant by feeding back to the cavity length and slave laser respectively. Drawing by Nic Seymour Smith taken from [25].

and slave laser beams coupled, the cavity length is scanned back and forth over one free spectral range using a piezo-electric transducer on one of the mirrors. The cavity meets the condition for resonance at different lengths for different wavelengths, so that the instances in time when transmission is detected by the photodiode during the scan are a function of the laser frequencies. The photodiode voltage is monitored by a microprocessor which distinguishes the frequencies by their time-ordering with respect to the start of each scan. The microprocessor calculates feedback individually for the slave lasers to hold them at a constant frequency offset from the master laser. The cavity is coated for high reflectivity for infra red wavelengths, so only lasers in this wavelength band can be stabilized in this way. In the experiments in this thesis, the only non-infra red laser to benefit from the SCL is the the 397 nm cooling laser. This is frequency-doubled from a 793 nm diode laser which is stabilized by the SCL. The SCL was built by Peter Blythe and Nic Seymour-Smith [25].

Figure 3.23 shows schematically how the master 894 nm beam is overlapped using polarizing beam splitters and half wave plates with several other slave beams and coupled into a cavity, which is coated for high reflectivity in the IR spectrum. The cavity is confocal ($L = 250\text{mm} \rightarrow 1\text{FSR} = 300$ MHz) ensuring all the modes are degenerate in frequency

for a given laser, so that changes in coupling do not change the shape of the front of the peak and generate an offset. The cavity length is scanned and the transmission monitored on a 10 MHz bandwidth photodiode. Peaks in transmitted light are recognized by a peak detector circuit which acts as a discriminator and pulse shaper, and this generates a TTL pulse for each peak detected. This is shown in Fig. 3.24. These pulses are fed into a microcontroller which timestamps the resonance events. The amplitude of the ramp generator signal is set to include resonance peaks from neighbouring free spectral ranges of the reference laser, and the offset is tuned so that resonance peaks attributed to the slave laser(s) appear between the two reference peaks. A computer interface allows the user to input the identity of the slave laser, the order in which their peaks appear, and the appropriate proportional-integral feedback values. The trigger from the function generator which provides the voltage for the cavity scan is a start signal and the microcontroller tracks the peaks as they are detected by the discriminator until it reaches the last peak due to the reference laser. The controller feeds back to a PZT on one of the cavity mirrors to hold constant the time τ_0 measured between the first and last master reference peaks. It calculates feedback voltages according to the proportional and integral gains set by the user for each slave laser, required to hold constant the ratios $\tau_i/\tau_0\,(i = 1, 2, 3)$ for three slave lasers, limited by the number of analogue voltage outputs on the controller.

Trapping $^{40}Ca^{+}$ does not require the stability of the SCL per se, as all the relevant transition linewidths can be power broadened to greater full widths at half maximum than the 60 MHz or 10MHz resolution of the two types of commercial wavemeter in the lab. However, when cooling close to the Doppler limit, the intensity of the cooling laser is reduced to narrow the line to close to its radiative linewidth of 22.4 MHz. Assuming the line is Lorentzian in shape, a drift of 10 MHz would dramatically change the cooling dynamics, requiring that this laser is locked to the SCL. In the experiments described in chapter 5, a laser at 866 nm is required to drive vacuum Rabi oscillations, and on the timescale of the oscillations, a laser linewidth greater than the cavity linewidth causes a rapid dephasing of the experimental signal. Therefore this laser, too, is locked to the SCL.

3.4 Routine characterization and optimization

Ion trap CQED requires the characterization, optimization or compensation of several important parameters, and the most important in our setup are now discussed. In order to stabilize the cavity length to fulfil the condition for Raman resonance (see section 2.3), Raman spectroscopy is routinely carried out in order to extract the line centre of the

Raman transition. Spectroscopy is also carried out on the 397 nm cooling transition to diagnose heating effects in the ion, and to establish the line centre and line width for cooling close to the Doppler limit. Micromotion is a feature of rf ion trapping, and regular compensation of stray electric fields is carried out. Both of the experiments in this thesis are sensitive to the magnetic field at the trap centre, and a scheme for the detection, compensation and generation of the magnetic field is required. Finally, the trap secular frequencies in the radial and axial directions characterize the confinement in the trap, and the axial secular frequency is a key parameter in the experiment described in chapter 4.

3.4.1 Raman spectroscopy

Section 2.3 introduces the use of cavity-assisted Raman transitions in the work in this thesis. To observe the Raman resonance the cavity length is scanned while driving the transition with a laser. In the experiments described in chapter 4, the laser which performs Doppler cooling on the 397 nm transition serves simultaneously as the drive laser for a cavity-assisted Raman transition, and it is by holding the cavity length in Raman resonance with the cooling laser and cooling continuously that the visibility scans in those experiments are performed. In section 5.1, the ion is prepared in a $D_{3/2}$ Zeeman sublevel after which an 866 nm pulse serves as the drive laser for one branch of a polarized Raman transition within the D manifold, while the cavity length is locked resonant with the other branch. Unlike the continuous emission in the first example, the latter produces a single polarized photon per pulse [4], followed by the need for cooling and state initialization.

In practice, the cavity length is PDH-stabilized to the first order tunable sideband of the TEM_{70} mode of the 894 nm stable reference laser, as outlined in section 3.2.2. The rf generator is computer-controlled in order to carry out the Raman spectroscopy scans. With the cavity locked to the 894 nm mode the frequency of the rf signal is changed, step-wise and typically by 1 MHz, and the cavity length follows. The sideband which has an accessible overlap with the 866 nm TEM_{00} mode is of higher frequency than the carrier, so an increase in the rf signal causes the cavity length to shorten as it remains locked on resonance. When the rf frequency is changed, the power in the sidebands changes. For the cavity lock to operate optimally, it is necessary to maximize the slope of the PDH error signal, so a pre-calibrated look-up table is used by the software to apply the optimum rf power at each frequency step.

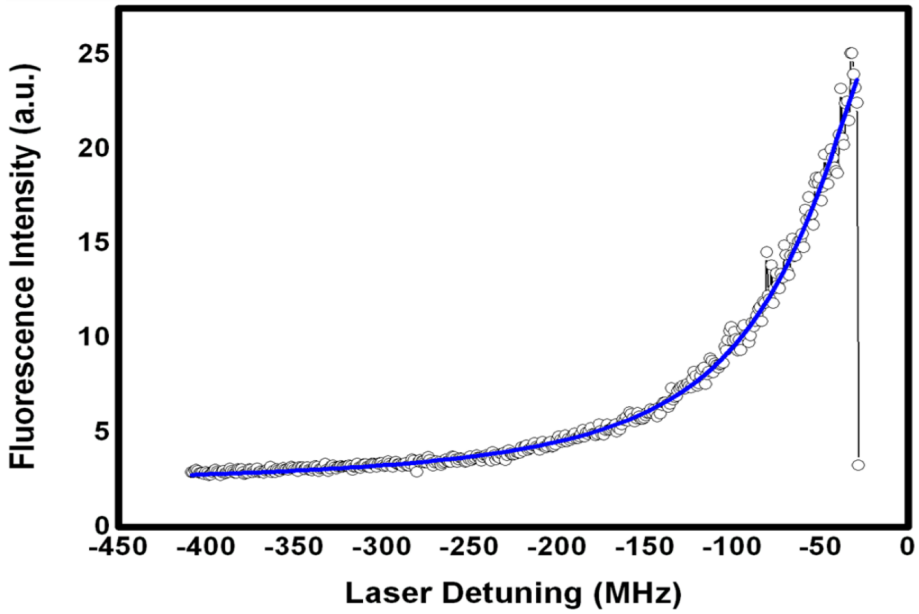

Figure 3.25: Fluorescence spectrum of allowed dipole transition. The cooling laser frequency is scanned toward line centre from far red detuned. The drop in fluorescence close to centre is due to Doppler heating. Data taken by Kevin Sheridan and image taken from [42].

3.4.2 Precision spectroscopy on the dipole-allowed cooling transition

In order to cool the ion close to the Doppler cooling limit, it is necessary to have precise information about the detuning of the cooling laser and the line shape of the transition. As derived in section 2.2.2, the detuning should be $-\Gamma/2$ and the line width is to be reduced as closely as possible to the natural line width. The relative Lorentzian and Gaussian contributions to the lineshape give information about possible sources of heating of the ion. Performing spectroscopy on the 397 nm cooling transition is not straight-forward, however, as the detuning of the cooling laser has a direct effect the cooling dynamics, resulting in distortion of the line shape, and probing the blue side of the transition directly heats the ion. Figure 3.25 shows the fluorescence spectrum measured when the frequency of the 397 nm laser is scanned towards the line centre from a far red detuning. The sudden drop in fluorescence close to line centre is due to Doppler heating of the ion (the opposite effect to Doppler cooling arising from a blue-detuned laser addressing the cooling transition). A technique to routinely carry out precision spectroscopy on the dipole-allowed transition has been developed [44] which overcomes these problems by decoupling the cooling and probing roles of the 397 nm laser.

The scheme employs an AOM driven by two switched VCOs to alternately cool and

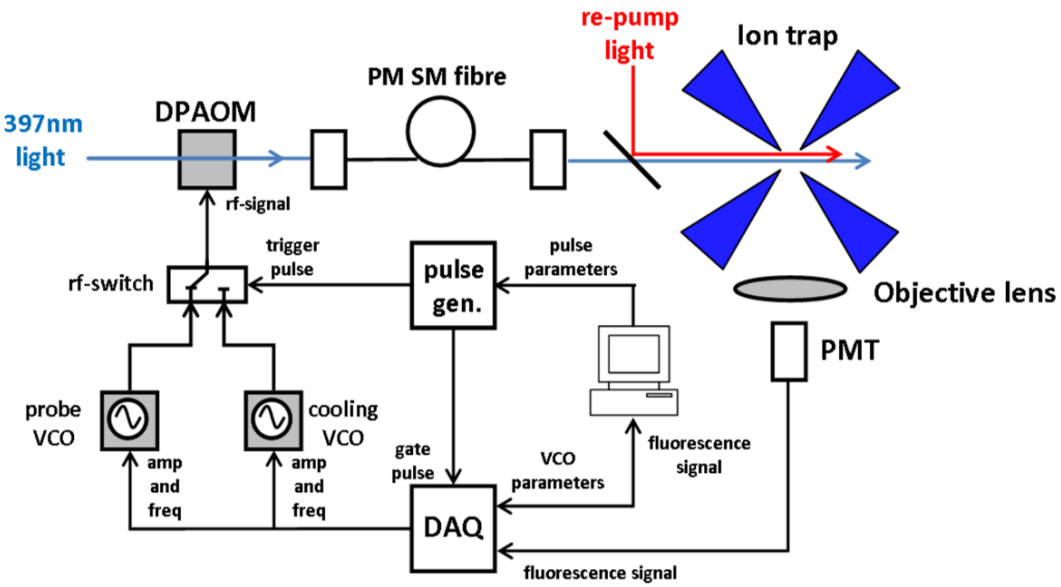

Figure 3.26: Setup for probing the 397 nm transition. A double pass AOM (DPAOM) switches the 397 nm laser between cooling and probing modes. A computer steps the frequency of the probe light while keeping the optical power constant with data from a calibration file. Image by Kevin Sheridan and taken from [42].

probe the ion, while the PMT count is gated off for the cooling period. This enables a DAQ to record the fluorescence rate at each frequency step due only to the frequency of the probe beam. The pulse sequence timing is chosen so that the rise in temperature which occurs during the probing phase is offset by the cooling period, preventing a build up in heating of the ion over the course of a scan.

Figure 3.26 shows the dipole-allowed spectroscopy setup. An rf switch alternates the supply of rf power to an AOM between two VCOs. One supplies rf at a constant frequency and amplitude to cool the ion stably, while the other changes frequency in steps in order to probe the fluorescence over the measurement range. The rf switch passes a VCO signal which depends on whether a TTL trigger pulse is high or low at an input. Therefore a pulse generator sets the repetition rate and duty cycle of the cooling and probing pulses. Computer control of the probe VCO enables each change in frequency to be accompanied by a pre-calibrated change in rf amplitude to compensate the effects of the system bandwidth and changes in coupling on the optical power.

A pulse sequence of 15 μs cooling to 5 μs probing is used, and an integration time of between 0.5 s and 2 s per frequency step, depending on the quality of the fit required. In our system the line shape was consistently found to have a negligible Gaussian component

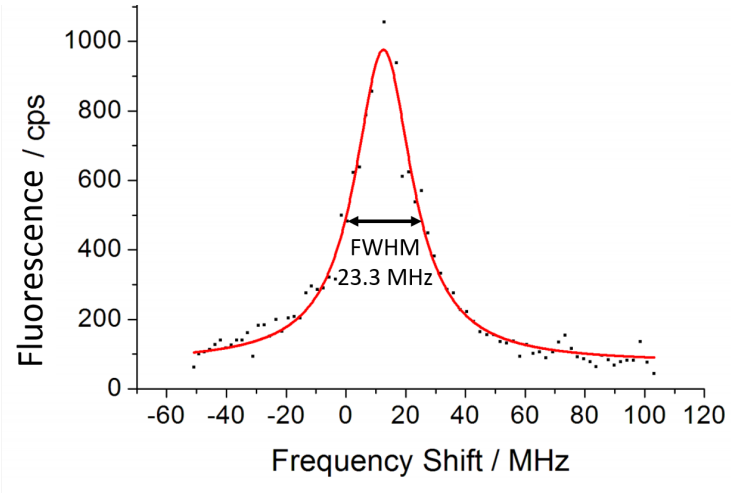

Figure 3.27: Precision spectroscopy on the dipole-allowed 397 nm cooling transition. For each datapoint the gated measurement accumulates fluorescence statistics during the probe portion of the sequence. The frequency shift is the probe laser's detuning from the frequency of the cooling laser. The fitted line has a width close to the natural linewidth.

to the width, so the 397 nm spectroscopy was primarily used to check the line width and laser detuning when cooling close to the Doppler cooling limit. An example of the line shape extracted via this technique is shown in Fig. 3.27.

3.4.3 Micromotion compensation

Micromotion is a driven motion of the trapped ions at the radio frequency of the trap drive, derived in section 2.1. While intrinsic micromotion is an artifact of the rf trapping physics, extrinsic micromotion results from the displacement of an ion from the rf trap centre by a stray dc field. This results in an oscillatory motion proportional and perpendicular to the displacement from the geometric rf minimum and can be detected and compensated.

To compensate the micromotion a dc voltage is applied to each radial rf electrode, in order to compensate the perturbing dc field. If the trap confinement is made shallow in the radial direction through a reduction in the amplitude of the rf trapping voltage, the force felt by the ion due to stray dc fields will push it further from the trap centre. By opening and closing the trap in this way, coarse micromotion compensation can be achieved using the CCD camera. Although a computer could fit a Gaussian function to the CCD image, giving near-arbitrary resolution in the plane perpendicular to the line of sight of the imaging system, the technique clearly offers a much reduced resolution when the ion is displaced parallel to the direction of view of the imaging system. Therefore another technique has been developed, in which photon arrival times are frequency correlated with

the trap drive electronics.

If the ion has an oscillatory motion with a component parallel to a cooling beam, the rate at which photons are scattered will be modulated, due to the Doppler effect, at the trap drive frequency. A time-to-digital converter is used with start signals given by a photon arrival event at the PMT and stop signals from the trigger pulse of the trap drive function generator, four-times frequency divided. The resulting correlation contains four oscillations in the height of the binned photon arrival times, to which a sinusoidal function is fitted, and the amplitude of the fit is extracted. This scheme is presented in detail in Stephen Begley's thesis [51]. For some change in the dc electric field, the ion can be moved through a point where its micromotion component in the direction of the laser vanishes, as the amplitude in the correlation goes to zero. Further movement in this direction results in a change in sign of the amplitude. For the purpose of micromotion compensation the radial trap plane is decomposed into orthogonal horizontal and vertical axes, H and V (corresponding to the natural trap axes x' and y', defined in Fig.2.1). A micromotion-compensating dc field is applied in these directions with dc voltages U_1, U_2, U_3 and U_4 on electrodes 1, 2, 3 and 4 respectively.

$$H = (U_1 + U_2) - (U_3 + U_4) \tag{3.3}$$

and

$$V = (U_1 + U_4) - (U_2 + U_3). \tag{3.4}$$

The field in the H direction is held constant while the photon correlation measurement is used to determine for what field in V the micromotion in the direction of the cooling laser is minimized. The parameter space for that laser is mapped by repeating this for many values in H. The result is a line in H - V space on which the micromotion is minimized for that laser. The process is then repeated for a second laser, aligned so as to maximize the angle between it and the other laser. In this way a crossing point is found at which the applied electric field has moved the ion to a global micromotion minimum in the radial plane of the trap. A crossing point is shown in Fig. 3.28.

3.4.4 Magnetic field coils and field compensation

All the energy levels of $^{40}Ca^{+}$ which we access have magnetic sublevels whose degeneracy is lifted by the presence of a magnetic field. The experiments in chapter 4 require a strong Raman transition to produce cavity emission proportional to the degree of coupling between ion and cavity. This is best achieved by having all the Zeeman levels degenerate and driving the $S_{1/2}$ to $D_{3/2}$ transition. In the experiments in chapter 5, a Raman

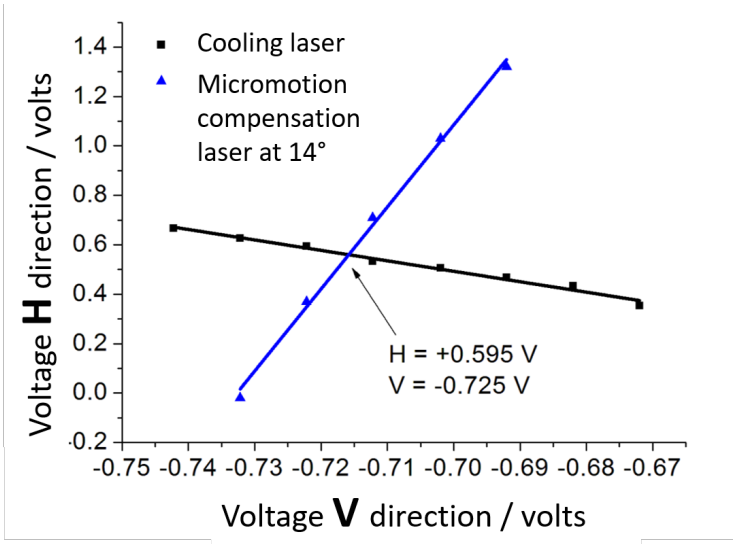

Figure 3.28: Micromotion compensation plot. The horizontal (H) and vertical (V) components of the micromotion compensation voltages are manipulated through dc voltages applied to the rf electrodes as defined in Eqs.3.3 and 3.4. Lines of minimum micromotion are found for the cooling laser (black) and a separate micromotion compensation laser (blue) elevated to 14°. The lines cross when the H and V dc electric field components place the ion at the trap rf minimum.

transition couples the $|D_{3/2}, m = -3/2\rangle$ and $|D_{3/2}, m = 1/2\rangle$ states. In order to resolve this transition, the degeneracy of the Zeeman substructure is lifted by application of a magnetic field to the point where individual lines are resolved.

To control the ions' magnetic environment, field coils (shown in Fig. 3.29) are mounted on an aluminium frame around the trap chamber in order to produce a magnetic field in an arbitrary direction at the centre of the trap. Before being mounted on the trap chamber, the fields generated by each coil as a function of current were measured using a Hall probe magnetometer. The probe was placed at the centre of the frame, and rotated to maximize the flux for successive coil pair measurements before varying the current and recording the field produced. The results are shown in Fig.3.30.

With the calibrated coils in place, before generating the desired magnetic environment at the trap centre, the ambient field was detected and compensated using a scheme based on the ground state Hanle effect [52], which is now described. While cooling and repumping with 866 nm light, all the transitions with respect to a given quantization axis between the magnetic sublevels in the $P_{1/2}$ and $D_{3/2}$ states are shown in Fig. 3.31. There is a dark

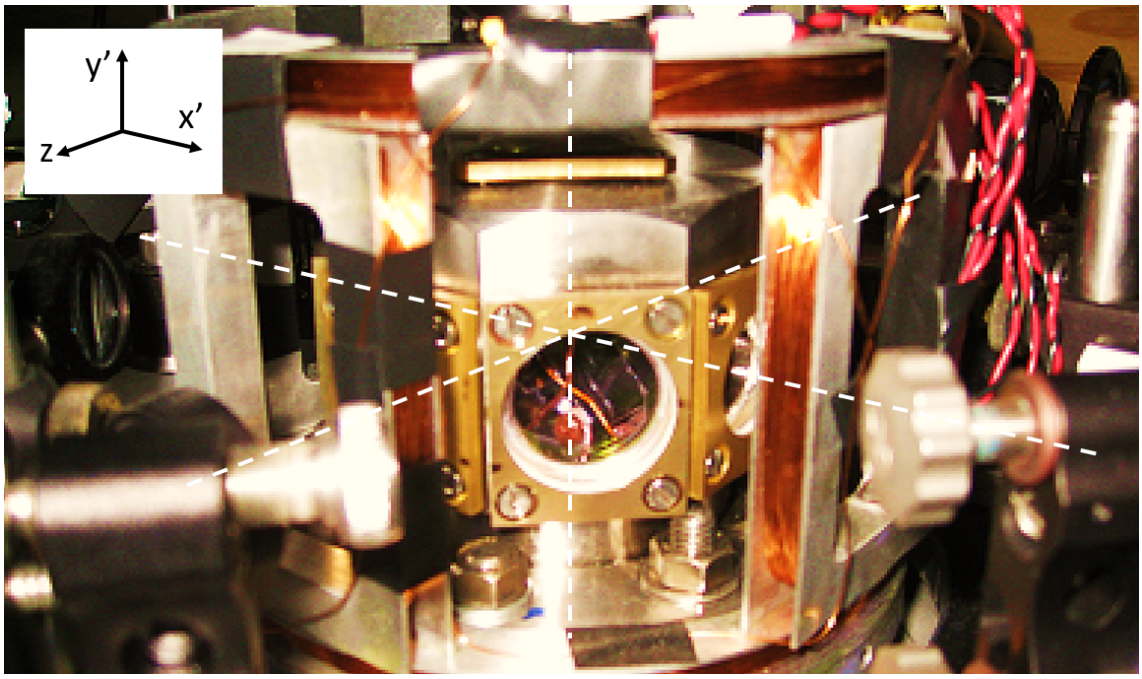

Figure 3.29: 3D magnetic field coils. A three-channel current supply produces a magnetic field with components along the natural axes of the trap, x', y' and z (defined in Theory chapter section 2.1).

state which is a superposition of those $D_{3/2}$ states uncoupled by the repumper, formally

$$\left(\sum_{m=-1/2}^{1/2} \sum_{m'=-3/2}^{3/2} \hbar\Omega_{m,m'} \left|P_{1/2}, m\right\rangle\left\langle D_{3/2}, m'\right| \right) |\Psi\rangle = 0. \tag{1}$$

If the repumper has polarization components with respect to the quantization axis which only excite σ^+ transitions, Fig. 3.31 indicates that the $\left|D_{3/2}, m = +1/2\right\rangle$ and $\left|D_{3/2}, m = +3/2\right\rangle$ will be uncoupled dark states. Likewise, when the repumper is polarized so that it only drives σ^- transitions, the $\left|D_{3/2}, m = -1/2\right\rangle$ and $\left|D_{3/2}, m = -3/2\right\rangle$ are the dark states. The dark states are $\left|D_{3/2}, m = \pm 3/2\right\rangle$ when only π transitions are driven.

Because in general laser light contains a superposition of polarization components which simultaneously drive the σ^+, σ^- and π transitions, the dark state for an arbitrary polarization will be a superposition of the corresponding $D_{3/2}$ sublevels which are not repumped by those polarizations. In the absence of a magnetic field, the states are degenerate in energy, and there is only a time evolution of the global phase. Once the population reaches a dark state it remains trapped there and fluorescence ceases. If an applied magnetic field then lifts the degeneracy, the state superposition evolves due to the time evolution of the complex phases of the states with respect to one another and fluorescence resumes. This is known as magentic destabilization of the dark state. However, in the case where the light field is specifically polarized to drive only one type of

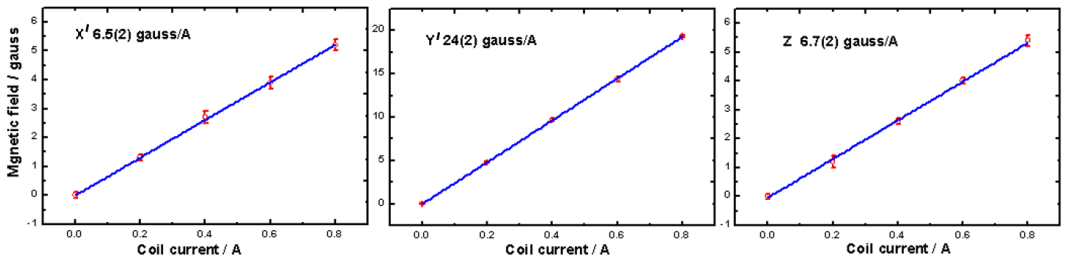

Figure 3.30: Field strengths due to the coils shown in Fig. 3.29 as a function of current. Before the coil assembly was mounted, a Hall probe magnetometer was used to measure the field generated at the centre of the coils as a function of the current in each coil.

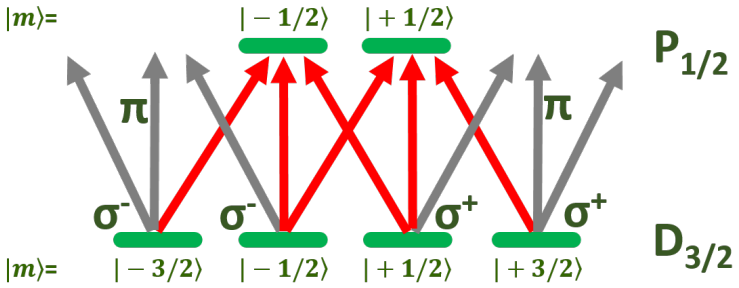

Figure 3.31: Hanle effect. All of the possible transitions from $D_{3/2}$ to $P_{1/2}$ are shown. The dark state is a superposition of those states uncoupled by the repumper, shown in grey.

transition, for example π, the dark state is a superposition of only the $\left|D_{3/2}, m = 3/2\right\rangle$ and $\left|D_{3/2}, m = -3/2\right\rangle$ states, and the evolution of the superposition state involves only these dark states.

As stated, if only π transitions are possible a dark state will ensue. This will be the case if the repumper is linearly polarized along the direction of a quantization axis defined by an applied magnetic field. Practically, this presents a scheme for detecting the presence of a component of the magnetic field perpendicular to the linear polarization of a repumper beam. The polarization of the repumper is prepared horizontally using a polarizing beam splitter, and directed along the x' axis into the trap. Its polarization therefore lies along z. The coil currents are changed to vary the magnetic field in the y' and x' directions until the fluorescence is minimized. The minimum occurs when there is only a component of the field along the z direction because the condition is fulfilled that the quantization axis is collinear with the polarization of the repumper: only π transitions are excited and the ion is trapped in the dark state superposition of the $\left|D_{3/2}, m = \pm 3/2\right\rangle$ states.

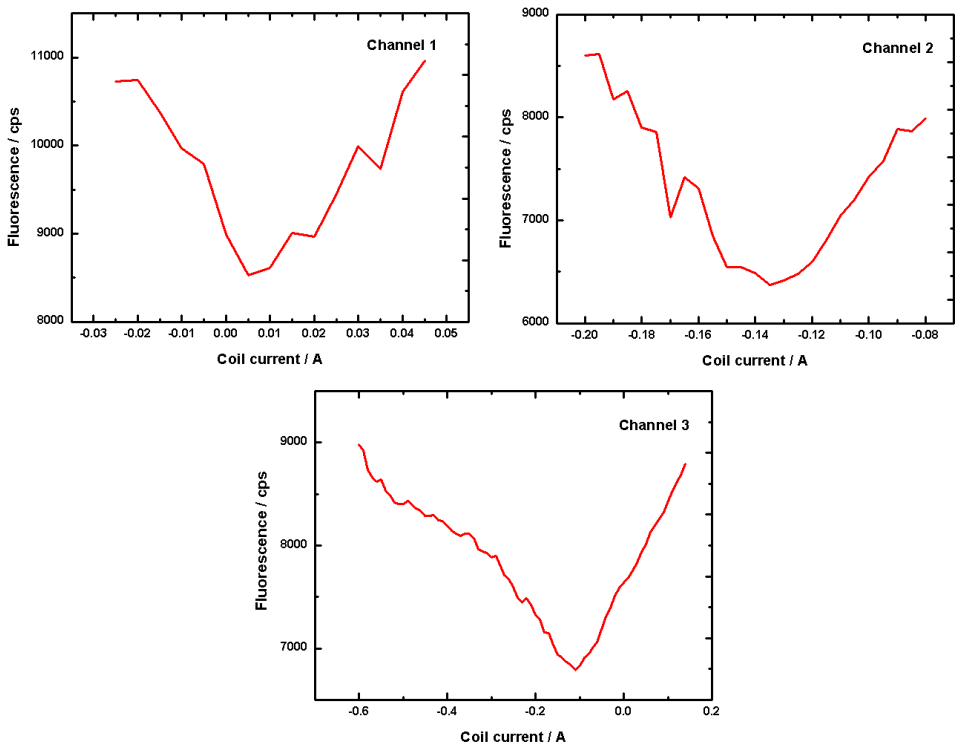

Figure 3.32: Observation of ground state Hanle effect. Dips are observed while scanning the coil current in each spatial direction, with the 866 nm repumper linearly polarized in a perpendicular direction.

With the field thus canceled along the y' and x' axes, the polarization of the repumper is changed to vertical. The magnetic field is then similarly canceled in the z direction.

The results are shown in Fig. 3.32. In general, once the magnetic field is compensated in all three directions, the dark state is destabilized through application of sufficient field in order for efficient cooling to take place.

3.4.5 Trap secular frequency measurements

The trapping theory presented in section 2.1 shows that the confinement of the ions in the trap is characterized by two parameters q and a. Measurement of the q parameter is desirable as it confirms that the circuit which applies resonant rf voltage onto the radial electrodes is functioning properly, and that there is sufficient confinement in a range where the ion is stable. In the multi-ion cavity coupling experiments in chapter 4, the inter-ion spacing is a critical parameter, so precise axial secular frequency calibration of the endcap electrode voltage source is necessary. q and a are found from fits to measurements of

the radial and axial secular frequencies as a function of voltages applied to the radial rf electrodes and the dc endcap electrodes U_{rf} and U_{dc}.

To excite the motion of the ion a sinusoidal voltage is applied to the excitation plate below the trap centre and the frequency changed until a radial or axial excitation is detected in the ion using the CCD camera. Figure 3.33 shows an ion while it is cooled normally (left), and while its axial motion is excited at the secular frequency for the confinement (right). This is repeated for a range of applied voltages, with the the results displayed in Fig. 3.34. The fit to the axial secular frequency curve give values of $-8 \times 10^{-4} < a < 0$ for our accessible range of 0 to 650 V, limited by the rating on the vacuum feedthroughs. In the radial secular frequency measurement $0 < q < 0.96$ for the operating range of the rf amplifier. During the experiments in this thesis, the rf confinement is set at $q = 0.2$.

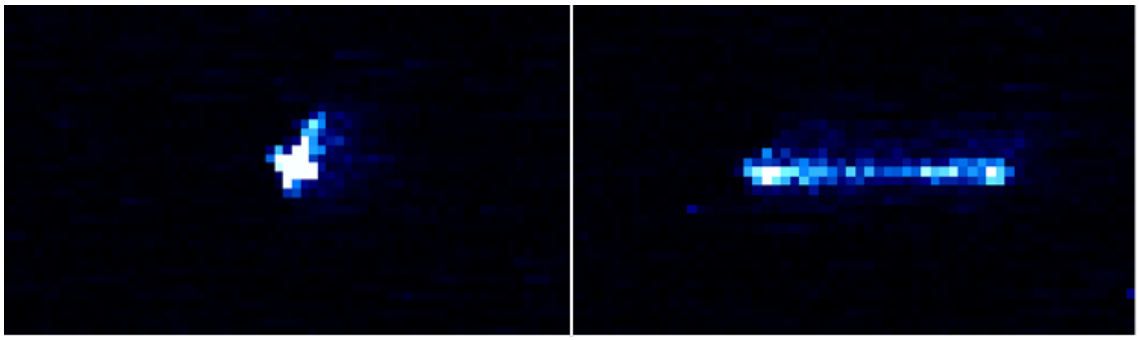

Figure 3.33: Excitation of ion at secular frequency. An ion while cooling normally (left), and while exciting the axial motion at the secular frequency.

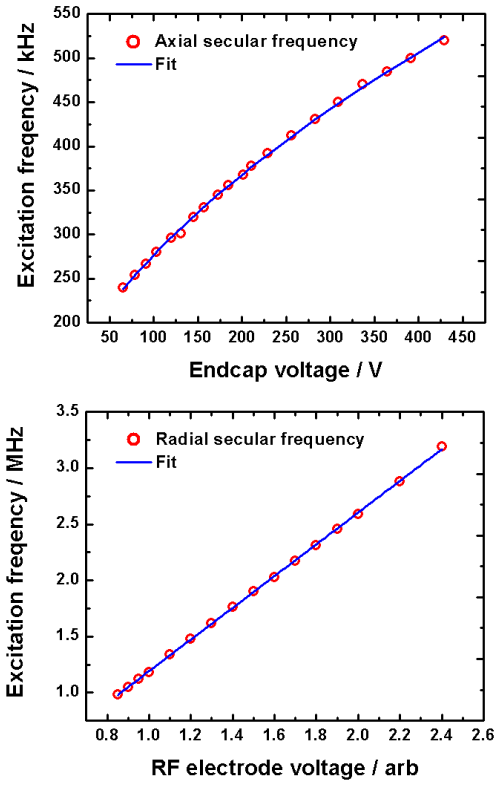

Figure 3.34: Secular frequency measurements. The errors are smaller than the data points.

Chapter 4

Optimized multi-ion cavity coupling

The overall aim of our QCED apparatus is to create multi-ion cluster states, through the cavity-mediated entanglement of pairs of ions in a string. The efficiency of the entanglement generation relies heavily on the optimization of the coupling of each individual ion to the cavity. In the radial direction, the cavity mode has a Gaussian distribution and the highest coupling is experienced by ions at its midpoint. Section 3.2.4 contains a detailed account of the positioning of the ions at the radial centre of the cavity. In the axial direction, the cavity mode has a sinusoidal standing wave structure, with points of maximum coupling at the anti-nodes. The axial equilibrium positions of the ions are determined by their mutual Coulomb repulsion and the axial confinement generated by the dc endcap electrode voltages. By varying these voltages, we therefore have a means to change the inter-ion spacings in a string until those spacings correspond closely to integer multiples of half of the wavelength of the cavity field, i.e. to integer multiples of the spacing between anti-nodes. Then, with individual control of the positions of the cavity mirrors via their PZTs, the cavity can be translated so that the equilibrium positions of all the ions approach anti-nodes of the field where their coupling strength is highest.

In contrast to a point particle positioned at an anti-node, which would experience a coupling strength of g_0 as defined in section 2.3, each ion has a wave function with a finite spread along the axial direction. The degree of localization of strings of ions is in the Lamb-Dicke regime, in which the spread in the wave functions of the ions are less than the cavity mode wavelength [53]. It will be shown that the wave function is Gaussian whose variance gives this spread. The variance is a function of both the temperature of the ion and the axial confinement it experiences. Therefore an ion, whose equilibrium position is

at an anti-node, experiences a spread of values of g centered about g_0, so that the average coupling strength of each ion goes down with temperature and up with confinement. It is desirable to maintain a low ion temperature, in order to mitigate the excursion of the ions from their near anti-nodal equilibrium positions.

The experiment described in this chapter seeks to quantify the degree to which we can deterministically optimize the equilibrium positions of up to five ions with respect to the cavity standing wave. In addition we gain information about the temperature of the ions to determine the spread of their wave functions.

The data take the form of visibility measurements. Here, one or more ions are trapped and cooled for some value of the axial confinement. With the cavity length-locked on Raman resonance with the 866nm $P_{1/2}$ to $D_{3/2}$ transition, the cooling laser serves to continuously drive cavity-assisted Raman transitions at a rate proportional to the convolution of the absolute square of the ions' wave function with the intensity function of the cavity field. The cavity emission is detected, with the signal proportional to the sum of the emission for each ion. The locked cavity is then translated axially and the change in rate of emission recorded. For a single ion, this is a sinusoid whose maxima and minima coincide with the instances where the ion is at an anti-node and node respectively. The spread in the ion's wave function about its equilibrium position attenuates the amplitude of the sinusoid compared to that which would be seen in the case of a point-like emitter, quantified by the visibility of the change in emission during the translation. It will be shown that for a given temperature, the visibility increases monotonically with axial confinement. With more than one ion in a string, translation of the cavity for a given confinement still yields a sinusoid in emission. However, when the confinement is changed and the cavity translated, the visibility of the emission as a function of confinement has local maxima corresponding to the ions' equilibrium positions approaching anti-nodal points in the cavity field. For more ions the visibility pattern becomes more complex. Nonetheless, it will be seen that the data fits the model well, indicating that the ions may be deterministically localized in the cavity field. Our experimental range of confinements is limited by the voltage ratings on the vacuum feedthroughs. However, we control the positions of four and five ions to achieve an average cavity coupling of greater than 98% of the value which they would experience in the ideal case of their equilibrium positions coinciding exactly with anti-nodes. Furthermore, the effective confinement of the ions increases with ion number due to their mutual Coulomb repulsion, manifested in the presence of higher order vibrational modes in the string. The contribution of higher vibrational frequencies associated with these

modes leads to significantly higher values of the visibility than that found for a single ion confined with the centre of mass (COM) frequency. The increase in visibility corresponds to a smaller spread in each ion's wave function, and therefore a smaller spread in coupling.

The first part of this chapter focuses on determining the cavity emission of a single ion while it is cooled and the cavity is translated. In section 4.1.1 the Gaussian shape of the wave function of the ions is derived. The ion is treated as a thermal state of the quantum harmonic oscillator at a fixed temperature, and obeying Boltzmann statistics. In these experiments, the cavity emission is proportional to the convolution of the wave function of the ions and the cavity field intensity function. This convolution is calculated in section 4.1.2, and an expression for the visibility is derived in terms of the spread in the wave function of the ions. Section 4.1.3 describes the experimental method for obtaining visibility measurement for a single ion.

The second part of the chapter treats visibility measurements performed with strings of ions trapped in the cavity mode. In section 4.2.1, the equilibrium postitions of the ions are calculated, before the additional experimental requirements for many-ion cavity coupling are discussed in section 4.2.2. The contribution to the confinement of higher order modes of vibration is calculated in section 4.2.2. Section 4.2.3 contains the key results and analysis for multi-ion cavity coupling, including the theoretical model used to fit the data.

4.1 Mode-mapping with a single ion

The coupling rate g between a single ion and the cavity field varies with the local field strength at the position of the ion [54]. It is characterized by a standing wave pattern along the cavity axis (z)

$$g(z) = g_0 \cos(kz). \tag{4.1}$$

Here, $2g_0$ is equal to the vacuum Rabi frequency and $k = 2\pi/\lambda$ is the wave number of the cavity field. The radial variation in g is neglected as this changes on a much longer scale than axially.

When continuously driving the cavity-assisted Raman transition described in section 2.3, maximum emission occurs when the equilibrium position of the ion is at an anti-node of the cavity field. If the ion were a point-like particle, emission would be zero at a node. However the ion's position is determined by its wave function, $\Psi(z)$. At finite temperature the ion is in a thermal mixture of states which are each a solution to the Schrödinger equation in a harmonic potential. The axial extent of each solution depends

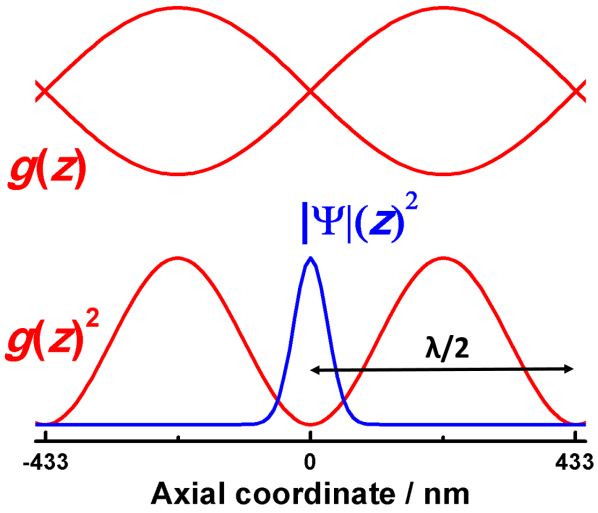

Figure 4.1: Schematic representation of cavity field standing wave $g(z)$, cavity field intensity $g(z)^2$ and absolute square of the ion's position wave function $|\Psi(z)|^2$. The cavity emission is proportional to the overlap of the absolute square of the wave function of the ion $|\Psi(z)|^2$ and the cavity intensity $g(z)^2$. The z axis origin is arbitrarily defined at the position of the ion. In the measurements in this chapter, the cavity field is translated axially along z with respect to the ion(s) position.

on the confining potential, and the weighting of the mixture depends on the temperature of the ion. A convolution of $|\Psi(z)|^2$ and the cavity field intensity $g(z)^2$ will predict the emission, proportional to the degree of coupling, for any axial coordinate z of the ion. The relationship between $g(z)$, $g(z)^2$ and $|\Psi(z)|^2$ is sketched in Fig. 4.1. In the visibility measurements described in this chapter, the cavity field is translated axially with respect to the ion.

4.1.1 Thermal state of the ion

The following derivation of the thermal spread in position of the ion is by Hiroki Takahashi (ITCM). At temperature T the ion is in a statistical mixture of energy eigenstates of the quantum harmonic oscillator with frequency ω. Each state $|n\rangle$ has energy $E_\mathrm{n} = n\hbar\omega$. This thermal state is given by the density operator

$$\rho = \sum_n p_\mathrm{n} |n\rangle\langle n| \tag{4.2}$$

in which p_n is the probability that the ion is in the state $|n\rangle$. This probability is calculated

from the Boltzmann distribution

$$p_{\mathrm{n}} = \frac{\mathrm{e}^{-E_{\mathrm{n}}/k_{\mathrm{B}}T}}{\sum\limits_{n} \mathrm{e}^{-E_{\mathrm{n}}/k_{\mathrm{B}}T}},$$

where k_{B} is Boltzmann's constant. Letting $\beta = \hbar\omega/k_{\mathrm{B}}T$ and evaluating the sum in the denominator gives

$$p_{\mathrm{n}} = \frac{\mathrm{e}^{-\mathrm{n}\beta}}{(1-\mathrm{e}^{-\beta})^{-1}}, \tag{4.3}$$

so that the expression for the density operator is

$$\rho = (1-\mathrm{e}^{-\beta}) \sum_{n} \mathrm{e}^{-n\beta} \left|n\right\rangle\!\left\langle n\right|. \tag{4.4}$$

The probability to find the ion at z is

$$P(z) = \left\langle z\right| \rho \left|z\right\rangle \tag{4.5}$$

$$= (1-\mathrm{e}^{-\beta}) \sum_{n=0}^{\infty} \mathrm{e}^{-n\beta} |\left\langle z\right| n\rangle|^2, \tag{4.6}$$

where $\left\langle z\right| n\rangle$ are the wave functions of the number states. The wave functions are the well-known solutions for the QHO [55] given by

$$\left\langle z\right| n\rangle = \frac{1}{\sqrt{2^n n!}} \left(\frac{m\omega}{\pi\hbar}\right)^{1/4} \mathrm{e}^{-\frac{m\omega z^2}{2\hbar}} H_n\left(\sqrt{\frac{m\omega}{\hbar}} z\right), \tag{4.7}$$

for an ion with mass m, and H_n are the Hermite polynomials. Squaring each wave function and attaching its Boltzmann weighting we have

$$\sum_{n=0}^{\infty} \mathrm{e}^{-n\beta} |\left\langle z\right| n\rangle|^2 = \left(\frac{m\omega}{\pi\hbar}\right)^{1/2} \mathrm{e}^{-\frac{m\omega z^2}{\hbar}} \sum_{n=0}^{\infty} \frac{1}{n!} \left(\frac{\mathrm{e}^{-\beta}}{2}\right)^n H_n^2\left(\sqrt{\frac{m\omega}{\hbar}} z\right), \tag{4.8}$$

and to carry out the summation we use the formula[1]

$$\sum_{n=0}^{\infty} \frac{H_n^2(\alpha)}{n!} \left(\frac{u}{2}\right)^n = \frac{1}{\sqrt{1-u^2}} \mathrm{e}^{\frac{2u}{1+u}\alpha^2}, \tag{4.9}$$

so that Eq. (4.8) now becomes

$$\left(\frac{m\omega}{\pi\hbar}\right)^{1/2} e^{-\frac{m\omega z^2}{\hbar}} \frac{1}{\sqrt{1-\mathrm{e}^{-2\beta}}} \mathrm{e}^{\frac{2\mathrm{e}^{-\beta}}{1+\mathrm{e}^{-\beta}} \frac{m\omega}{\hbar} z^2} \tag{4.10}$$

$$= \left(\frac{m\omega}{\pi\hbar}\right)^{1/2} \frac{1}{\sqrt{1-\mathrm{e}^{-2\beta}}} \mathrm{e}^{-\frac{m\omega}{\hbar} z^2 \left(1 - \frac{2\mathrm{e}^{-\beta}}{1+\mathrm{e}^{-\beta}}\right)} \tag{4.11}$$

$$= \left(\frac{m\omega}{\pi\hbar}\right)^{1/2} \frac{1}{\sqrt{1-\mathrm{e}^{-2\beta}}} \mathrm{e}^{-\frac{m\omega}{\hbar} \tanh\left(\frac{\beta}{2}\right) z^2}. \tag{4.12}$$

[1] Eq (22), 10.13, p. 194, Bateman, Harry (1953) *Higher Transcendental Functions Volume II*. McGraw-Hill Book Company.

The substitution is made in Eq. (4.6), to give the distribution function of the position of ion as

$$P(z) = \sqrt{\frac{1-e^{-\beta}}{1+e^{-\beta}}} \left(\frac{m\omega}{\pi\hbar}\right)^{1/2} \mathrm{e}^{-\frac{m\omega}{\hbar}\tanh\left(\frac{\beta}{2}\right)z^2} \tag{4.13}$$

$$= \left(\frac{m\omega \tanh\left(\frac{\beta}{2}\right)}{\pi\hbar}\right)^{1/2} \mathrm{e}^{-\frac{m\omega}{\hbar}\tanh\left(\frac{\beta}{2}\right)z^2}. \tag{4.14}$$

The ion's spatial dependence along the cavity axis at temperature T is therefore a Gaussian with a spread of

$$\Delta z = \sqrt{\frac{\hbar}{m\omega \tanh\left(\frac{\hbar\omega}{2k_BT}\right)}}. \tag{4.15}$$

If $\hbar\omega \ll k_BT$ then $\tanh\left(\frac{\hbar\omega}{2k_BT}\right) \approx \frac{\hbar\omega}{2k_BT}$ and $\Delta z \approx \sqrt{\frac{2k_BT}{m\omega^2}}$. Putting in values consistent with this experiment, $\omega = 2\pi \cdot 615$ kHz and $T = 750$ μK, we find that the approximation is valid as $\frac{\hbar\omega}{k_BT} = 0.077 << 1$.

The position of the ion has a variance of

$$(\Delta z)^2 \approx \frac{2k_BT}{m\omega_{\mathrm{sec}}^2}, \tag{4.16}$$

where ω_{sec} is the axial secular frequency of the trap due to the dc voltage on the endcap electrodes. The variance depends on the confinement and the temperature. The overlap of the ion's position with the intensity of the cavity field, sketched in Fig. 4.1, gives the emission.

4.1.2 Cavity emission for a single ion

The average cavity emission rate R_{em} is proportional to the position averaged coupling $\langle g^2(z)\rangle$ equal to the convolution of $g(z)^2$ with $|\Psi(z)|^2$. The following derivation of R_{em}, and subsequently the visibility, is by Hiroki Takahashi (ITCM). The functions are

$$|\Psi(z)|^2 = \left(\frac{1}{\pi\Delta z^2}\right)^{1/2} \mathrm{e}^{-\frac{z^2}{\Delta z^2}} \tag{4.17}$$

and

$$g(z)^2 = g_0^2 \cos^2(kz). \tag{4.18}$$

The convolution is

$$\langle g^2(z)\rangle = g_0^2 \int_{-\infty}^{\infty} |\Psi(y)|^2 \cos^2(k(z-y))\, dy \tag{4.19}$$

$$= \frac{g_0^2}{2} \int_{-\infty}^{\infty} |\Psi(y)|^2 \left(1+\cos(2k(z-y))\right)\, dy \tag{4.20}$$

$$= \frac{g_0^2}{2}\left(1 + \frac{1}{2\sqrt{\pi\Delta z^2}} \int_{-\infty}^{\infty} \mathrm{e}^{-\frac{y^2}{\Delta z^2}} \left(\mathrm{e}^{2ik(z-y)} + \mathrm{e}^{-2ik(z-y)}\right)\right) dy, \tag{4.21}$$

and evaluating the integral

$$\int_{-\infty}^{\infty} \mathrm{e}^{-\frac{y^2}{\Delta z^2}+2ik(z-y)}\,dy = \mathrm{e}^{2ikz}\int_{-\infty}^{\infty} \mathrm{e}^{-\frac{y^2}{\Delta z^2}-2iky}\,dy \tag{4.22}$$

$$= \mathrm{e}^{2ikz}\int_{-\infty}^{\infty} \mathrm{e}^{-\frac{1}{\Delta z^2}\left((y+ik\Delta z^2)^2+k^2\Delta z^4\right)}\,dy \tag{4.23}$$

$$= \mathrm{e}^{2ikz}\mathrm{e}^{-k^2\Delta z^2}\int_{-\infty}^{\infty} \mathrm{e}^{-\frac{(y+ik\Delta z)^2}{\Delta z^2}}\,dy \tag{4.24}$$

$$= \mathrm{e}^{2ikz}\mathrm{e}^{-k^2\Delta z^2}\sqrt{\pi\Delta z^2}. \tag{4.25}$$

It can be shown through complex analysis [51] that $\int_{-\infty}^{\infty} \mathrm{e}^{-\frac{(y+ik\Delta z)^2}{\Delta z^2}}\,dy = \int_{-\infty}^{\infty} \mathrm{e}^{-\frac{y^2}{\Delta z^2}}\,dy$, and the identity $\int_{-\infty}^{\infty} \mathrm{e}^{-\frac{y^2}{\Delta z^2}}\,dy = \sqrt{\pi\Delta z^2}$ has been used. The result in Eq. (4.25) is substituted back into Eq. (4.21), so that

$$\left\langle g^2(z)\right\rangle = \frac{g_0^2}{2}\left(1+\frac{1}{2}\mathrm{e}^{-k^2\Delta z^2}(\mathrm{e}^{2ikz}+\mathrm{e}^{-ikz})\right) \tag{4.26}$$

$$= \frac{g_0^2}{2}\left(1+\mathrm{e}^{-k^2\Delta z^2}\cos(2kz)\right), \tag{4.27}$$

giving an expression for the average cavity emission

$$R_{\mathrm{em}}(z) \propto \frac{g_0^2}{2}\left(1+\mathrm{e}^{-k^2\Delta z^2}\cos(2kz)\right). \tag{4.28}$$

The maximum and minimum signals are expected when $\cos(2kz) = 1$ and -1 so

$$\left\langle g^2(z)\right\rangle_{\max} = \frac{g_0^2}{2}(1+\mathrm{e}^{-k^2\Delta z^2}), \tag{4.29}$$

$$\left\langle g^2(z)\right\rangle_{\min} = \frac{g_0^2}{2}(1-\mathrm{e}^{-k^2\Delta z^2}), \tag{4.30}$$

and the visibility may be defined by

$$V = \frac{\left\langle g^2(z)\right\rangle_{\max}-\left\langle g^2(z)\right\rangle_{\min}}{\left\langle g^2(z)\right\rangle_{\max}+\left\langle g^2(z)\right\rangle_{\min}} = \mathrm{e}^{-k^2\Delta z^2}. \tag{4.31}$$

4.1.3 Visibility of a single ion

In order to increase the visibility of the cavity emission, the temperature of the ion must be reduced. To achieve the lowest possible temperature, the 397 nm beam is kept at a low power (600 nW) in order to minimize its broadening effect on the transition, and is frequency detuned to $\Gamma/2$ (see section 2.2.2 on laser Doppler cooling). This laser serves two purposes: to cool the ion close to the Doppler cooling limit, and to continuously drive one arm of a cavity-assisted Raman transition from the $S_{1/2}$ ground state to the $D_{3/2}$ state. Using one of the cavity mirror PZTs, the cavity is length-locked into Raman resonance with the 397 nm cooling laser, while the ion is continuously cooled, driving the emission of 866 nm Raman photons into the cavity mode. The voltage on the other PZT is smoothly

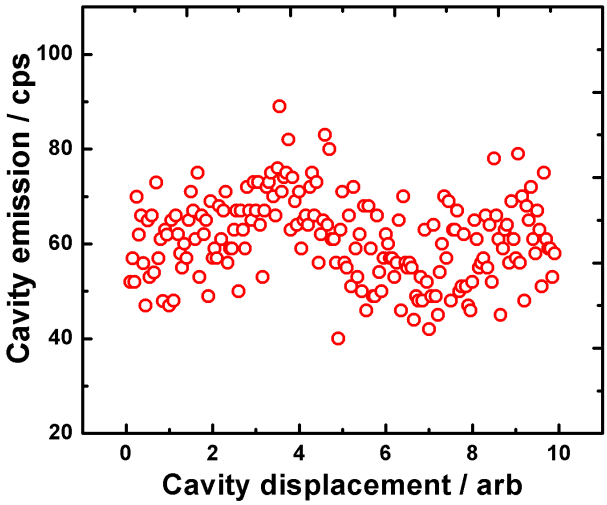

Figure 4.2: Calibration file used for in-coupling background subtraction. The locked cavity is translated over the experimental range. Shown is the variation of the contribution from the 894 nm locking light due to the change in in-coupling to the cavity.

ramped in order to translate the cavity with respect to the ion while the cavity emission is monitored with the single photon counting module (SPCM).

When translating the cavity, there are changes both in the in-coupling of the locking light from the stable 894 nm reference laser, and the out-coupling of light in the cavity. Therefore two distinct types of calibration file are taken in order to compensate for these changes which result from the movement of the CQED system in the laboratory frame.

The variation in in-coupling is compensated by locking the cavity length and translating it over the experimental range without ions present. The SPCM signal is recorded and this is later subtracted from each dataset before the fitting routine takes place. This amounts to removing a position-dependent background from the raw data. An example of the background calibration file is shown in Fig. 4.2.

In order to compensate the change in coupling between the output mirror of the cavity and the detection fiber leading to the SPCM, a string of six ions is loaded and the axial confinement relaxed in order for the string to become kinked. The ions are Doppler cooled with high intensity 397 nm light in order to broaden the transition and raise the temperature of the ions as much as possible. It was found that under these conditions, any remaining visibility was dominated by a pattern characteristic of translation of the cavity under these conditions. A very large crystal would in principle have given the best calibration file of this type. However, this type of calibration measurement was

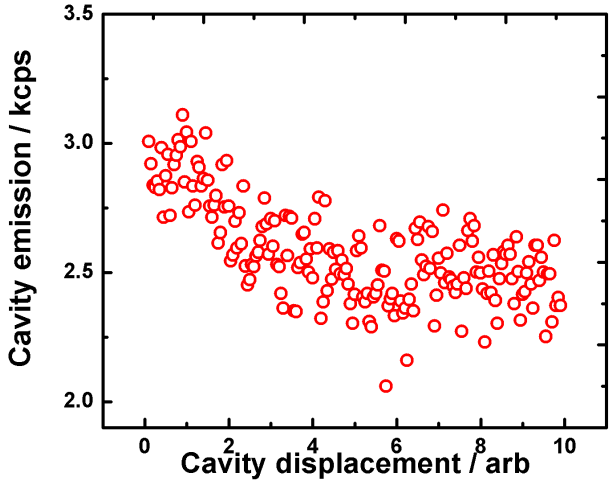

Figure 4.3: Calibration file used for scaling data against change in out-coupling. The locked cavity is translated over the experimental range with a hot non-linear crystal of six ions brightly fluorescing. The change in signal reflects the change in out-coupling as the cavity position is scanned.

not used due the undetectable loss of individual ions from the ensemble, leading to an unquantifiable drop in signal with time, so therefore the calibration files were taken with a clearly defined constant number of ions in the trap. After the cavity was translated and the signal recorded, it was used as a data point-wise divisor to scale each dataset after the subtraction of the in-coupling compensation file. An example of the scaling file to compensate the changes in out-coupling is shown in Fig. 4.3.

After calibrating the raw data the sinusoidal dependence on position of the ion's emission into the cavity is clear in Fig. 4.4. The contrast of the pattern is determined by the degree of localization of the ion and is given by Eqs. (4.31) and (4.16). After each translation a sinusoid is fitted to the dataset and the visibility is calculated from the ratio of the amplitude and the offset. The confinement ω_{sec} was held at 625 kHz and from the measured visibility of 39% a temperature of 1.1 T_{D} was extracted.

4.2 Coupling multiple ions

When multiple ions are coupled to the cavity, the inter-ion spacing plays an important role in the emission as the position of the cavity is changed with respect to the string. Furthermore, the Coulombic interaction present in strings of more than one ion cause an enhancement of the visibility compared with that of a single ion. A model is later

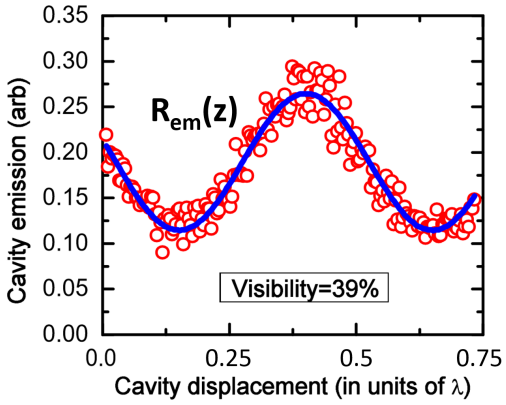

Figure 4.4: Single-ion visibility scan. The cavity emission rate R_{em} (see Eq.4.28) observed as the cavity is translated 0.75λ with respect to the position of the ion. The visibility of 39% is calculated from the ratio of the amplitude to the offset of the fit. The far-detuned laser is not switched on during this measurement.

presented which accounts for the increase in visibility in terms of the effect of higher order vibrational modes on the spread in each ion's position. The fundamental centre of mass (COM) mode frequency of vibration ω_{COM} is identical to the axial secular frequency mentioned previously in this thesis so $\omega_{\mathrm{COM}} = \omega_{\mathrm{sec}}$.

4.2.1 Equilibrium positions in multi-ion string

The axial equilibrium positions of the ions are calculated following the derivation by James [56]. The potential energy of a string of N ions of mass M in a confining potential characterized by the axial secular frequency ω_{sec} is

$$V = \sum_{m=1}^{N} \frac{1}{2} M \omega_{\mathrm{sec}}^2 z_m(t)^2 + \sum_{\substack{n,m=1 \\ m \neq n}}^{N} \frac{e^2}{8\pi\epsilon_0} \frac{1}{|z_n(t) - z_m(t)|}, \tag{4.32}$$

where e is the electron charge, ϵ_0 is the permitivity of free space and $z_m(t)$ is the instantaneous position of the mth ion in the string. If the ions are sufficiently cold, the position of the mth ion may be approximated by $z_m(t) \approx z_m^{(0)} + q_m(t)$, where $z_m^{(0)}$ is the equilibrium position of the ion and $q_m(t)$ is a small displacement. The equilibrium positions of the ions are found through:

$$\left[\frac{\partial V}{\partial z_m}\right]_{z_m = z_m^{(0)}} = 0. \tag{4.33}$$

A length scale l may be defined by

$$l^3 = \frac{e^2}{4\pi\epsilon_0 M \omega_{\mathrm{sec}}^2} \tag{4.34}$$

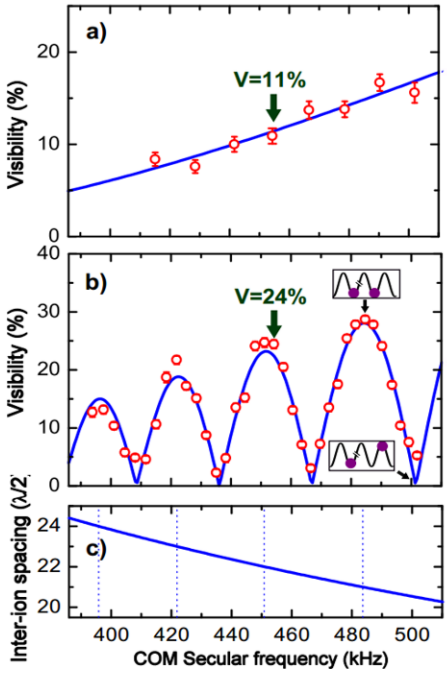

Figure 4.5: Visibility measurement results for (a) a single ion and (b) two ions, as the COM frequency is varied. The blue curves are a fit to the data with our theoretical model, from which the temperature may be extracted. This is found to be $\approx 1.5T_D$ for both datasets. The increase in temperature with respect to the data in Fig. (4.4) is due to the far-detuned stabilizing beam. The insets in (b) show schematically the extreme cases where the two-ion visibility is maximized and when it is entirely washed out due to the ions' separation. (c) shows the calculated inter-ion spacing as a function of the axial COM frequency.

to give the dimensionless equilibrium coordinate $u_m = z_m^{(0)}/l$. Differentiating V with respect to each of the N ions' coordinates, evaluated at their equilibrium positions, yields N coupled equations for u_m:

$$u_m - \sum_{n=1}^{m-1} \frac{1}{(u_m - u_n)^2} + \sum_{n=m+1}^{N} \frac{1}{(u_m - u_n)^2} = 0 \quad (m = 1, 2, ..., N). \tag{4.35}$$

The solutions to these equations give the equilibrium positions and these are listed in [56] for up to ten ions.

4.2.2 Visibility measurements of more than one ion

The cavity emission rate takes the form $\sum_i R_{\rm em}(z_i)$, where each term $R_{\rm em}(z_i)$ is the emission rate for the ith ion in the string, as in Eq. (4.28). Figures 4.5(a) and (b) show the results of discrete visibility measurements taken for different axial secular frequencies

with a single ion (a) and two ions (b) coupled to the cavity. Each red circle is the result of a visibility measurement taken at a fixed secular frequency. In each case the visibility is extracted through a sinusoidal fit, and the error bars are the combined uncertainties in the best fit parameters. The single ion data in Fig. 4.5(a) clearly shows the monotonic dependence of the visibility on the axial secular frequency for a fixed temperature. The range of secular frequencies probed during these scans was established in the following way. The shape of a single species ion crystal is generally determined by the ratio of the radial and axial secular frequencies [56]. It is found empirically that the high radial confinement of 1.23 MHz, required to prevent a five-ion string from kinking, causes the longer ion strings to frequently become delocalized with a steep drop in both fluorescence and cavity emission. We conjecture that the longer strings present a larger cross section for collisions with background gas, while absorbing more heat from electrical noise on the rf trap electrodes. As a result of a collision, the temporary Doppler shift disrupts the cooling dynamics and the ions become delocalized before eventually being cooled back to their stable equilibrium positions in a timescale on the order of a second. The drops in cavity emission have a detrimental effect on the quality of the sinusoidal fits from which we extract the visibility. We therefore employ a far-detuned 397 nm beam in addition to the primary cooling laser, aligned radially to the trap and cavity axis, with a power of 2.1 μW and a detuning of 6.5 Γ (150 MHz). The large detuning minimizes the heating effects due to unwanted continuous extra scatter of photons, while serving to Doppler cool the ions when (and only when) they have acquired a large momentum during a collision. In order to compare the results of visibility measurements for ion strings of different length, the far-detuned laser was employed even for strings with low number of ions, to satisfy the requirement for consistency with the other datasets. It is emphasized that the demonstration single-ion dataset in Fig. 4.4 was taken under ideal conditions of maximum axial confinement and without the far-detuned laser. The requirement to have linear strings and to limit the amount of suspected rf heating in the longer strings, placed an upper limit on the radial secular frequency, which in turn limited the axial secular frequency range available to avoid kinking the strings. For consistency, the trapping regime required by the five-ion string was extended to all the other datasets, with the exception of the model dataset in Fig. 4.4.

The dependence of the visibility on the inter-ion spacing is now condsidered for the case of two ions. Figure 4.5(c) shows the calculated inter-ion spacing for a two-ion string as a function of confinement. The dotted blue lines indicate for which secular frequencies the

inter-ion spacing becomes equal to an integer multiple of half the cavity field wavelength, $n\lambda/2$. As indicated schematically in the insets in Fig. 4.5(b), at these secular frequencies the positions of the two ions are simultaneously nodal or anti-nodal in the cavity field and they will make an in-phase contribution to the emission while the cavity is translated: ignoring any mutual interaction between the ions, the signal would double with respect to that of a single ion at every instant during the translation and the single-ion visibility is recovered. If the two ions are separated by a distance of $(n + \frac{1}{2})\lambda/2$, they make an out-of-phase contribution and the visibility vanishes.

The preceding assertion is only true if the ions do not interact. It is clear from Figs. 4.5(a) and (b) that the visibilities recorded in the one- and two-ion scans are not the same when similar confinements are compared; at 454 kHz the two-ion data shows an increase of a more than a factor of two in the visibility when the two ions are separated by $n\lambda/2$. The reason for this is that the mutual Coulomb interaction between the ions increases the spatial confinement felt by each. The greater confinement is a result of the contributions of higher order modes of vibration, each with a higher frequency than the fundamental center-of-mass (COM) mode. The COM mode frequency ω_{COM} is characterized for various endcap potentials in the measurements of the secular frequency in section 3.4.5 in chapter 3. The measurements are for a single ion, therefore only the COM mode is present: $\omega_{\mathrm{COM}} = \omega_{\mathrm{sec}}$. In order to analyze the contributions of higher order modes to the vibrational frequency of the ions, and thus to the confinement and change in spread in position that they experience, Eq. (4.16) cannot be applied directly, due to the time-dependent coupling between the ions. In the following section a modified expression for the spread in position Δz of each ion in a string is derived, which takes into account the interaction between the ions.

Higher order modes of vibration

The reduced spread in the positions of the ions, seen when comparing the datasets in Figs. 4.5(a) and (b), cannot be calculated directly from Eq. (4.16) due to the ions' mutual interaction. Instead we transform the motion to a set of non-interacting normal modes of vibration, each of which evolves independently from the others. The variance in amplitude of each these modes can be found from Eq. (4.16), which can be transformed back into an expression for the variance in position of the ions.

Again following James [56] to derive the amplitudes of the higher order modes, the

Lagrangian for the motion of the ions is

$$L = \frac{M}{2}\sum_{m=1}^{N}(\dot{q}_m)^2 - \frac{1}{2}\sum_{n,m=1}^{N} q_n q_m \left[\frac{\partial^2 V}{\partial z_n \partial z_m}\right]_{q_n=q_m=0}. \tag{4.36}$$

The expression for the potential energy is a Taylor approximation[2], in which the first two terms are zero (as it is a potential energy function evaluated at its minimum) and terms of order q_n^3 and higher are ignored. The validity of the approximation is justified in [56]. Calculating the partial derivatives gives

$$L = \frac{M}{2}\left[\sum_{m=1}^{N}(\dot{q}_m)^2 - \omega_{\text{sec}}^2 \sum_{n,m=1}^{N} A_{nm} q_n q_m\right], \tag{4.37}$$

with

$$A_{nm} = \begin{cases} 1 + 2\sum\limits_{\substack{p=1 \\ p\neq m}}^{N} \frac{1}{|u_m - u_p|^3} & \text{if } n = m; \\ \frac{-2}{|u_m - u_n|^3} & \text{if } n \neq m. \end{cases} \tag{4.38}$$

A_{nm} is a real, non-negative definite, symmetric matrix with non-negative eigenvalues. Therefore we can write the eigenvalue equation for the eigenvectors $\boldsymbol{b}_m^{(p)}$ $(p = 1, 2, ..., N)$ as

$$\sum_{n=1}^{N} A_{nm}\boldsymbol{b}_n^{(p)} = \mu_p \boldsymbol{b}_m^{(p)} \ (p = 1, ..., N) \tag{4.39}$$

where $\mu_p \geq 0$ are the eigenvalues and the eigenvectors are numbered in order of increasing eigenvalue. For $N = 2$ and $N = 3$ ions, these may be calculated algebraically and are

$$\begin{aligned} N = 2: \quad & \boldsymbol{b}^{(1)} = \tfrac{1}{\sqrt{2}}(1, 1), && \mu_1 = 1, \\ & \boldsymbol{b}^{(2)} = \tfrac{1}{\sqrt{2}}(-1, 1), && \mu_1 = 3, \\ N = 3: \quad & \boldsymbol{b}^{(1)} = \tfrac{1}{\sqrt{3}}(1, 1, 1), && \mu_1 = 1, \\ & \boldsymbol{b}^{(2)} = \tfrac{1}{\sqrt{2}}(-1, 0, 1), && \mu_1 = 3, \\ & \boldsymbol{b}^{(3)} = \tfrac{1}{\sqrt{6}}(1, -2, 1), && \mu_1 = 29/5. \end{aligned} \tag{4.40}$$

The eigenvectors correspond to normal modes of oscillation, with N modes present in a string of N ions. Higher order modes when $p \geq 4$ require numerical calculation, and are presented in [56] for up to ten ions. The first eigenmode $p = 1$ is known as the centre of mass (COM) mode, and corresponds to all N ions moving in the same direction. They oscillate at the COM frequency $\omega_{\text{COM}} = \omega_{\text{sec}}$ which is the same as the secular frequencies

[2]Eq. (5.107), p.358, Ch 5, Arfken, George B. and Weber, Hans J. (2005) *Mathematical Methods for Physicists (Sixth Edition)* Elsevier Academic Press

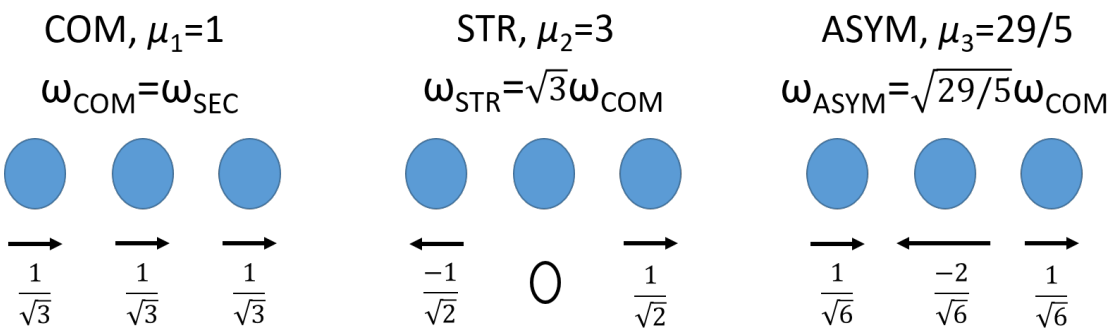

Figure 4.6: Modes of oscillation for $N = 3$ ions. Schematic representations of the centre of mass (COM), stretch (STR) and asymmetric (ASYM) modes are shown with eigenvalues μ and oscillation frequencies ω relative to the COM mode.

recorded in the measurements in section 3.4.5 of chapter 3. The next mode $p = 2$ is known as the stretch (STR), or breathing, mode in which each of the ions oscillate in the same direction as the displacement of their equilibrium position from the trap centre. Movement associated with the asymmetric (ASYM) mode $p = 3$ in the case of three ions, sees the outer ions move in the same direction, while the inner ion moves in the opposite direction with twice the amplitude. Fig 4.6 illustrates the first three normal modes for the case of $N = 3$ ions. Each mode oscillates with a frequency which is higher than the COM mode by a factor equal to the square root of its eigenvalue. The normal mode oscillations $Q_p(t)$ are defined by

$$Q_p(t) = \sum_{m=1}^{N} \boldsymbol{b}_m^{(p)} q_m(t) \tag{4.41}$$

The increased visibility seen in the two ion data is explained by the contribution of these normal modes to the confinement of the ions. The following derivation of the modification to the spread in position due to the higher motional modes is due to Hiroki Takahashi (ITCM). A matrix B is defined:

$$B = [\boldsymbol{b}^{(1)}\, \boldsymbol{b}^{(2)} ... \boldsymbol{b}^{(N)}] \tag{4.42}$$

$$B_{ip} = \boldsymbol{b}_i^{(p)}. \tag{4.43}$$

B is orthogonal such that ${}^{\mathrm{T}}B\, B = B\, B^{\mathrm{T}} = 1$ where B^{T} is the transpose of B. From Eq. (4.41) we have

$$Q_p(t) = \sum_{m=1}^{N} B_{mp} q_m(t) = \sum_{m=1}^{N} {}^{\mathrm{T}}B_{pm} q_m(t) \tag{4.44}$$

Now each ion's displacement may be written in terms of B and the normal mode displace-

ments

$$q_m(t) = \sum_{p=1}^{N} B_{mp} Q_p(t). \tag{4.45}$$

The variance in the mth ion's position Δq_m^2 is

$$\Delta q_m^2 = \langle q_m^2 \rangle - \langle q_m \rangle^2. \tag{4.46}$$

The average position of the ion is its equilibrium position so the second term is equal to zero, and using Eq. (4.46):

$$\begin{aligned}
\Delta q_m^2 &= \left\langle q_m^2 \right\rangle && (4.47)\\
&= \left\langle \left(\sum_{p=1}^{N} B_{mp} Q_p \right)^2 \right\rangle && (4.48)\\
&= \left\langle \sum_{p=1}^{N} \sum_{p'=1}^{N} B_{mp} B_{mp'} Q_p Q_{p'} \right\rangle && (4.49)\\
&= \left\langle \sum_{p=1}^{N} \left(B_{mp} Q_p \right)^2 \right\rangle + \left\langle \sum_{\substack{p,p'=1 \\ p \neq p'}}^{N} B_{mp} B_{mp'} Q_p Q_{p'} \right\rangle. && (4.50)
\end{aligned}$$

It is assumed that the contributions from the normal modes are independent and incoherent, so therefore the second term is equal to zero, giving

$$\begin{aligned}
\Delta q_m^2 &= \left\langle \sum_{p=1}^{N} \left(B_{mp} Q_p \right)^2 \right\rangle && (4.51)\\
&= \sum_{p=1}^{N} \left(B_{mp} \Delta Q_p \right)^2. && (4.52)
\end{aligned}$$

The quantity ΔQ_p may now be calculated through an expression analagous to Eq. (4.16)

$$(\Delta Q_p)^2 \approx \frac{2 k_B T}{m \omega_{\mathrm{p}}^2}, \tag{4.53}$$

where ω_{p} is the characteristic frequency of vibration of the pth mode. The spread in the mth ion's position is therefore

$$\Delta q_m = \sqrt{\sum_{p=1}^{N} \left(B_{mp} \Delta Q_p \right)^2}. \tag{4.54}$$

For the case of two ions, $N = 2$ and $B = \frac{1}{\sqrt{2}} \begin{pmatrix} 1 & -1 \\ 1 & 1 \end{pmatrix}$, so that Eq. (4.54) gives their spread in position as

$$\Delta q_1 = \Delta q_2 = \sqrt{\frac{(\Delta Q_{\mathrm{COM}})^2 + (\Delta Q_{\mathrm{STR}})^2}{2}}. \tag{4.55}$$

The second normal mode has a higher eigenfrequency than the first ($\omega_{\mathrm{STR}} = \sqrt{3}\omega_{\mathrm{COM}}$), therefore for the same temperature in each mode, $\Delta Q_{\mathrm{STR}} < \Delta Q_{\mathrm{COM}}$ and $\Delta q_1 = \Delta q_2 < \Delta Q_{\mathrm{COM}}$.

Although we have defined the parameter q to denote excursions from the equilibrium position for notational clarity, the quantity Δq is identical to the spread in the wave function of an ion, Δz in Eq. (4.16). Therefore we may rewrite the above as $\Delta z_1 = \Delta z_2 < \Delta Q_{\mathrm{COM}}$, which means that $\Delta z_{1,2}$ is smaller than Δz for a single ion. The argument can be extended to N ions. This accounts for the greater degree of visibility recorded for the datasets with higher numbers of ions.

4.2.3 Results and analysis

Figure 4.7 shows the results of visibility measurements for strings of three, four and five ions in the same COM frequency range as in Fig. 4.5. Hiroki Takahashi (ITCM) has fitted the blue curves to the data using a theoretical model which is now described. The cavity emission when multiple ions are coupled is proportional to

$$W(\omega_{\mathrm{sec}}, T, \phi) = \sum_{i=1}^{N} g_0^2 \left(1 + \mathrm{e}^{-k^2(\Delta z_i(\omega_{\mathrm{sec}},T))^2} \cos\big(2kz_i^0(\omega_{\mathrm{sec}}) + \phi\big)\right). \tag{4.56}$$

For a given COM confinement frequency ω_{sec}, $z_i^0(\omega_{\mathrm{sec}})$ is the equilibrium position of the ith ion in the string and $\Delta z_i(\omega_{\mathrm{sec}}, T)$ is the thermal spread in position at temperature T. ϕ is the overall phase offset between the ion string and the cavity field. z_i^0 is obtained from Eqs. (4.35) and $\Delta z_i(\omega_{\mathrm{sec}}, T)$ is calculated from Eq. (4.54) assuming equal temperature across all the modes. For a fixed ω_{sec} and T the visibility is calculated from the maximum and minimum values of W obtained by varying the offset phase ϕ. The fitting routine repeats the calculation for a range of values of ω_{sec} while optimizing the temperature T and allowing a horizontal offset in ω_{sec}. The offset in the 1-5 ions datasets was small, not exceeding 1.3 kHz.

Despite the increased complexity in the variation in visibility, the model fits the data well. Three ions in a string still have uniform inter-ion spacing, d_1. In Fig 4.7(a) the three major local maxima correspond to d_1 being equal to an integer multiple of half wavelengths, 20, 19 and 18 in units of $\lambda/2$ at COM frequencies of 411, 444 and 482 kHz. The four- and five-ion strings, however, are characterized by two distinct inter-ion separations [56], d_1 and d_2, illustrated in the figure. The COM frequency can nonetheless be tuned to optimize the simultaneous ion-cavity coupling for the given range. The local maxima marked (i) and (ii) in Fig. 4.7(b) and (c) are now analysed. In a string of four

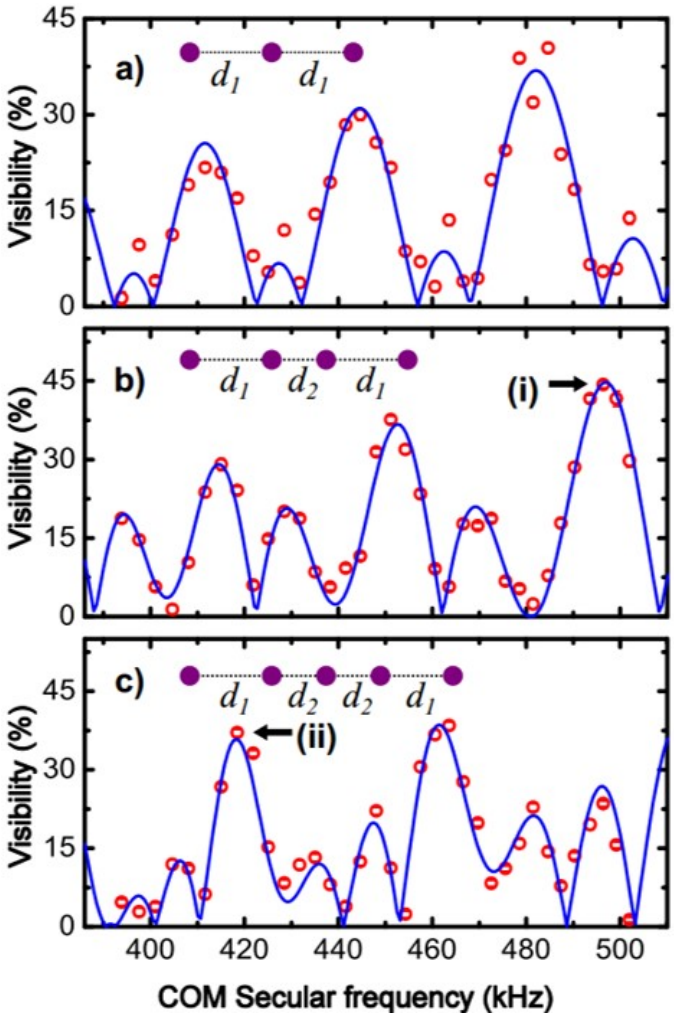

Figure 4.7: Visibility measurement results for (a) three-, (b) four- and (c) five-ion strings. The same temperature is assumed in all normal modes, yielding a temperature of 1.56, 1.57 and 1.72 T_{D} respectively. The insets illustrate how the string configurations depart from a uniform inter-ion spacing in the cases of four and five ions.

ions with a confinement corresponding to (i) the inter-ion distances are extracted from the fit as d_1=16.1, d_2=14.9 in units of $\lambda/2$. In a string of five ions with a confinement corresponding to (ii) the distances are d_1=16.9, d_2=15.1. We define a normalized average coupling strength

$$\tilde{g} = \frac{1}{g_0 N} \sum_{i=1}^{N} \left| g(z_i^0) \right|, \tag{4.57}$$

where $g(z_i^0)$ are calculated ion-wise from Eqs. (4.1) and (4.35) for the individual ion equilibrium positions. It is assumed that the cavity is translated to the position of optimum coupling with respect to the string and that the COM frequencies for four- and five-ion strings are those of (i) and (ii) respectively. $\tilde{g}$ is the average coupling achieved for N ions

as a fraction of that which is experienced by N ions with equilibrium positions coinciding exactly with anti-nodes of the cavity field.

The ion-cavity coupling strengths are (i) $\tilde{g}$=0.988 and (ii) $\tilde{g}$=0.983, showing that it is possible to optimally couple strings of up to five ions in our limited range of confinement with errors of less than 2%. When coupling N ions to the cavity field, the coupling strength scales with $\sqrt{N}$.

Although the purpose of these experiments is to demonstrate control over the precision with which we localize the ions in the cavity standing wave, it is noted that the system reached a collective cooperativity of $Ng_0^2/(\kappa\Gamma) = 0.78$ when five ions were simultaneously coupled. Despite the collective enhancement of the coupling strength, the rate of photon creation in the cavity is nevertheless smaller than the rate of emission. Therefore we do not witness the few-emitter interference effects observed in strongly coupled atomic CQED systems such as those recently reported by Neuzner *et al* in [57].

4.3 Conclusions

Previous work in the field of atomic CQED has focused on coupling either single emitters or very large ensembles, with only an averaged contribution of interest in the latter. Our system has been optimized for the controlled coupling of many ions at anti-nodes of the cavity field, for later utilization in the generation of cluster states.

Up to five ions have been coupled to the cavity mode in a deterministic way. Measurements of visibility of the signal generated by translating the position of the cavity with respect to the ions led to the characterization of the individual coupling of the ions, both in terms of their equilibrium positions in the cavity standing wave, and of the effects of temperature and collective confinement on the thermal spread in their positions. The results agreed well with the theoretical model, indicating that the setup can be used with confidence for schemes to generate many-ion entanglement.

The values for $\tilde{g}$ seen in the experiment can be improved outside the COM secular frequency range explored in these experiments. The model predicts $\tilde{g} \approx 0.999$ is achievable at the readily attainable COM frequencies of 242 and 350 kHz for four and five ions respectively. In addition, it is feasible to couple more than five ions at such low axial confinements. This is because a lower radial confinement will suffice to avoid kinking of the strings. High radial confinement was an empirically determined source of heating, which prevented longer strings to be used in these measurements in the axial confinement ranges chosen.

Chapter 5

Toward coherent ion-cavity coupling

The previous chapter described the work done toward optimally coupling several ions simultaneously to the cavity mode, as a prerequisite for efficient generation of ion-ion entanglement. A further requirement is to initialize each ion in a specific energy level, and coherently couple this to another state via a cavity-assisted Raman transition. When the coupling is switched on, each ion produces a photon in the cavity whose polarization state is entangled with the final electronic state of the ion. Entanglement is heralded through the detection of orthogonally polarized photons in the resulting cavity emission (see section 2.4.1).

The first part of this chapter details work done toward this heralded entanglement scheme, in which a single ion is initialized in a Zeeman substate of the $D_{3/2}$ manifold through optical pumping. Then a control laser drives a cavity-assisted Raman transition to a second Zeeman state, producing a polarized photon in the cavity mode. The work sets the scene for entanglement generation, through duplication of the scheme when two or more ions are simultaneously coupled to the cavity.

Section 5.1.1 details the modifications to the laser systems required for both state preparation through optical pumping and polarized addressing of the Raman transition. Optimization of the state preparation scheme is described in section 5.1.2. An investigation into the degree of magnetic field splitting required to resolve the Raman transitions is contained in section 5.1.3 as well as the steps taken to achieve this. Finally, section 5.1.4 presents the results of a measurement of the purity of the polarization of the emitted photons.

This chapter contains a second part which presents an experiment which follows natur-

ally from the work described above. In a collaborative effort, Kimmo Luoma (Theoretical Quantum Optics group, Dresden University) developed the theoretical framework to explore the non-Markovianity of an ion trapped in a high-finesse cavity, and found that the parameters of our system made it a promising platform. There is currently a significant theoretical interest in the study of non-Markovian dynamics exhibited by open quantum systems [58]. An open quantum system consists of a two-level emitter coupled to a reservoir, for example an atom in vacuum [59]. While theoretical progress has been made, there is a desire for appropriate experimental systems with which to test the theoretical models [60]. The ion trap CQED system is an attractive candidate, as the cavity represents a reservoir with memory. Using the scheme developed in the first part of this chapter, the ion is initialized in a Zeeman state of the $D_{3/2}$ manifold and the Raman drive laser couples it to another Zeeman level with the emission of a photon in the cavity. The coherent ion-cavity evolution is then monitored for observation of the vacuum Rabi oscillation predicted by the Jaynes-Cummings model. While the photon energy oscillates between the cavity Fock state and the atomic qubit state, the cavity decay provides a means to directly measure the probability of the photon occupying the cavity. In our weakly coupled system, the dominant process is the fast decay from the excited $P_{1/2}$ level. Therefore, the experimental sequence is governed by a field-programmable gate array, which carries out a state-dependent fluorescence measurement upon detection of a cavity photon in order to determine the state of the ion. The timestamped cavity signal is discarded in the case of finding the ion in the ground state. This post-selection process eliminates the effect of the $P_{1/2}$ level decay with the intention of revealing the coherent evolution of the coupled system.

The theoretical model for the observation of vacuum Rabi oscillations in our system is presented in section 5.2.1. Section 5.2.2 details the modifications carried out to the system and implementation of the scheme. This includes the optimization of the cooling and state initialization sequence, and the use of a field-programmable gate array to mediate the logic required for post-selecting data via a state detection scheme. The state detection is achieved through electron shelving to a dark state and resonant fluorescence detection. There is a discussion of the addition of the shelving laser and the photon statistics employed in the fluorescence detection. Finally the results are presented and discussed in section 5.2.3.

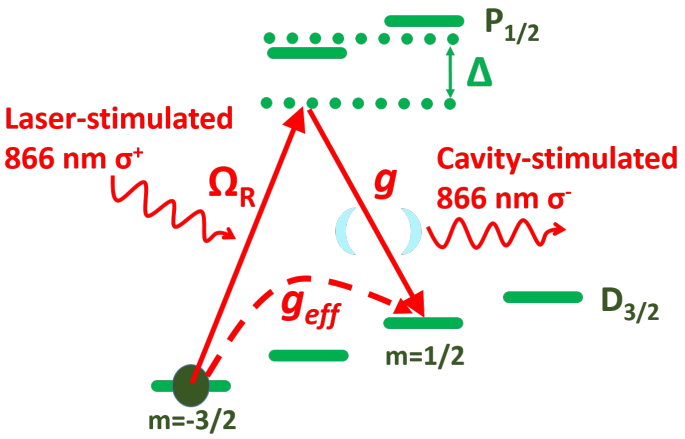

Figure 5.1: Generation of polarized photons. The $\left|\mathrm{D}_{3/2}, m=-3/2\right\rangle$ to $\left|\mathrm{D}_{3/2}, m=1/2\right\rangle$ cavity-assisted Raman transition in which polarized 866 nm light with Rabi frequency Ω_{R} drives the σ^{+} branch while the cavity length is resonant with the σ^{-} branch providing coupling with frequency g. It is emphasized that only one laser is employed to drive the Raman transition. The effective rate of coupling between the levels is g_{eff}. The detuning of the Raman transition from the unshifted $\mathrm{P}_{1/2}$ level is Δ.

5.1 Generation of polarized photons

In our scheme we drive a cavity-assisted Raman transition between sublevels of the $\mathrm{D}_{3/2}$ manifold. In order to do this, a magnetic field is aligned along the cavity length to define the quantization axis. Therefore the cavity supports only left- and right-handed circularly polarized σ^{+} and σ^{-} modes. The ion is prepared in the $\left|\mathrm{D}_{3/2}, m=-3/2\right\rangle$ state through optical pumping, and an 866 nm laser is switched on to drive the σ^{+} branch of the Raman transition. With the magnetic field pointing along the cavity, the other branch must be σ^{+} or σ^{-} with the accompanied emission of a photon in the cavity with right or left circular polarization respectively. With sufficient field to resolve the Zeeman levels, the cavity length is tuned to be resonant with the σ^{-} transition. In this way we drive the $\left|\mathrm{D}_{3/2}, m=-3/2\right\rangle$ to $\left|\mathrm{D}_{3/2}, m=1/2\right\rangle$ coherent Raman transition shown in Fig. 5.1.

To implement the scheme it is necessary to carry out three steps. Initially the ion is optimally cooled, then the repumper lasers are replaced with a 866 nm laser containing polarization components which drive σ^{-} and π transitions in order to optically pump the ion into the $\left|\mathrm{D}_{3/2}, m=-3/2\right\rangle$ state. Finally a pulse of polarized 866 nm light drives the σ^{+} cavity-assisted Raman transition. The emission is detected by the single photon counting module (SPCM) described in section 3.2.3, synchronously gated with the drive laser, and the sequence is repeated. The pulse sequence is shown in Fig. 5.2. These processes are

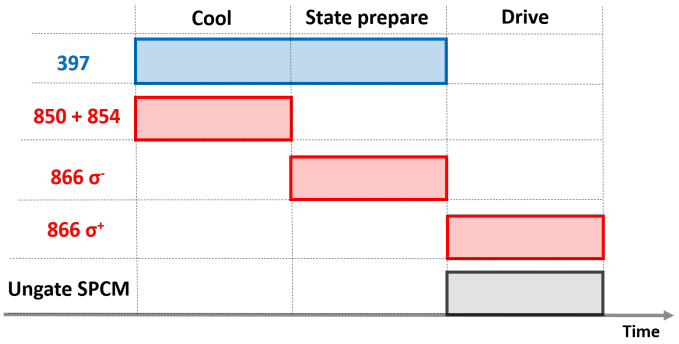

Figure 5.2: Laser pulse sequence for generation of polarized photons. The ion is optimally Doppler cooled with the 397 nm cooling laser and 850 and 854 nm repumpers. Then the repumpers are replaced with light at 866 nm, polarized to drive only the σ^- and π transitions. This optically pumps the ion into the $|D_{3/2}, m = -3/2\rangle$ level, before a differently polarized 866 nm laser drives the σ^+ branch of a cavity-assisted Raman transition.

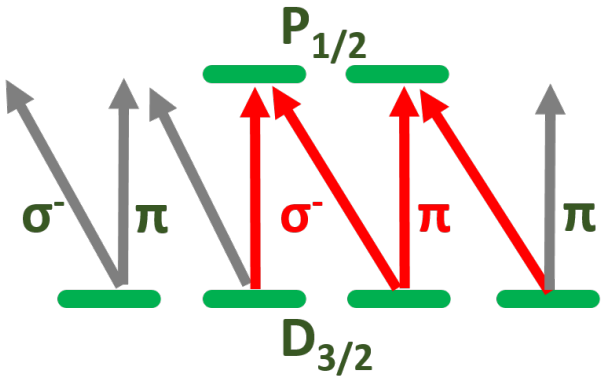

Figure 5.3: Optical pumping. When repumping with 866 nm light polarized to only address σ^- and π transitions, a dark state is reached when the ion is in the $|D_{3/2}, m = -3/2\rangle$ state.

described individually in the following sections.

5.1.1 Polarization of the 866 nm lasers

In order to prepare the desired $|D_{3/2}, m = -3/2\rangle$ state, the repumpers are switched off, and the ion is repumped with a polarized 866 nm beam which addresses only σ^- and π transitions. After some time the repumping will stop when the the ion is in the $|D_{3/2}, m = -3/2\rangle$ state. If the 866 nm beam has a non-zero angle with the quantization axis, the polarization in the frame of the ion will in general address σ^+, σ^- and π transitions. It will be shown below that the polarization of the laser may be modified to prevent excitation of the σ^+ transition. If this is done, it is seen from the structure of the

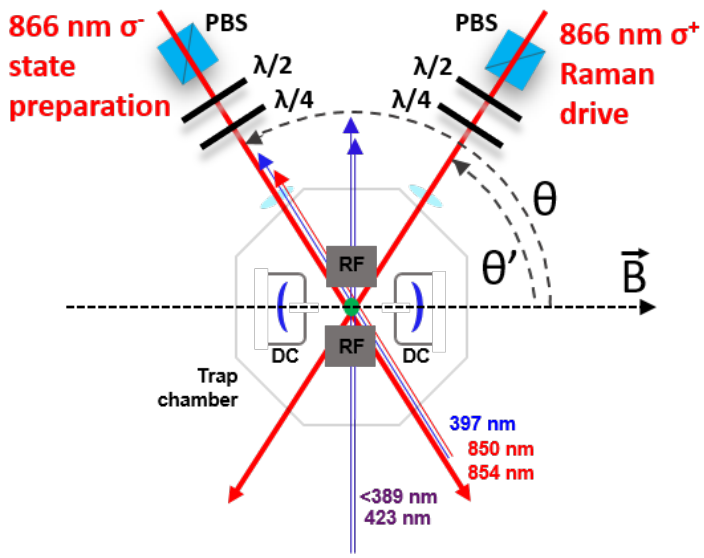

Figure 5.4: New 866 nm lasers and magnetic field alignments. The setup described in section 3.3.1 has been modified to include the 866 nm beams which perform optical pumping (σ^-, π) and drive the Raman transition (σ^+), making angles with the direction of the magnetic field of Θ and Θ' respectively. Each beam passes through polarization optics consisting of a polarizing beam splitter and quarter and half wave plates.

$D_{3/2}$ and $P_{1/2}$ levels that the $\left|D_{3/2}, m = -3/2\right\rangle$ is a dark state, as illustrated in Fig. 5.3.

Two new 866 nm lasers were added to the experimental setup already described in section 3.3.1, with the alignment shown in Fig. 5.4. In order to give the beams the desired polarization, first the fiber out-couplers were rotated to give approximately horizontal polarization, and a polarizing beam splitter placed in front of each to act as a filter. Then, with the polarization horizontal, a half wave plate and a quarter wave plate were added to make an arbitrary polarization, as well as a focusing lens.

In order to prepare the target state through optical pumping it is necessary to eliminate the undesirable circular polarization component in the frame of the ion, for the angle Θ which the laser makes with the magnetic field. This results in a beam which contains only σ^- and π components in a ratio which depends only on Θ. The polarization of the beam along the direction of propagation of the laser may be transformed to the frame of the ion in the magnetic field. The coordinates on the Poincaré sphere can then be found for the laser beam which maximize the desired polarization component in the frame of the field. The full calculation is presented in the thesis of Hendrik-Marten Meyer [61]. The

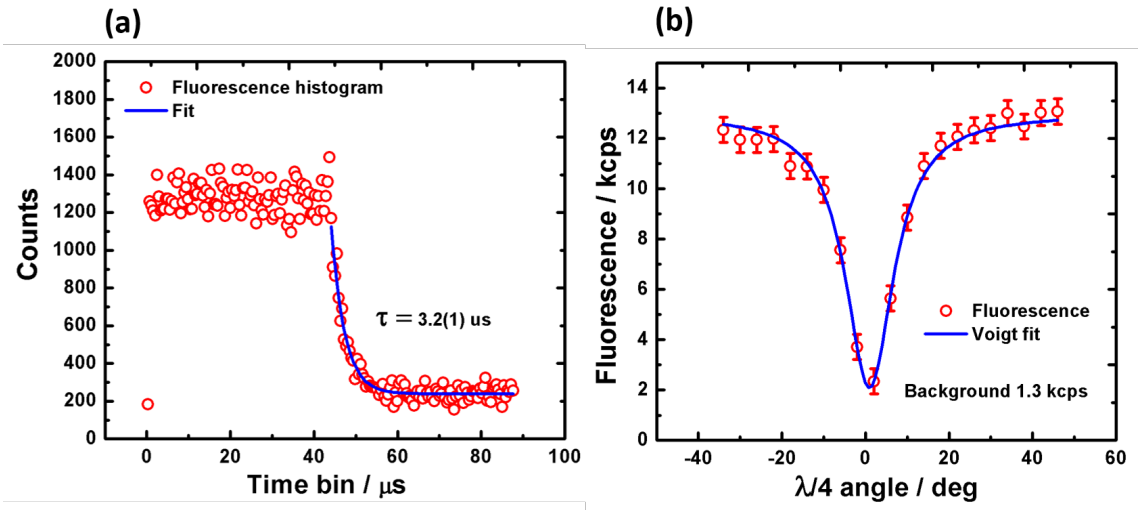

Figure 5.5: (a) Time-resolved fluorescence during cooling and state preparation. After cooling for 45 μs the (σ^-, π) 866 nm laser replaces the repumpers and drives the ion into a dark state at rate of $1/\tau = 310$ kHz. (b) Effect of polarization on the state preparation efficiency. The PMT counter is gated over the steady dark state fluorescence during the state preparation sequence. With the half wave plate fixed, the quarter wave plate is rotated and the fluorescence level recorded. The error bars are the standard deviation of the fluorecence over the timescale of the measurement.

normalized Stokes vector for the optimized polarization is

$$\vec{S} = \begin{pmatrix} S_0 \\ S_1 \\ S_2 \\ S_3 \end{pmatrix} = \begin{pmatrix} 1 \\ \frac{(1-\cos^2(\Theta))}{(1+\cos^2(\Theta)} \\ 0 \\ \frac{(2\cos(\Theta))}{(1+\cos^2(\Theta)} \end{pmatrix}. \tag{5.1}$$

Here, S_0 is the intensity of the beam, S_1 is the linear component of polarization, S_2 is the $\pm 45°$ component and S_3 is the circular component. As the Stokes vector is normalized, $S_0 = 1$. $S_2 = 0$ confirming that there is no superposition of σ^+ and σ^- polarizations, as expected after elimination of one of them. S_3 is the circular component which is positive for σ^+ and negative for σ^-.

The azimuthal and eliptical angles in the Poincaré basis, θ and ϕ, are calculated from the Stokes vector as

$$\theta = \frac{1}{2}\arctan\left(\frac{S_2}{S_1}\right) \tag{5.2}$$

and

$$\phi = \frac{1}{2}\arctan\left(\frac{S_3}{\sqrt{S_1^2 + S_2^2}}\right). \tag{5.3}$$

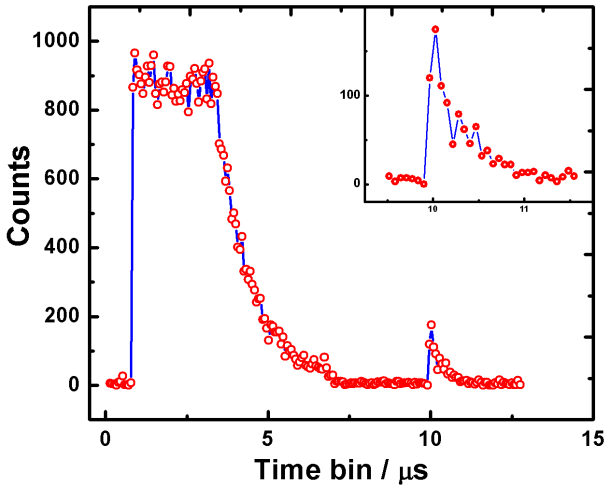

Figure 5.6: Time resolved fluorescence during cooling, state preparation and pulse from σ^+ polarized drive laser. After the dark state is prepared with σ^- light, all the lasers are off for 3 μs, then the drive laser pumps out the prepared $\left|\mathrm{D}_{3/2}, m = -3/2\right\rangle$ state with orthogonal light. The inset shows the peak of 397 nm scatter from the $\mathrm{P}_{1/2}$ level.

In our setup, $\Theta' \approx 58°$ and $\Theta \approx 122°$. The polarization of each beam was measured and the wave plates rotated to give the correct values of θ and ϕ for the elimination of the unwanted component of circular polarization in each beam. The ratio of intensity of the circular polarization to the π component is 2.2 for both beams.

5.1.2 State preparation through optical pumping

After preparing the polarization of the state preparation laser, it was necessary to optimize this, as well as to characterize the optical pumping process. The ion was illuminated by a pulse sequence of optimal cooling followed by state preparation through repumping with the 866 nm (σ^-, π) laser. A time to digital counter was used to produce a time-resolved histogram of the ion fluorescence in order to observe the rate and fidelity of the state preparation, shown in Fig. 5.5(a).

In order to optimize the fidelity of the prepared state, we take advantage of fact that the target state does not fluoresce on the 397 nm transition. A DAQ PMT counter was gated over the last 15 μs of the state preparation portion of the sequence, and the fluorescence minimized through fine adjustment of the angles of the wave plates. Fig. 5.5(b) shows the result of turning the quarter wave plate through the angle at which the fidelity of the dark state preparation was optimized. The effects of the 397 nm and 866 laser powers on

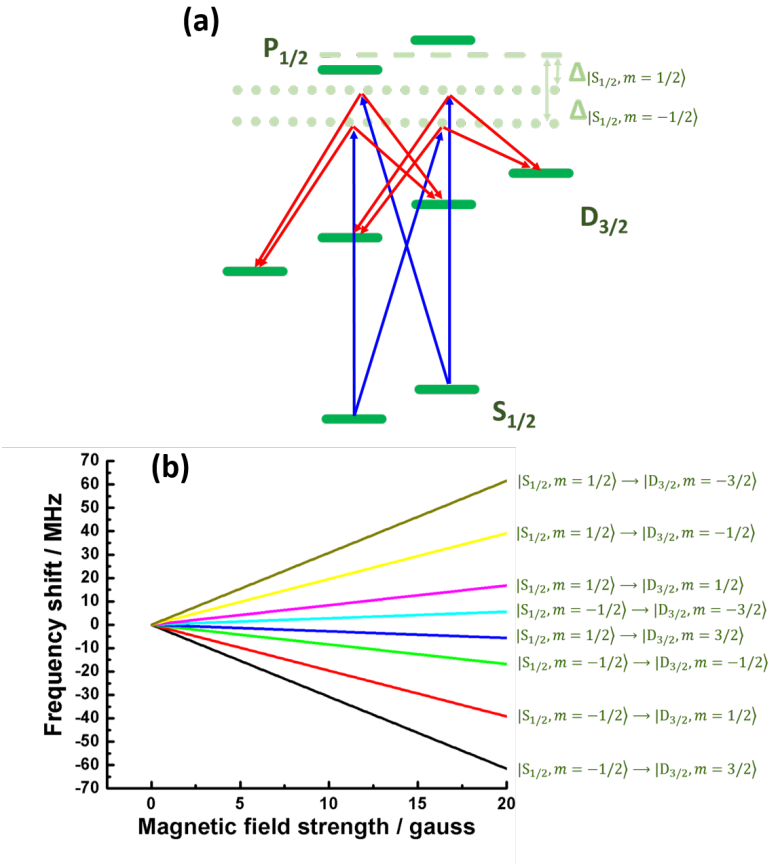

Figure 5.7: (a) Allowed $S_{1/2}$ to $D_{3/2}$ cavity-assisted Raman transitions with quantization axis along cavity. The 397 nm drive laser is shown in blue and the cavity-assisted branch in red. Transitions beginning in the $\left|S_{1/2}, m = \pm 1/2\right\rangle$ levels have different detunings (shown relative to resonance with unshifted $P_{1/2}$ transition). (b) Calculation of Zeeman shifts of $S_{1/2}$ to $D_{3/2}$ Raman transitions due to an applied magnetic field.

the rate and fidelity of the state preparation will be discussed in section 5.2.2.

The polarization of the σ^+ drive laser was similarly optimized and the orthogonality of the circular components of the polarization of the two 866 nm beams was confirmed by extending the state preparation sequence to include a pulse of light from the drive laser. The time-resolved fluorescence in Fig. 5.6 shows the emission peak of 397 nm light at 10 μs as the $\left|D_{3/2}, m = -3/2\right\rangle$ level is pumped out by the drive laser. By contrast, when the third portion of the sequence contained light from the state preparation laser there was no peak visible.

5.1.3 Splitting the $D_{3/2}$ Zeeman sublevels

After preparing the ion in the $\left|D_{3/2}, m = -3/2\right\rangle$ state, the (σ^+, π) laser drives one branch of the Raman transition described above. With the magnetic field pointing along the cavity

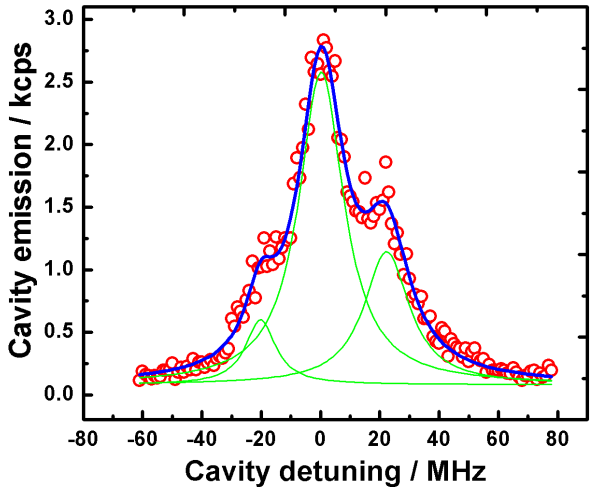

Figure 5.8: $S_{1/2}$ to $D_{3/2}$ magnetic field splitting with old coils. A coarse fit gives an upper limit of approximately 20 MHz for the shift of the $\left|S_{1/2}, m = \pm 1/2\right\rangle$ to $\left|D_{3/2}, m = \mp 3/2\right\rangle$ Raman transition. This is insufficient to resolve the transitions for polarized photon generation.

axis, the second, cavity-assisted branch can emit either σ^- or σ^+ photons as the channels back to the $\left|D_{3/2}, m = -3/2\right\rangle$ and forward to the $\left|D_{3/2}, m = 1/2\right\rangle$ states are both possible. Therefore in order to produce photons of only one polarization in the cavity emission, it is necessary to lift the degeneracy of the $D_{3/2}$ sublevels, with the cavity length resonant with only one of the two allowed branches.

Characterization of the degree of magnetic field splitting attainable with the trap coils described in section 3.4.4 was carried out initially on the $S_{1/2}$ to $D_{3/2}$ Raman transitions. The eight possible transitions are shown in Fig. 5.7(a) and the shifts in their calculated frequencies are shown in Fig. 5.7(b).

Figure 5.8 shows the degree of splitting achieved when 1.5 A of current was passed through the z axis magnetic field coil. The data shows the Raman spectrum recorded while the 397 nm drive laser was held at constant detuning, while the cavity length was scanned. Although the lines are not resolved, a coarse fit with 3 Lorentzian lines shows a shift of approximately ± 20 MHz for the $\left|S_{1/2}, m = \pm 1/2\right\rangle$ to $\left|D_{3/2}, m = \mp 3/2\right\rangle$. With 1.5 A of applied current a field of approximately 10 gauss is expected from the magnetometry results, yielding a shift of 30 MHz, so either there is some shielding, magnetometry uncertainty was underestimated or the coarse fit has not been correctly interpreted. If it is assumed that the estimated 20 MHz shift in the S to D Raman transitions is close to

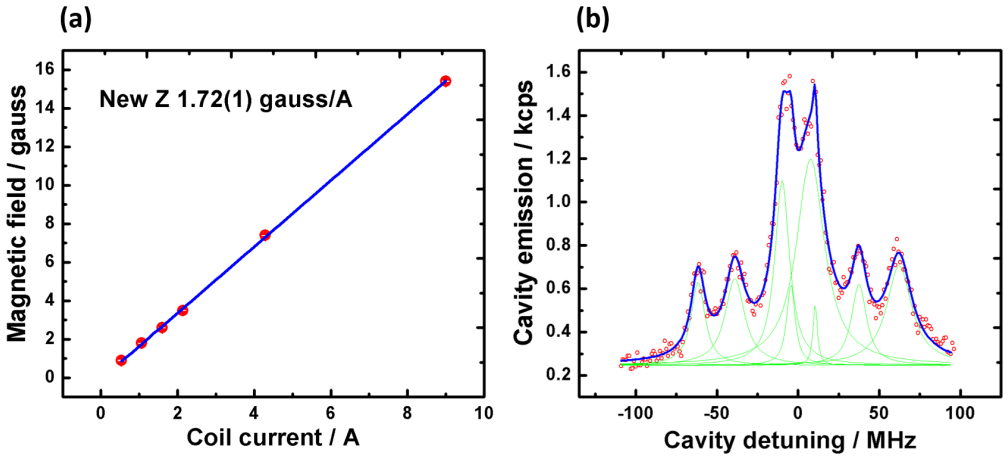

Figure 5.9: (a) Field as function of current for additional z axis coils. Thicker diameter wire was used so the accessible current range is higher than for the old coils. (b) $S_{1/2}$ to $D_{3/2}$ magnetic field splitting with additional coils. The extracted average shifts are 62.1(4), 38(1), 10.1(4) and 6(2) MHz - see text.

the true value, this gives an upper limit to the splitting accessible in the D to D transition in which polarized photons are to be generated, as the shifts per unit of magnetic field in the $\left|S_{1/2}, m = \pm 1/2\right\rangle$ sublevels are over twice that of the $\left|D_{3/2}, m = \pm 1/2\right\rangle$ sublevels. The natural linewidth of the D to D Raman transitions is that set by the rate of spontaneous decay from the $P_{1/2}$ manifold, $\Gamma = 22.4$ MHz, suggesting that the field applied in Fig. 5.8 is insufficient to resolve the $D_{3/2}$ levels in the target Raman transition for generation of polarized photons. Furthermore, the maximum field that could be sustained indefinitely, due to coil heating, was 1 A. Further coils were therefore added to the existing assembly which could generate an additional magnetic field of 15 gauss. The field as a function of current is shown in Fig. 5.9(a).

The new coils were mounted and currents of 9 A and 1 A passed through the new and old coils respectively. The S to D data was retaken, shown in Fig. 5.9(b), with the frequency scale set to zero for the fitted centre of the unbroadened line. Eight Lorentzian distributions were fitted, with initial guesses for the line centres taken from the calculated shifts expected from the applied currents. The 397 nm drive laser was unpolarized so the transition line strengths were not calculated. From the fit, the shifts are 62.1(4), 38(1), 10.1(4) and 6(2) MHz, compared to the calculated values of 62, 39, 17 and 6 MHz for a field of 20 gauss. The measured shift results are the averaged absolute values of the pairs of peaks that are symmetric about the unshifted frequency, and the standard deviation of each pair.

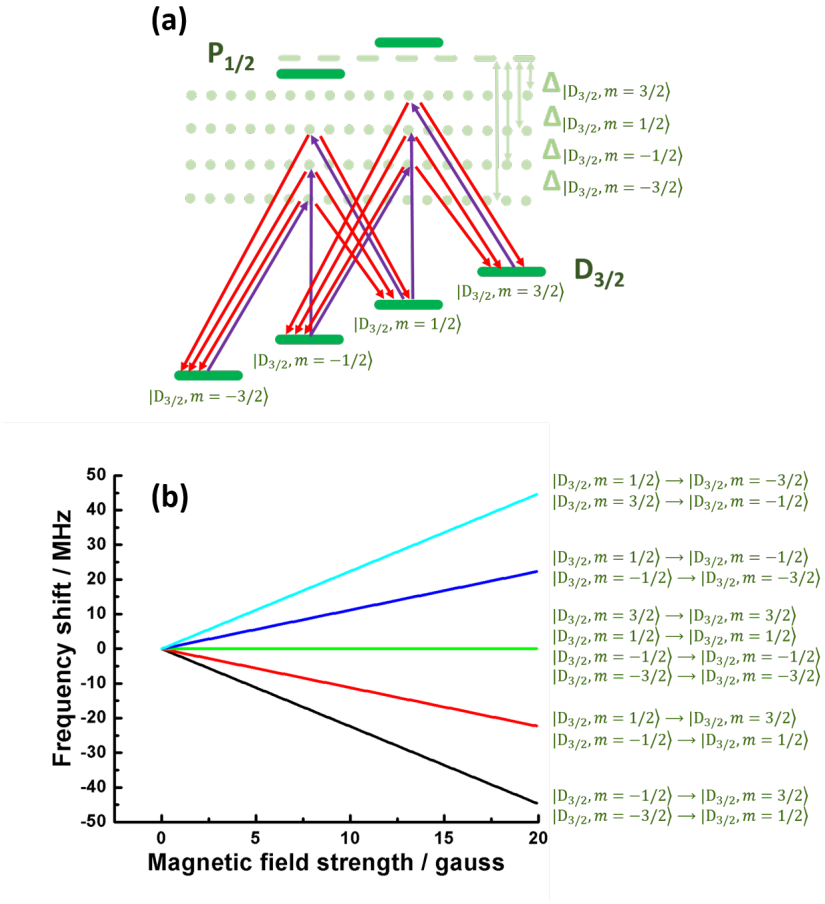

Figure 5.10: (a) Unpolarized cavity-assisted Raman transitions within the $D_{3/2}$ manifold. After preparing a mixture of all the states, a 866 nm laser drives all the allowed transitions. The drive branches are shown in purple for clarity. The detuning of the drive laser for each transition is shown relative to the unshifted $P_{1/2}$ level. (b) Line shifts in Raman transitions in the $D_{3/2}$ as a function of magnetic field strength.

Next, D to D transitions were observed within the the manifold, to confirm that the magnetic splitting was sufficient to resolve the lines. With the quantization axis along the cavity, there are 12 allowed cavity-assisted Raman transitions within the $D_{3/2}$ manifold. They are shown in Fig. 5.10(a). The expected shifts in the transition lines as a function of magnetic field is shown in Fig. 5.10(b). In order to observe these, the ion was first prepared in an arbitrary mixture of all the $D_{3/2}$ sublevels during a period of optimal cooling, after which the repumpers were switched off for a time sufficient for population of the $D_{3/2}$ level. This was followed by a pulse of 866 nm light to drive the Raman transition, and the cavity length scanned with the SPCM gated on the drive pulse. The polarization of the 866 nm laser was set to drive σ^+, σ^- and π transitions. Currents in the old and new coils were 700 mA and 6 A respectively. The results are shown in Fig. 5.11, with

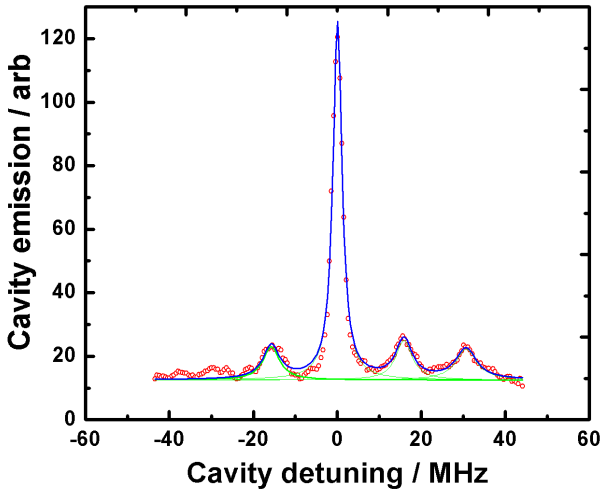

Figure 5.11: Observation of unpolarized cavity-assisted Raman transitions within the $D_{3/2}$ manifold. The old and new coils carried currents of 700 mA and 6 A respectively. A fit for 5 peaks did not converge so the fit is for four Lorentzian peaks with initial guess parameters for the line centers calculated from the measured field strengths for the lines that are clearly visible. The central peak is augmented by photons scattered from the trap electrodes.

four Lorentzian peaks fitted. There is clearly a missing peak, attributed to a bias in the polarization of the drive laser. The peak at zero detuning contains a contribution from the drive laser scattering off the trap electrodes. The linewidths of the other peaks, extracted from the fit, are 4.7(6), 4.8(8) and 6(1) MHz from left to right, and the four peaks have an average separation of 15.4(6) MHz. This ratio of line width to separation is assurance that the target transition will be resolved.

5.1.4 Observation of polarized photons

With the polarization of the (σ^-, π) and (σ^+, π) 866 nm beams respectively optimized for state preparation and driving the cavity-assisted Raman transition, and the Zeeman levels split enough to resolve the transitions by the enhanced magnetic field, a cavity-length scan was performed while the ion was illuminated by the pulse sequence shown in Fig. 5.2. The detector was gated on the drive pulse. The coil currents were 350 mA and 3 A in the old and new coils respectively, and the detuning of the drive laser was 70 MHz. The result is shown in Fig. 5.12. The target transition has a width of 1.8(3) MHz and lies 16.59(7) MHz from the resonant $\left|D_{3/2}, m = -3/2\right\rangle$ to $\left|D_{3/2}, m = -3/2\right\rangle$ transition in which the

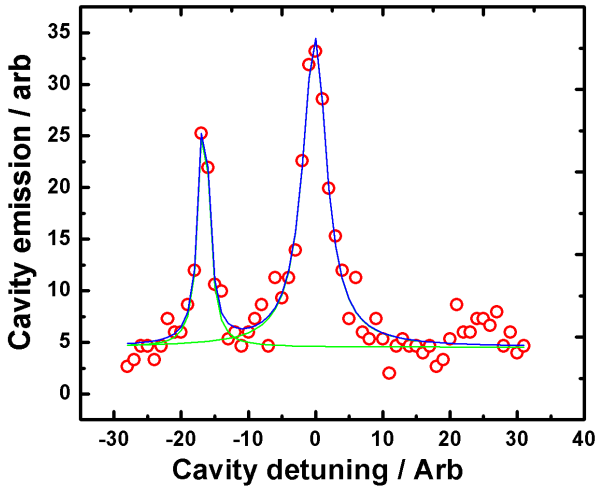

Figure 5.12: $\left|D_{3/2}, m = -3/2\right\rangle$ to $\left|D_{3/2}, m = 1/2\right\rangle$ and $\left|D_{3/2}, m = -3/2\right\rangle$ cavity-assisted Raman transitions. The fit shows the target transition has a width of 1.8(3) MHz and is clearly resolved with a frequency offset of 16.59(7) MHz from the resonant transition. The other three transitions are well suppressed by the fidelity of the prepared state. It is emphasized that there is a single monochromatic laser at the frequency labeled zero detuning, while the peak at -16.59 MHz is due solely to Raman emission into the cavity by the ion.

laser-driven and cavity-assisted branches have the same frequency.

Illuminating the ion with the above pulse sequence while locking the cavity length resonant with the target $\left|D_{3/2}, m = -3/2\right\rangle$ to $\left|D_{3/2}, m = 1/2\right\rangle$ transition generates a stream of σ^- polarized photons in the cavity emission. To observe the purity of polarization of the emission, a polarization analyzer consisting of a quarter and half wave plate and a PBS were inserted in the cavity emission path between the cavity and the detection fiber. The quarter wave plate was pre-aligned to linearize the circular polarization. The half wave plate was then rotated in steps of 10° while the detector was gated on the drive pulse of the Raman transition. The results for a full turn of the half wave plate are shown in Fig. 5.13, along with a measurement of the background. A sinusoid was fitted to the data, and the background was averaged and found to be 24.1(3) cps. This was subtracted from the signal and an extinction ratio of 0.8(1) was calculated. The data was taken with a drive laser Rabi frequency of 25Γ and with a detuning of +30 MHz. The impurity in the polarization is attributed to imperfect alignment of the quarter wave plate and insufficient separation of the $\left|D_{3/2}, m = -3/2\right\rangle$ to $\left|D_{3/2}, m = 1/2\right\rangle$ and $\left|D_{3/2}, m = -3/2\right\rangle$ to

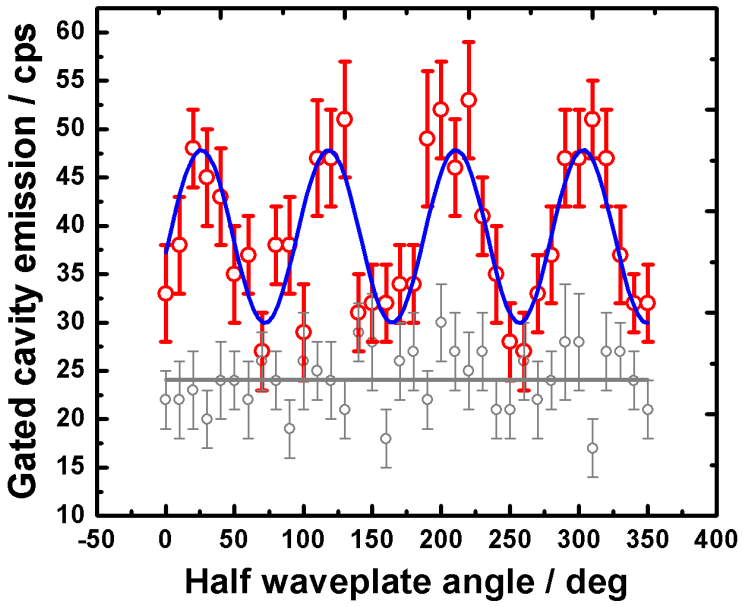

Figure 5.13: Measurement of the polarized cavity emission extinction ratio. A polarization analyser was inserted in the cavity emission detection path, comprised of quarter and half wave plates and a PBS. With the SPCM gated on the drive laser pulse, the cavity emission rate was measured for a full turn of the half wave plate, at 10° intervals. A sinusoidal fit was made to the red data points and the background is shown in grey. The background average is 24.1(3) and after subtracting this from the signal, the extinction ratio is 0.8(1).

$|\mathrm{D}_{3/2}, m = -3/2\rangle$ transitions. To extract the true extinction ratio, several measurements like the one in Fig. 5.13 will be made for different settings of the quarter wave plate and the value extracted from a fit to that data. The polarization purity will be improved with higher detuning to narrow the line widths of the transitions in order to isolate the target transition.

5.2 Toward coherent ion-cavity interaction

Having established the ability to drive a cavity-assisted Raman transition between the $|\mathrm{D}_{1/2}, m = -3/2\rangle$ and $|\mathrm{P}_{1/2}, m = 1/2\rangle$ levels, generating a polarized photon in the cavity through the scheme outlined above, the scene is set for the observation of a coherent ion-cavity interaction in the form of a vacuum Rabi oscillation, in which there is a coherent exchange of energy between the ion and the cavity field. By observing the cavity emission during this experimental detection window, we expect to see an oscillation in the prob-

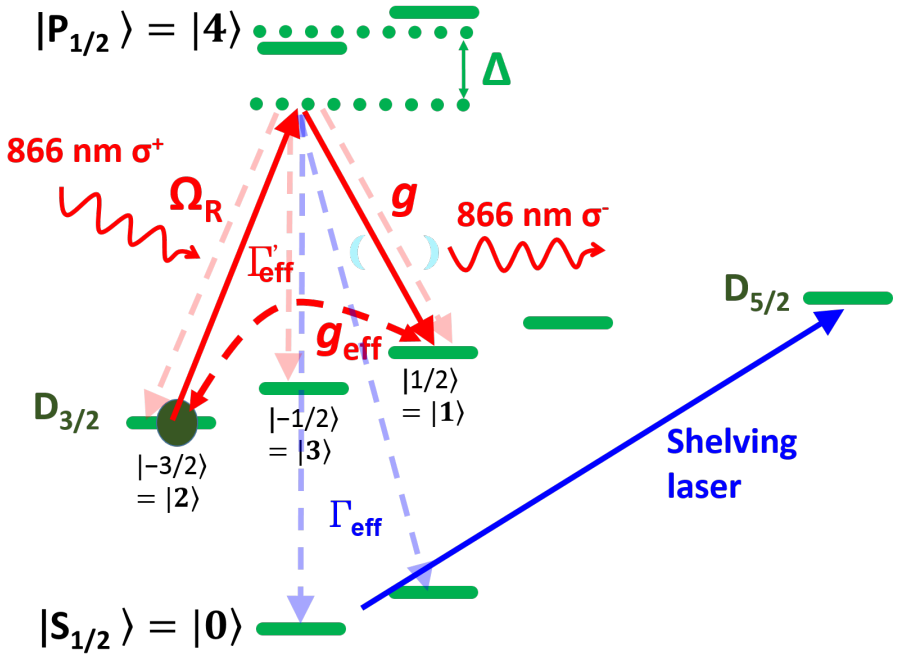

Figure 5.14: Scheme for observing vacuum Rabi oscillations. The dynamics depicted in Fig. 5.1 have been extended to include the spontaneous decay (shown in faint dashes) from the $P_{1/2}$ level to the $S_{1/2}$ level (Γ_{eff}) and the $D_{3/2}$ level (Γ'_{eff}). The action of the shelving laser in coupling the $S_{1/2}$ level to the $D_{5/2}$ level is shown as well as the reversibility of the effective Raman coupling between the $D_{3/2}$ levels. The states relevant to the model are shown and labeled $|0\rangle$, $|1\rangle$, $|2\rangle$, $|3\rangle$ and $|4\rangle$.

ability of detecting a photon proportional to the probability of there being a photon in the cavity. By assigning a timestamp to the arrival of each cavity photon, we may build a histogram in which the oscillation would be apparent. However, in the dynamics of our system the dominant process is the fast decay from the $P_{1/2}$ level to the $S_{1/2}$ ground state, and the signal from this fast decay would hide that of the coherent process. To overcome this we may post-select our data. Upon detection of a photon, we carry out a test to see whether the ion is in the ground state or if it still remains in the $D_{3/2}$ manifold. By discarding the data points when the ion is found to be in the ground state, we restrict ourselves to the subspace of interest, reducing the impact of the fast decay channel on the visibility of the coherent oscillation.

The scheme for post-selecting the data is via a process of electron-shelving to a dark state followed by fluorescent state detection. Immediately after a signal is observed from the cavity, the laser driving the vacuum Rabi oscillation is switched off, and on-resonance light is switched on which couples the $S_{1/2}$ state to the long-lived $D_{5/2}$ level. Then the 397 nm and 866 nm fluorescence lasers are switched on, for which the $D_{5/2}$ level is a dark

state. By contrast the $D_{3/2}$ state is a bright state, so by measuring the fluorescence of the system after the action of the shelving laser, we may infer whether a decay from the $P_{1/2}$ level had taken place, and decide whether to keep that data point. The theoretical model is now presented.

5.2.1 Theoretical model

The theoretical framework presented in this section was developed by Kimmo Luoma (Theoretical Quantum Optics group, Dresden University). Figure 5.14 shows the scheme for observation of the vacuum Rabi oscillation. After the generation of a σ^- photon in the cavity, described in the above section, the photon energy may then oscillate between the cavity and the ion as predicted by the Jaynes-Cummings model. During this process the cavity decays at a rate κ, and effective decay from the $P_{1/2}$ is at a rate Γ_{eff} to the $S_{1/2}$ level and a rate $\alpha_k \Gamma'_{\text{eff}} (k = 1, 2, 3)$ to the three allowed $D_{3/2}$ states where the α_k are the Clebsch-Gordan coefficients for the three transitions. The degeneracy of the $S_{1/2}$ states do not play a role in the dynamics. If there is a decay to the $S_{1/2}$ level, this is detected through fluorescent state detection after a shelving laser couples the $S_{1/2}$ state to the $D_{5/2}$ dark state.

The states $|i\rangle$ are labeled

$$\left|S_{1/2}\right\rangle = |0\rangle\,, \tag{5.4}$$

$$\left|D_{3/2}, m = -1/2\right\rangle = |1\rangle\,, \tag{5.5}$$

$$\left|D_{3/2}, m = 3/2\right\rangle = |2\rangle\,, \tag{5.6}$$

$$\left|D_{3/2}, m = 1/2\right\rangle = |3\rangle\,, \tag{5.7}$$

$$\left|P_{1/2}\right\rangle = |4\rangle\,, \tag{5.8}$$

with the atomic energy levels $E_i = \hbar\omega_i$. The Hamiltonian for the system is written as the sum of the Hamiltonians for the cavity, the ion, and the ion-field interaction between the ion and both the drive laser and the cavity field:

$$H(t) = H_{\text{C}} + H_{\text{I}} + H_{\text{IF}}(t), \tag{5.9}$$

where

$$H_{\text{C}} = \hbar\omega_{\text{C}} a^\dagger a, \tag{5.10}$$

$$H_{\text{I}} = \sum_{i=1}^{4} \hbar\omega_i \sigma_{i,i} \tag{5.11}$$

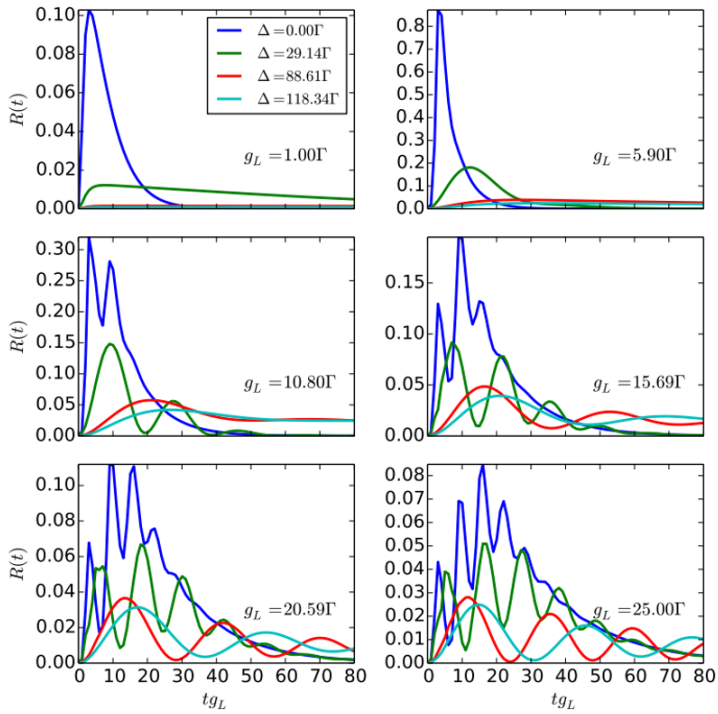

Figure 5.15: Simulated photon flux $R(t)$. The time-resolved flux of cavity emission as measured at the SPCM during the detection window is calculated for a range of drive laser intensities $\Omega_{\mathrm{R}} \in [\Gamma, 25\Gamma]$ and detunings $\Delta \in [0, 118\Gamma]$. In this figure Ω_{R} is written as g_L. As a guide it is noted that $80t_{g_L}$ is equivalent to 50 μs in the top left window and 2 μs in the bottom right window.

and

$$H_{\mathrm{IF}}(t) = \hbar \left(e^{-i(\omega_{\mathrm{L}}+\delta_{\mathrm{L}})t}\Omega_{\mathrm{R}}\sigma_{4,2} + e^{i(\omega_{\mathrm{L}}+\delta_{\mathrm{L}})t}\Omega_{\mathrm{R}}^{*}\sigma_{2,4} + g\sigma_{4,1}a + g^{*}\sigma_{1,4}a^{\dagger} \right). \tag{5.12}$$

Here ω_{L} and Ω_{R} are the drive laser angular and Rabi frequencies respectively, ω_{C} is the cavity field angular frequency, δ_{L} is the detuning between the laser and the cavity, and $\sigma_{i,j} = |i\rangle\langle j|$ are the atomic raising and lowering operators. We choose $\omega_0 = 0$ so that the energies in the system satisfy

$$\omega_4 = \omega_1 + \omega_{\mathrm{C}} + \Delta, \tag{5.13}$$

$$\omega_4 = \omega_2 + \omega_{\mathrm{L}} + \Delta, \tag{5.14}$$

for a Raman detuning Δ from the unshifted $\mathrm{P}_{1/2}$ level. The decay processes which affect the dynamics are the cavity decay κ and the decays from the $\mathrm{P}_{1/2}$ manifold Γ and $\alpha_k\Gamma'$ to the $\mathrm{S}_{1/2}$ and $\mathrm{D}_{1/2}$ levels respectively. After transforming to the interaction representation

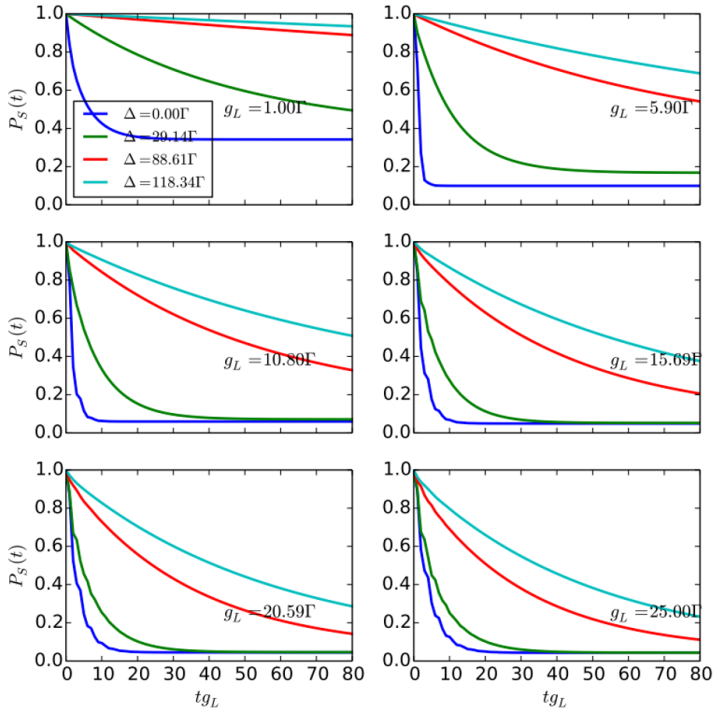

Figure 5.16: Simulated probability of success $P_{\mathrm{S}}(t)$ for the intensities and detunings in Fig. 5.15. The lines correspond to the probability that the ion-cavity system still undergo a coherent interaction before decay to the $\mathrm{S}_{1/2}$ state takes place.

the Hamiltonian is

$$H_{\mathrm{Int}} = \hbar\left(-\Delta\sigma_{1,1} - (\Delta - \delta_{\mathrm{L}})\sigma_{2,2} + \Omega_{\mathrm{R}}\sigma_{4,2} + \Omega_{\mathrm{R}}^{*}\sigma_{2,4} + g\sigma_{4,1}a + g^{*}\sigma_{1,4}a^{\dagger}\right) \tag{5.15}$$

and the dynamics are given by

$$\frac{d}{dt}\rho(t) = -i\left[H_{\mathrm{Int}}, \rho(t)\right] + \frac{\kappa}{2}\mathcal{D}\left[a\right]\rho(t) \tag{5.16}$$

$$+ \frac{\Gamma}{2}\mathcal{D}\left[\sigma_{0,4}\right]\rho(t) \tag{5.17}$$

$$+ \frac{\Gamma'}{2}\left(\alpha_1\mathcal{D}\left[\sigma_{1,4}\right] + \alpha_2\mathcal{D}\left[\sigma_{2,4}\right] + \alpha_3\mathcal{D}\left[\sigma_{3,4}\right]\right)\rho(t) \tag{5.18}$$

with $\mathcal{D}\left[o\right]\rho \equiv 2o\rho o^{\dagger} - \left\{o^{\dagger}o, \rho\right\}$.

The effect of the decay from the $\mathrm{P}_{1/2}$ to the $\mathrm{S}_{1/2}$ level is eliminated by post-selection and is realized by

$$\rho(t) \mapsto \rho_{\mathrm{PS}}(t) \equiv \frac{A\rho(t)A}{\mathrm{tr}\left\{A\rho(t)A\right\}}, \tag{5.19}$$

where $A = \mathrm{I}\otimes\mathrm{I} - |0\rangle\langle 0|\otimes\mathrm{I}$. The spontaneous cavity decay leads to a rate of cavity emission

$$R(t) = \kappa\mathrm{tr}\left\{\mathrm{I}\otimes a^{\dagger}a\rho_{PS}(t)\right\}. \tag{5.20}$$

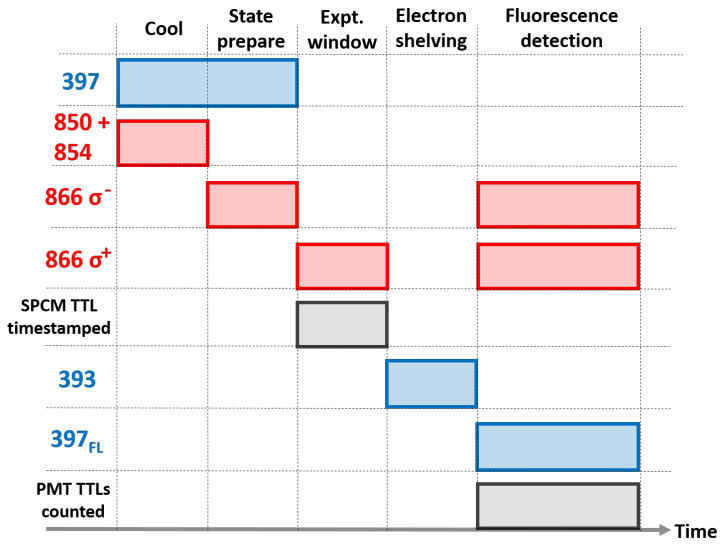

Figure 5.17: FPGA control and detection. Laser pulses during cooling and state preparation sequence, the experimental window, electron shelving and fluorescence detection are shown. The grey regions show when the FPGA takes input from the SPCM during the experimental window and from the PMT during fluorescence detection. The fluorescing 397 nm laser marked 397_{FL} has a different power and detuning to the 397 nm laser responsible for cooling and state preparation.

The effective two-level atom dynamics (TLA) are given by

$$\rho(t)_{\mathrm{TLA}}(t) = \frac{B\rho_{\mathrm{ion}}(t)B}{\mathrm{tr}\left\{B\rho_{\mathrm{ion}}(t)B\right\}}, \tag{5.21}$$

where $B = \sigma_{11} + \sigma_{22}$ and $\rho_{\mathrm{ion}} = \mathrm{tr}_{\mathrm{cav}}\left\{\rho_{\mathrm{PS}}(t)\right\}$.

The dynamics have been simulated for the laser intensity range $\Omega_{\mathrm{R}} \in [\Gamma, 25\Gamma]$ and detuning range $\Delta \in [0, 118\Gamma]$. The laser intensity range corresponds to powers of $[13\mu\mathrm{W}, 65\mu\mathrm{W}]$ after taking into account the proportion of the total beam power in the σ^+ polarization component. The relative laser-cavity detuning δ_L is set to zero. The time-resolved photon flux as detected by the SPCM during the coherent evolution window is calculated, and the results are shown in Fig. 5.15. A further calculation in Fig. 5.16 shows the decreasing probability with time of the ion-cavity system undergoing a coherent interaction before decaying to the ground state.

5.2.2 Experimental realization

The experimental sequence to observe the coherent coupling between the ion and the cavity divides chronologically into three parts. During the state preparation phase the ion is cooled close to the Doppler temperature before being optically pumped into the

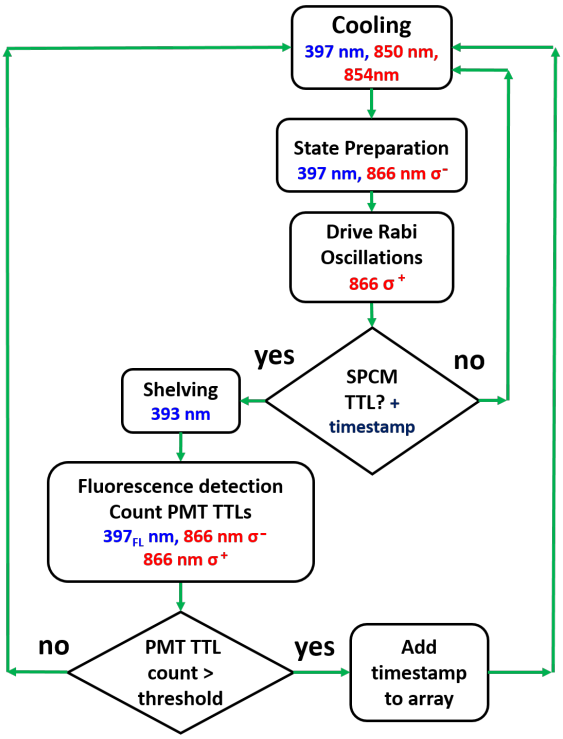

Figure 5.18: FPGA logic. The FPGA makes two which-way choices. The arrival of a TTL pulse from the SPCM while driving the vacuum Rabi oscillations causes the event to be timestamped and held in memory while the driving laser is switched off and the shelving begins, otherwise the sequence resets to the cooling phase. After the shelving phase, TTL pulses from the PMT are counted for some predetermined time. If a number is counted equal to some predetermined threshold, the second condition is met and the timestamp is added to the array of post-selected data, while the sequence resets to the cooling phase.

$|\mathrm{D}_{3/2}, m = -3/2\rangle$ state. After that there is a coherent evolution phase, during which time the laser which drives the vacuum Rabi oscillation is switched on while the cavity emission is observed. Finally there is a state detection phase in which electron shelving to a dark state precedes fluorescent state detection. In order to detect the final state of the ion with certainty, the requirement to gather photon statistics makes this sequence some orders of magnitude longer in time than the others. For this reason it is only carried out if a photon is detected during the experimental window. Therefore some which-way logic is required to be carried out in real time during the measurement.

A field-programmable gate array (FPGA) is used to govern the timing of the laser pulses, while taking two inputs: the TTL pulses produced by the single photon counting module which detects cavity emission; and the TTL pulses produced by the PMT during fluorescent state detection. The FPGA runs source code written by Hiroki Takahashi

(ITCM). The time resolution of the FPGA is 10 ns. If a photon is observed at the cavity output during the experimental window, the FPGA timestamps the event and writes the timestamp to a memory address while shutting off the σ^+ polarized 866 nm drive laser. Electron-shelving is carried out with a 393 nm laser resonant with the $S_{1/2}$ to $P_{3/2}$ transition, from where the ion decays to the dark long-lived $D_{5/2}$ level with 88% probability (see Fig. 3.18 for the $^{40}Ca^+$ energy levels). Finally a 397 nm fluorescent laser is switched on, optimized for maximum fluorescence counts, as well as both of the oppositely polarized 866 nm lasers. During this time the PMT signals are counted. The process for determining the duration of the counting time and photon number threshold is by Poissonian statistical analysis and is described in section 5.2.2. If sufficient photons are counted the ion is deemed to be in a bright state and the timestamp is copied to another address in the FPGA memory. This second memory address is constantly interrogated by a PC and its value recorded each time it changes, so that an array of post-selected timestamps are recorded for binning in a histogram. The computer also records a separate array containing all the timestamps acquired before the post-selection process takes place. Figure 5.17 shows the laser pulse sequence generated by the FPGA as well as the windows during which it takes input. Figure 5.18 shows schematically the real time logic which the FPGA applies.

There are strict practical constraints on the conditions under which the vacuum Rabi oscillations may be observed. Firstly, the wave function of the ion has a thermal spread in the direction of the cavity standing wave, explored in detail in chapter 4, which amounts to a spread in the value of the effective ion-cavity coupling g_{eff}. Each contribution leads to a different value for the frequency at which the vacuum Rabi oscillation takes place, leading to a dephasing over time in the observed signal. Therefore the ion must be as cold as possible to extend the coherence of the signal for as long as possible. Secondly, there must be a high degree of fidelity in the state preparation. Although the Clebsch-Gordan coefficients for the cavity-assisted Raman transitions are the same regardless of the initial state, the difference in detuning from the $P_{1/2}$ level will cause a change in g_{eff} and the effective decay rate Γ_{eff}, both of which change the rate of the coherent oscillation. Thirdly, the post-processing relies critically on the ability to shelve the ion to a dark state and to accurately determine that state through fluorescence detection. Finally, the act of post-processing the data is lengthy, and results in the discarding of large amounts of data. This means that the repetition rate at which the sequence is carried out must be maximized. Work toward realization of these experimental requirements is now discussed.

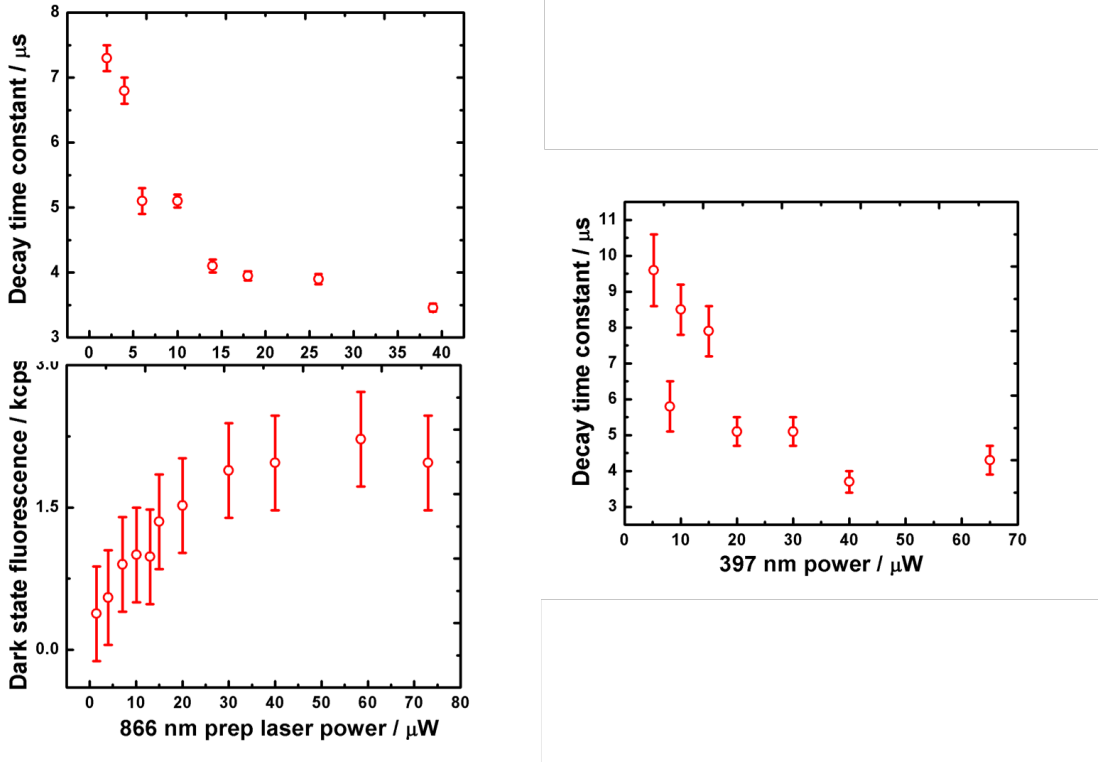

Figure 5.19: Dependence of rate and fidelity of the state preparation on powers in 866 nm state preparation beam and 397 nm cooling beam. Higher laser powers correspond to a shorter time required for state preparation. In the case of the 866 nm laser, there is a clear conflict with the requirement to achieve a high fidelity in the target state. For low 866 nm powers the fidelity is close to unity. The error bars on the decay times are from the fits, and the fluorescence error is the standard deviation in the fluorescence over the timescale of the measurement.

Optimization of the cooling and state preparation sequence

Time resolved PMT fluorescence traces were recorded while cooling and state preparing the ion, similar to the one in Fig. 5.5(a). Exponential decays were fitted and both the time constant and steady state fluorescence while in the dark state were extracted for various powers in both the 866 nm state preparation laser and the 397 nm cooling laser. Figure 5.19 shows the results of the fits. The scattering rate of the ion increases with the power in the 397 nm cooling laser, driving the state preparation faster for higher powers, as is the case for the power in the 866 nm laser. However, saturating these transitions conflicts with other requirements. The figure shows the steady state fluorescence of the final dark state as the 866 nm power is increased. This rises drastically and is attributed to impurities in the polarization of the 866 nm state preparation laser, with the undesirable circular

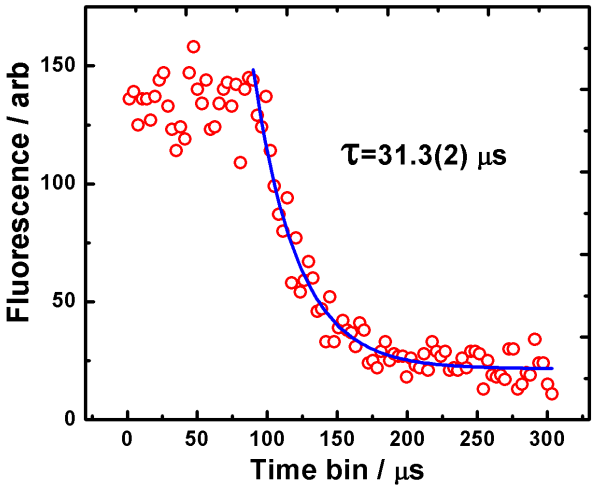

Figure 5.20: Time-resolved fluorescence during cooling and state preparation with the final experimental parameters for 397 nm and 866 nm laser powers. It is necessary to cool for 100 μs and prepare the state for another 200 μs.

component repumping the cooling transition. The power in the 397 nm cooling laser is constrained by the requirement to minimize the temperature of the ion before the start of the experimental measurement window during which the oscillations in cavity signal are to be observed. The ion temperature was probed at the end of the state preparation sequence (as measured through visibility scans like those described in chapter 4) by gating the SPCM over the last 10% of the state preparation sequence. It was found that the visibility of the cavity standing wave structure was entirely washed out when the cooling laser was operating at high powers. Therefore the state preparation was executed with the same power in the 397 nm laser as that required by efficient cooling to close to the Doppler limit. The period of state preparation had to be extended in order to get a high degree of fidelity with the target state. Fig. 5.20 shows the time-resolved fluorescence during the 100 μs of cooling and 200 μs of state preparation which was required to simultaneously fulfill the requirements to prepare the state with a high fidelity and maintain a low temperature of the ion at the beginning of the experimental window. The powers are 1 μW and 150 nW in the 866 nm and 397 nm lasers respectively. A visibility measurement showed that the temperature of the ion was around twice the Doppler limit at the end of this sequence. This high temperature is attributed to the shifts in the Zeeman levels due to the magnetic field. With 15 gauss of applied field, the shift in the $\left|\mathrm{S}_{1/2}, m = 1/2\right\rangle$ to $\left|\mathrm{P}_{1/2}, m = -1/2\right\rangle$ transition is 28 MHz and it was found empirically that the best ion temperature was

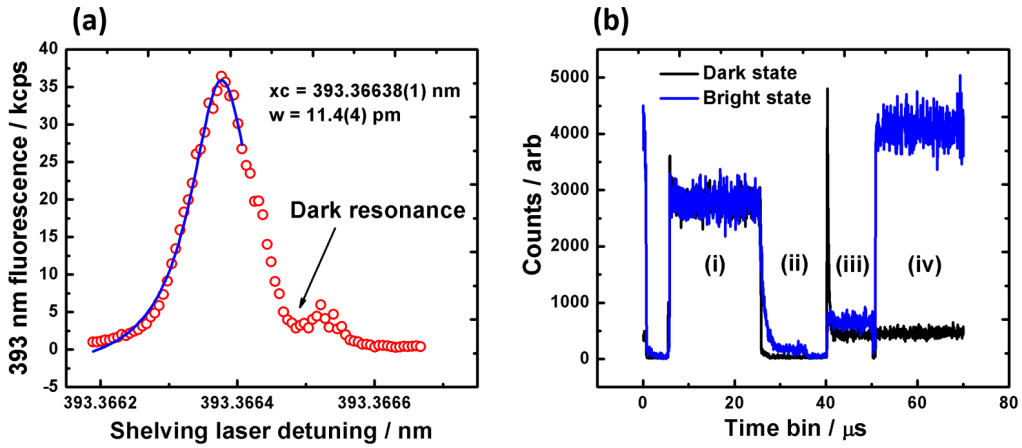

Figure 5.21: (a) Coarse spectroscopy of the 393 nm transition. The shoulder on the low frequency side is due to coherent population trapping in the 3-level system coupled by the 393 and the 854 nm lasers, resulting in a dip in the main line. The fitting range is chosen to attempt to minimize the effect of this distortion. The line centre and width are shown. (b) Contrast in bright and dark fluorescent states after shelving. After cooling (i) and preparing the ion in the $S_{1/2}$ state (ii), the 393 nm laser shelves it (iii) to the dark $D_{5/2}$ state (black). Preparation of the ion in the $D_{3/2}$ state makes it transparent to the 393 nm beam, and the ion fluoresces (iv) during state detection (blue). During the dark state preparation sequence the 393 nm scatter during shelving is clearly visible.

attained with a detuning of 25 MHz from the line centre.

State detection sequence

If the condition is met that the FPGA detects a TTL pulse from the SPCM during the experimental window, the σ^+ drive laser is shut off and the state detection sequence begins, consisting of electron shelving followed by fluorescent state detection.

Shelving the ion to a dark state would ideally be carried out using a 729 nm laser to directly couple the ground state to the dark $D_{5/2}$ manifold. However this forbidden transition is so narrow that a highly sophisticated apparatus is required to lock a laser to resonance. While this is currently under development in the lab it was not ready at the time these experiments were carried out. Therefore a 393 nm laser resonant with the $S_{1/2}$ to $P_{3/2}$ transition was used to indirectly couple the ground state to the target dark state. Decay from the $P_{3/2}$ level is predominantly to the $D_{5/2}$ level, with a branching ratio of approximately 9:1 with the $D_{3/2}$ level. The use of the 393 nm laser is a significant compromise, as the 12% decay channel to the $D_{3/2}$ level gives a false positive in the state

detection, and 12% of all the SPCM counts detected during the experimental window erroneously enter the post-selected dataset.

In order to lock the 393 nm laser on resonance, the precision spectroscopy technique routinely used to probe the dipole-allowed cooling transition (see section 3.4.2) was adapted to carry out spectroscopy on the 393 nm transition. The 397 nm probing pulse was replaced with a 393 nm pulse, and the grating angle on the ECDL was scanned over resonance to give the line shape in Fig. 5.21(a). There is a feature which has been confirmed to be a result of coherent population trapping due to the coupling of the $D_{5/2}$ and $S_{1/2}$ levels by the 854 nm and 393 nm lasers. The fitting range was chosen to minimize the distortion due to the dip created by the dark resonance, and the fit extracted a line centre of 393.36638(1) nm in air and a width of 213.6(8) MHz at a power of approximately 70 μW. The line width is well above the 60 MHz accuracy of the wavemeter lock. The 393 nm beam is overlapped in the same fiber as the 397 nm cooling beam.

In order to observe the effect of the shelving laser, a sequence of laser pulses prepared the ion either in the $S_{1/2}$ level or in the $D_{3/2}$ level followed by illumination with the 393 nm laser before finally switching on the 397 nm and and an unpolarized 866 nm laser to generate state-dependent fluorescence. The state preparation was achieved by optimally cooling with the 397nm cooling laser while repumping with the 850 and 854 nm lasers, before switching off either the cooling laser or the repumpers. In the case of preparing the $D_{3/2}$ state, the ion is transparent to the shelving laser and fluoresces in the presence of the 397 and 866 nm beams. In the case of preparing the $S_{1/2}$ state, the effect of the 393 nm laser is to shelve the ion to the dark $D_{5/2}$ level indirectly via the $P_{3/2}$ level. The result is a suppression of the fluorescence during the last portion of the sequence. The two cases are shown in the time-resolved fluorescence in Fig. 5.21(b). Here, the ion was cooled for 20 μs, the initial state prepared for 10 μs, then a pause with no lasers for 5 μs, the 393 nm laser was switched on for 10 μs and fluorescence is observed for 20 μs. The suppressed fluorescence of the dark state follows a sharp spike in PMT counts as the ion initially in the $S_{1/2}$ state scatters 393 nm light. By contrast there is no apparent signal due to the 393 nm beam before the bright fluorescence.

The final part of the experimental sequence is fluorescent state detection, in which it must be established whether the ion is in a bright or dark state. In order to precisely determine whether the ion is in the bright $D_{3/2}$ or dark $D_{5/2}$ state in as short a time as possible, a statistical analysis of the distribution of the arrival times of the fluorescence photons was carried out. A trace such as the one in Fig. 5.21(b) is made from a histogram

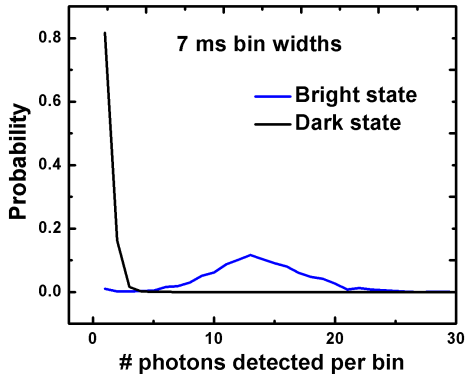

Figure 5.22: Bright and dark state photon statistics. Probability distribution functions are shown for a bin width of 7 ms, calculated from fluorescence data like that in Fig. 5.21(b).

of trigger-correlated timestamps. The timestamps which make up the portion of the sequence which contains the state-dependent fluorescence are extracted and concatenated. This was done separately for the bright and dark state fluorescence generated by lasers with the same power and detuning parameters which would be used during state detection in the experiment. Both arrays of chronologically ordered arrival times were binned with some bin width on the order of milliseconds, and the number of photon events in each bin was counted. A probability distribution function was extracted for the number of photon arrivals per bin for each of the bright and dark states. In this way, the distributions of each could be compared for different lengths of time-bin, in order to minimize the bin width while still clearly resolving the distributions for a bright and dark state. The results of this procedure is displayed in Fig. 5.22 for the bright and dark states in Fig. 5.21(b), with a bin width of 7 ms. The distributions are clearly resolved, with a photon count threshold of 4 during a counting period of 7 ms to maximally distinguish the bright state from the dark.

With the state preparation and state detection sequences characterized, the drive laser rise time was recorded with respect to the signal from the FPGA, both with a fast photodiode measuring the laser intensity before the beam enters the trap chamber, and by scattering the laser light off the trap electrodes and using the counting card to time-resolve the cavity signal due to the scatter. This is shown in Fig. 5.23.

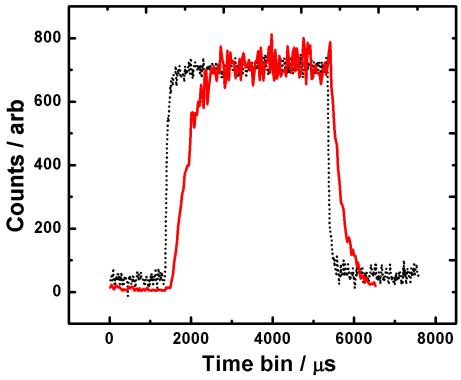

Figure 5.23: Laser rise time with respect to cavity signal. Pulses of 866 nm light measured before entering the trap chamber on a fast photodiode (black dashed) compared with the same pulse observed in the time-resolved SPCM signal as the beam is scattered off the trap electrodes (red).

5.2.3 Preliminary results

Fig. 5.24 shows the results of running the experiment for 115 minutes. The FPGA was programmed with the following sequence. The ion was cooled for 100 μs and state preparation was done for 200 μs. The experimental window was 4 μs. If a cavity photon was observed by the FPGA during this time, the post-selection sequence was initiated during which the shelving laser was on for 6 μs followed by 7 ms of fluorescent state detection. The time-resolved cavity signal in Fig. 5.24 has an offset of +500 ns due to an artifact in the way the PC extracted the data from the FPGA, and the drive laser has a switch-on delay of approximately 730 ns.

The power in the drive laser was 220 μW, corresponding to a Rabi frequency of 38 Γ and the detuning was 150 MHz.

Discussion of preliminary results

With the power and detuning in the drive laser which are quoted above, the theoretical model predicts three periods of oscillation in the first 1000 ns of the dynamics, which are clearly not reflected in the data. Other powers and detunings were tried, and the timescales of the rise and fall in the curves were extended with less power and more detuning, and vice versa, but without the expected oscillation in the probability of the photon arrival times.

The temperature of the ion is a source of dephasing, due to the spread in the value of

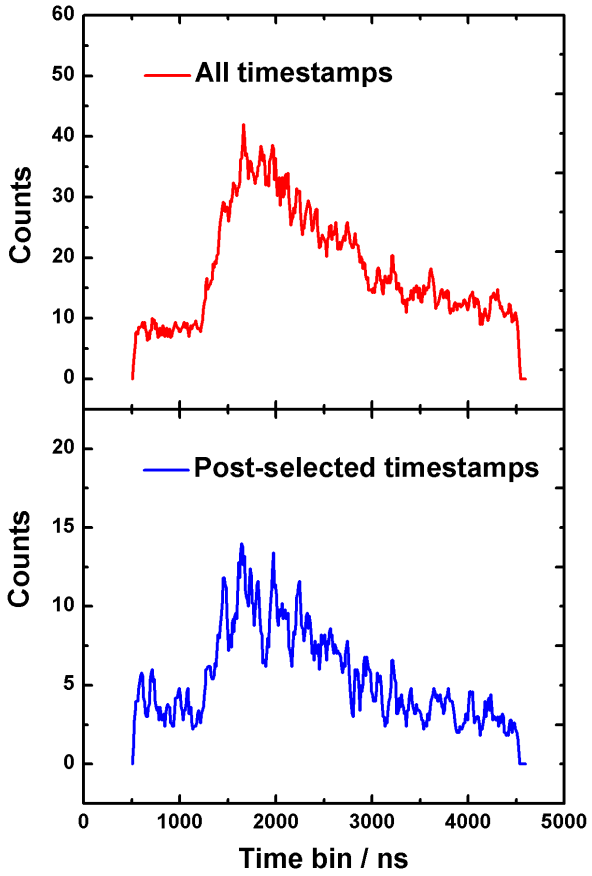

Figure 5.24: Comparison of data sets. (a) shows the binned arrival times of all the cavity emission events detected during the experimental window, (b) shows those data which were chosen during post-selection. An independent measurement shows that the laser switches on at approximately 1230 ns.

g_{eff}. The effect of the dephasing is shown in Fig. 5.25 for an ion temperature of 1, 2 and 3 T_{D}, with any oscillation strongly suppressed after 2 microseconds. The temperature of the ion at the start of the experimental window was estimated to be approximately 2 T_{D}.

Cavity spectroscopy was done on the 866 nm drive laser, and it was found to have a linewidth of approximately 1 MHz with a strong Gaussian contribution. This is attributed to the scanning cavity lock. The theoretical model outlined in section 5.2.1 assumes that the linewidth of the laser is negligible, so a broad laser line will introduce a significant extra damping into the dynamics.

No measurements have been made of the fluctuations in magnetic field at the position of the ion in the cavity, and if present, they would constitute another source of dephasing

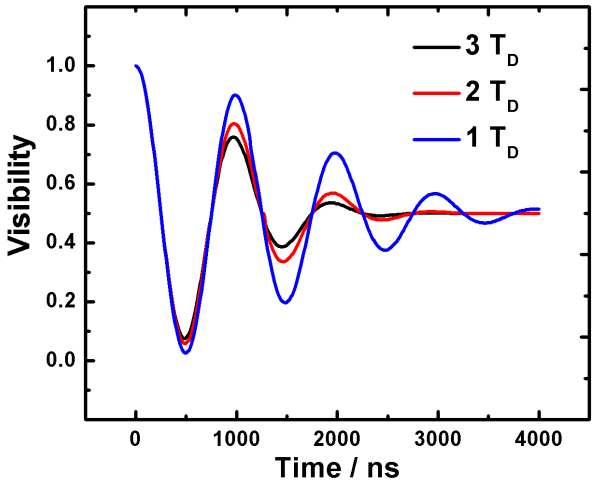

Figure 5.25: Effect of ion temperature on visibility of signal. Dephasing of the coherent oscillation is calculated for 1, 2 and 3 T_{D}, where T_{D} is the Doppler cooling limit.

in the system.

The post-selection of the data relies on shelving population to the $\mathrm{D}_{5/2}$ level. A 729 nm laser was intended to couple the $\mathrm{S}_{1/2}$ ground state directly to this dark state, but was not ready in time for the measurements in this thesis. Therefore the 393 nm laser was used to indirectly couple the two states via the $\mathrm{P}_{3/2}$ excited level, which has a 12% decay to the fluorescent $\mathrm{D}_{3/2}$ level, introducing false positives into the post-selected data. While the power and detuning in the drive laser were chosen to limit the probability of decay from the $\mathrm{P}_{1/2}$ during the measurement window, the decay probability is approximately 2/3 after the first microsecond and more than 5/6 after 2 μs. This flaw in the post-selection scheme introduces 24% noise from the $\mathrm{P}_{1/2}$ decay after 1 μs and nearly 60% after 2 μs.

5.3 Conclusions and outlook

The experiment detailed in the first part of this chapter takes the setup closer toward the goal of creating ion-ion entanglement by initializing a single ion in a Zeeman level of the $\mathrm{D}_{3/2}$ manifold and driving a specific cavity-assisted Raman transition to another state. The polarization purity of the cavity emission shows that the initial state preparation and final state addressing are both achieved with high fidelity. The scene is therefore set for carrying out a similar sequence with two ions simultaneously coupled: the addition of a STIRAP pulse to transfer the initialized population from $\left|\mathrm{D}_{3/2}, m = -3/2\right\rangle$ to $\left|\mathrm{D}_{3/2}, m = 1/2\right\rangle$ will be sufficient to attempt the entanglement scheme presented in Fig. 2.12 in chapter 2.

Although we have failed to observe the vacuum Rabi oscillations in our system, significant work has been achieved toward this goal, including a state-detection protocol for post-selecting the data, and the FPGA-mediated logic required to implement it.

While the individual components of the scheme have been assembled and characterized, it is probable that several elements have combined to put the observation of coherent ion-cavity coupling out of reach. Further work needs to be done on the cooling scheme, so that the ion temperature can be made as low as possible despite the considerable splitting of the cooling transition and the requirement to carry out state preparation immediately before the experimental window. The temperature was estimated through measurements of the visibility of the cavity standing wave with the cavity emission detection gated on the last portion of the state preparation sequence. An improvement on this estimate will come from carrying out the visibility measurement using the polarized photons produced during the experimental window itself. The linewidth of the scanning cavity lock is higher than its fundamental limit, and will be improved. The magnetic field stability will be characterized, and mumetal shielding or an active feedback system will be installed if stability is shown to limit the coherence. Finally, the 729 nm laser will soon be ready which will directly shelve the population during state detection, eliminating the source of false positives in the post-selected data.

Once these experimental issues have been addressed, the setup will act as a platform for testing theoretical predictions in the field of non-Markovian behaviour in quantum systems.

Chapter 6

Summary and conclusions

Before the work presented in this thesis began, a CQED setup consisting of an ion trap with integrated cavity mirrors had be constructed, and a proof-of-principle demonstration of ion-cavity coupling had been carried out. The purpose of the apparatus is to entangle pairs of ions, and to further entangle the pairs to form cluster states for measurement-based quantum computation. This thesis details two experiments that have been performed which bring our setup closer to the point where ion-ion entanglement and cluster state generation will be possible.

In the first experiment, up to five ions have been deterministically and simultaneously coupled to the cavity, and the degree of coupling thoroughly characterized. Previous work by other groups has focused on cavity-coupling either single ions [4], pairs of ions [17] or large ensembles [26]. While coupling several ions to the cavity, the application of a theoretical model to visibility measurements provided a rigorous framework within which to quantify the degree of individual coupling of each ion. It was found that four and five ions could be simultaneously coupled with an average coupling strength of $0.988g_0$ and $0.983g_0$ respectively, where g_0 is the theoretical maximum coupling strength achievable when all the emitters are ideally positioned at cavity antinodes. In terms of the ultimate goals of our scheme, it realizes a critical requirement for efficient cluster state generation, namely the precise localization of several ions simultaneously close to anti-nodal positions in the cavity mode. More generally, this result is highly satisfactory in the context of few-qubit CQED systems for exploring many-body entanglement.

In the second experiment, it has been demonstrated that an ion could be initialized in a specific Zeeman state and then coherently transferred to another with a high degree of fidelity, satisfying a second important requirement in our scheme for ion-ion entanglement. This has been achieved by state preparation through optical pumping, and coherent trans-

fer of population to another target state through a cavity-assisted Raman transition. An initial lower limit on the polarization purity of 80% has been established, paving the way to employ the process for entanglement of two ions. Similar initialization and transfer has previously been achieved by one other group [17] in the context of trapped-ion CQED, and led to a successful demonstration of ion-ion entanglement. Our ability to initialize the ion in one state and coherently transfer it to another, coupled with the work done on multi-ion cavity-coupling described above, brings the setup closer to the realization of many-ion cluster states.

In addition, work has begun on a project in which post-selection of data will reveal vacuum Rabi oscillations in the ion-cavity system. Although the oscillations have not yet been observed above the noise in the system, a point has been reached where all of the apparatus and protocols for the scheme are in place, and areas of the setup which require further characterization and optimization have been identified. When ready, the ion-cavity system will provide a platform for the study of non-Markovian quantum dynamics.

Bibliography

[1] P. W. Shor, "Polynomial-time algorithms for prime factorization and discrete logarithms on a quantum computer," *SIAM Review*, vol. 41, no. 2, pp. 303–332, 1999. Cited on 1

[2] R. Blatt and C. F. Roos, "Quantum simulations with trapped ions," *Nature Physics*, vol. 8, no. 4, pp. 277–284, 2012. Cited on 1

[3] R. Miller, T. E. Northup, K. M. Birnbaum, A. Boca, A. D. Boozer, and H. J. Kimble, "Trapped atoms in cavity QED: coupling quantized light and matter," *Journal of Physics B: Atomic, Molecular and Optical Physics*, vol. 38, no. 9, pp. S551–S565, 2005. Cited on 1

[4] M. Keller, B. Lange, K. Hayasaka, W. Lange, and H. Walther, "Continuous generation of single photons with controlled waveform in an ion-trap cavity system," *Nature*, vol. 431, no. 13, pp. 1075–1078, 2004. Cited on 1, 2, 61, 121

[5] T. Yoshie, A. Scherer, J. Hendrickson, G. Khitrova, H. M. Gibbs, G. Rupper, C. Ell, O. B. Shchekin, and D. G. Deppe, "Vacuum rabi splitting with a single quantum dot in a photonic crystal nanocavity," *Nature*, vol. 432, no. November, pp. 9–12, 2004. Cited on 1

[6] Y. Colombe, T. Steinmetz, G. Dubois, F. Linke, D. Hunger, and J. Reichel, "Strong atom-field coupling for Bose-Einstein condensates in an optical cavity on a chip.," *Nature*, vol. 450, no. 7167, pp. 272–6, 2007. Cited on 1

[7] A. Faraon, C. Santori, Z. Huang, V. M. Acosta, and R. G. Beausoleil, "Coupling of nitrogen-vacancy centers to photonic crystal cavities in monocrystalline diamond," *Physical Review Letters*, vol. 109, no. 3, p. 033604, 2012. Cited on 1

[8] D. P. DiVincenzo, "The physical implementation of quantum computation," *arXiv:quant-ph/0002077*, 2000. Cited on 1

[9] H. J. Kimble, "The quantum internet," *Nature*, vol. 453, no. 7198, pp. 1023–30, 2008. Cited on 1

[10] J. Raimond, M. Brune, and S. Haroche, "Manipulating quantum entanglement with atoms and photons in a cavity," *Reviews of Modern Physics*, vol. 73, no. July, p. 565, 2001. Cited on 1

[11] T. Wilk, S. C. Webster, A. Kuhn, and G. Rempe, "Single-atom single-photon quantum interface.," *Science*, vol. 317, no. 5837, pp. 488–90, 2007. Cited on 1

[12] S. Ritter, C. Nölleke, C. Hahn, A. Reiserer, A. Neuzner, M. Uphoff, M. Mücke, E. Figueroa, J. Bochmann, and G. Rempe, "An elementary quantum network of single atoms in optical cavities," *Nature*, vol. 484, no. 7393, p. 195200, 2012. Cited on 1

[13] A. Stute, B. Casabone, B. Brandstätter, K. Friebe, T. E. Northup, and R. Blatt, "Quantum-state transfer from an ion to a photon.," *Nature Photonics*, vol. 7, no. 3, pp. 219–222, 2013. Cited on 1

[14] C. J. Ballance, T. P. Harty, N. M. Linke, M. A. Sepiol, and D. M. Lucas, "High-fidelity quantum logic gates using trapped-ion hyperfine qubits," *Phys. Rev. Lett.*, vol. 117, p. 060504, Aug 2016. Cited on 1

[15] T. Monz, P. Schindler, J. T. Barreiro, M. Chwalla, D. Nigg, W. A. Coish, M. Harlander, W. Hänsel, M. Hennrich, and R. Blatt, "14-qubit entanglement: Creation and coherence," *Physical Review Letters*, vol. 106, no. 13, p. 130506, 2011. Cited on 1

[16] A. Stute, B. Casabone, P. Schindler, T. Monz, P. O. Schmidt, B. Brandstätter, N. T. E., and R. Blatt, "Tunable ionphoton entanglement in an optical cavity," *Nature*, vol. 485, no. 7399, p. 482485, 2012. Cited on 2

[17] B. Casabone, A. Stute, K. Friebe, B. Brandstätter, K. Schüppert, R. Blatt, and T. E. Northup, "Heralded Entanglement of Two Ions in an Optical Cavity," *Physical Review Letters*, vol. 111, no. 10, p. 100505, 2013. Cited on 2, 4, 27, 29, 121, 122

[18] L.-M. Duan and H. J. Kimble, "Efficient engineering of multiatom entanglement through single-photon detections," *Phys. Rev. Lett.*, vol. 90, p. 253601, Jun 2003. Cited on 2, 27

[19] G. R. Guthöhrlein, M. Keller, K. Hayasaka, W. Lange, and H. Walther, "A single ion as a nanoscopic probe of an optical field," *Nature*, vol. 414, no. 6859, pp. 49–51, 2001. Cited on 2

[20] M. Keller, B. Lange, K. Hayasaka, W. Lange, and H. Walther, "Stable long-term coupling of a single ion to a cavity mode," *Journal of Modern Optics*, vol. 54, no. 11, pp. 1607–1617, 2007. Cited on 2, 25

[21] M. A. Nielsen, "Cluster-state quantum computation," *Reports on Mathematical Physics*, vol. 57, no. 1, pp. 147 – 161, 2006. Cited on 3

[22] G. Vallone, G. Donati, N. Bruno, A. Chiuri, and P. Mataloni, "Experimental realization of the deutsch-jozsa algorithm with a six-qubit cluster state," *Physical Review A*, vol. 81, no. 5, p. 050302, 2010. Cited on 3

[23] A. S. Sørensen and K. Mølmer, "Measurement induced entanglement and quantum computation with atoms in optical cavities," *Phys. Rev. Lett.*, vol. 91, p. 097905, Aug 2003. Cited on 3

[24] J. T. Barreiro, M. Müller, P. Schindler, D. Nigg, T. Monz, M. Chwalla, M. Hennrich, C. F. Roos, P. Zoller, and R. Blatt, "An open-system quantum simulator with trapped ions," *Nature*, vol. 410, no. 7335, p. 486491, 2011. Cited on 3

[25] N. R. Seymour-Smith, "Ion-trap cavity qed system for probabilistic entanglement," *PhD thesis - Unversity of Sussex*, 2011. Cited on 3, 8, 34, 36, 41, 42, 55, 57, 58, 59

[26] P. F. Herskind, A. Dantan, J. P. Marler, M. Albert, and M. Drewsen, "Realization of collective strong coupling with ion Coulomb crystals in an optical cavity," *Nature Physics*, vol. 5, no. 7, pp. 494–498, 2009. Cited on 4, 35, 121

[27] R. McConnell, H. Zhang, J. Hu, S. Ćuk, and V. Vuletić, "Entanglement with negative Wigner function of almost 3,000 atoms heralded by one photon," *Nature*, vol. 519, no. 7544, pp. 439–442, 2015. Cited on 4

[28] R. Dicke, "Coherence in spontaneous radiation processes," *Physical Review*, vol. 93, no. 1, p. 99, 1954. Cited on 4

[29] R. Reimann, W. Alt, T. Kampschulte, T. Macha, L. Ratschbacher, N. Thau, S. Yoon, and D. Meschede, "Cavity-Modified Collective Rayleigh Scattering of Two Atoms," *Physical Review Letters*, vol. 114, no. 2, p. 023601, 2015. Cited on 4

[30] B. Casabone, K. Friebe, B. Brandstätter, K. Schüppert, R. Blatt, and T. E. Northup, "Enhanced Quantum Interface with Collective Ion-Cavity Coupling," *Physical Review Letters*, vol. 114, no. January, p. 023602, 2015. Cited on 4

[31] S. Morrison and A. S. Parkins, "Dynamical quantum phase transitions in the dissipative Lipkin-Meshkov-Glick model with proposed realization in optical cavity QED," *Physical Review Letters*, vol. 100, no. 4, p. 040403, 2008. Cited on 4

[32] S. Gopalakrishnan, B. L. Lev, and P. M. Goldbart, "Frustration and Glassiness in Spin Models with Cavity-Mediated Interactions," *Physical Review Letters*, vol. 107, no. 27, p. 277201, 2011. Cited on 4

[33] T. Pellizzari, S. Gardiner, J. Cirac, and P. Zoller, "Decoherence, continuous observation, and quantum computing: A cavity QED model," *Physical Review Letters*, vol. 75, no. 21, pp. 3788–3791, 1995. Cited on 4

[34] S.-B. Zheng, "Unconventional geometric quantum phase gates with a cavity QED system," *Physical Review A*, vol. 70, no. April, p. 052320, 2004. Cited on 4

[35] S. Fernández-Vidal, S. Zippilli, and G. Morigi, "Nonlinear optics with two trapped atoms," *Physical Review A*, vol. 76, no. 5, pp. 53810–53829, 2007. Cited on 4

[36] H. Habibian, S. Zippilli, and G. Morigi, "Quantum light by atomic arrays in optical resonators," *Physical Review A*, vol. 84, no. 3, p. 033829, 2011. Cited on 4

[37] A. González-Tudela and D. Porras, "Mesoscopic Entanglement Induced by Spontaneous Emission in Solid-State Quantum Optics," *Physical Review Letters*, vol. 110, no. 8, p. 080502, 2013. Cited on 4

[38] E. G. Dalla Torre, J. Otterbach, E. Demler, V. Vuletic, and M. D. Lukin, "Dissipative preparation of spin squeezed atomic ensembles in a steady state," *Physical Review Letters*, vol. 110, no. 12, p. 120402, 2013. Cited on 4

[39] P. Ghosh, *Ion Traps*. Oxford University Press, 1995. Cited on 7

[40] D. Berkeland, J. Miller, J. Bergquist, W. Itano, and D. Wineland, "Minimization of ion micromotion in a paul trap," *Journal of applied physics*, vol. 83, no. 10, pp. 5025–5033, 1998. Cited on 8

[41] M. Raizen, J. Gilligan, J. Bergquist, W. Itano, and D. Wineland, "Linear trap for high-accuracy spectroscopy of stored ions," *Journal of Modern Optics*, vol. 39, no. 2, pp. 233–242, 1992. Cited on 8

[42] K. Sheridan, "Experimental techniques for cold chemistry and molecular spectroscopy in an ion trap," *PhD thesis - Unversity of Sussex*, 2012. Cited on 10, 11, 20, 22, 23, 36, 62, 63

[43] J. Weiner and P. Ho, *Light-Matter Interaction Volume 1*. Wiley, 2003. Cited on 12

[44] A. A. S. Gardner, "Experiments toward high resolution spectroscopy of N_2^+," *PhD thesis - Unversity of Sussex*, 2016. Cited on 17, 62

[45] C. J. Foot, *Atomic Physics*. Oxford University Press, 2004. Cited on 19

[46] M. Fox, *Quantum Optics*. Oxford University Press, 2006. Cited on 24

[47] M. Keller, B. Lange, K. Hayasaka, W. Lange, and H. Walther, "A calcium ion in a cavity as a controlled single-photon source," *New Journal of Physics*, vol. 6, no. 1, p. 95, 2004. Cited on 25

[48] G. S. Vasilev, A. Kuhn, and N. V. Vitanov, "Optimum pulse shapes for stimulated raman adiabatic passage," *Phys. Rev. A*, vol. 80, p. 013417, Jul 2009. Cited on 30

[49] H. C. Nägerl, "Ion strings for quantum computation," *PhD thesis - University of Innsbruck*, 2014. Cited on 35

[50] A. Stute, B. Casabone, B. Brandstätter, D. Habicher, H. G. Barros, P. O. Schmidt, T. E. Northup, and R. Blatt, "Toward an ion–photon quantum interface in an optical cavity," *Applied Physics B*, vol. 107, no. 4, pp. 1145–1157, 2012. Cited on 39

[51] S. P. Begley, "Optimisation of the coupling of ion strings to an optical cavity," *PhD thesis - University of Sussex*, 2015. Cited on 65, 78

[52] D. J. Berkeland and M. G. Boshier, "Destabilization of dark states and optical spectroscopy in zeeman-degenerate atomic systems," *Phys. Rev. A*, vol. 65, p. 033413, Feb 2002. Cited on 66

[53] D. Leibfried, R. Blatt, C. Monroe, and D. Wineland, "Quantum dynamics of single trapped ions," *Reviews of Modern Physics*, vol. 75, no. 1, pp. 281–324, 2003. Cited on 72

[54] G. Guthoehrlein, M. Keller, K. Hayasaka, W. Lange, and H. Walther, "A single ion as a nanoscopic probe of an optical field," *Nature*, vol. 414, p. 49, 2001. Cited on 74

[55] D. J. Griffiths, *Introduction to Quantum Mechanics*. Pearson Education, 2 ed., 2005. Cited on 76

[56] D. F. V. James, "Quantum dynamics of cold trapped ions with application to quantum computation," *Applied Physics B: Lasers and Optics*, vol. 66, pp. 181–190, Feb. 1998. Cited on 81, 82, 83, 84, 85, 88

[57] A. Neuzner, M. Körber, O. Morin, S. Ritter, and G. Rempe, "Interference and dynamics of light from a distance-controlled atom pair in an optical cavity," *Nat Photon*, vol. 10, pp. 303–306, May 2016. Letter. Cited on 90

[58] B.-H. Liu, L. Li, Y.-F. Huang, C.-F. Li, G.-C. Guo, E.-M. Laine, H.-P. Breuer, and J. Piilo, "Experimental control of the transition from markovian to non-markovian dynamics of open quantum systems," *Nature*, vol. 7, no. 12, p. 931934, 2011. Cited on 92

[59] L. Mazzola, S. Maniscalco, J. Piilo, K.-A. Suominen, and B. M. Garraway, "Pseudomodes as an effective description of memory: Non-markovian dynamics of two-state systems in structured reservoirs," *Phys. Rev. A*, vol. 80, p. 012104, Jul 2009. Cited on 92

[60] M. Genkin, D. W. Schönleber, S. Wüster, and A. Eisfeld, "Non-markovian dynamics in ultracold rydberg aggregates," *Journal of Physics B: Atomic, Molecular and Optical Physics*, vol. 49, no. 13, p. 134001, 2016. Cited on 92

[61] H. M. Meyer, "A fibre-cavity based photonic interface for a single ion," *PhD thesis - University of Cambridge*, 2014. Cited on 95